An Opto-Fluidic Architecture for Image-Based Sorting of Biological Cells and Particles

by

Joseph Kovač
Bachelor of Science, Electrical Science and Engineering
Massachusetts Institute of Technology, 2005

Submitted to the Department of Electrical Engineering and Computer Science
in Partial Fulfillment of the Requirements for the Degree of

Master of Engineering in Electrical Engineering and Computer Science

at the

Massachusetts Institute of Technology

September 13, 2006
[February 2007]

Author: _____
Department of Electrical Engineering and Computer Science
September 13, 2006

Certified by: _____
Joel Voldman
Thesis Supervisor

Accepted by: _____
Arthur C. Smith
Chairman, Department Committee on Graduate Theses

An Opto-Fluidic Architecture for Image-Based Sorting of Biological Cells and Particles

by

Joseph Kovač

Submitted to the
Department of Electrical Engineering and Computer Science

September 13, 2006

in Partial Fulfillment of the Requirements for the Degree of
Master of Engineering in Electrical Engineering and Computer Science

ABSTRACT

The present state of technology provides limited practical options for viably sorting and capturing biological cells based on visual information. This thesis presents a novel opto-fluidic architecture which enables potentially viable image-based cell sorting. The architecture combines a trivially-fabricated microfluidic device with a laser and simple support optics to create a platform which enables user-friendly, intuitive, image-based sorting of cells. The microfluidic device contains a microfabricated array of poly-(dimethylsiloxane) (PDMS) wells which are used to passively array cells for visual inspection using any microscopy method (phase, fluorescence, etc.). After inspecting cells, the architecture allows capture of cells of interest by allowing exertion of radiation pressure onto a target cell via the integrated laser, levitating the cell from the well array, and into the flow-field of the microfluidic device for downstream collection and isolation. This thesis presents the design, fabrication, and testing of the platform, and presents a plan for integration of the system into a typical upright microscope.

Thesis Supervisor: Joel Voldman
Title: NBX Associate Professor of Electrical Engineering and Computer Science

Acknowledgements

My ability to complete this project hinged on advice and direction I received from others well before the year I started the M.Eng. program. I extend my most sincere thanks to Prof. Joel Voldman, who first mentored me as a UROP supervisor in 2003, and continues to give direct, meaningful and useful advice as a graduate advisor, despite the fact that his group has grown fivefold since 2003. All of his group members and I genuinely appreciate his availability and willingness go to lengths for us, and I am grateful that he has let me be a part of his group.

The members of the Voldman group have all made it a fun and productive place to work. Adam's optimistic look on nearly everything has been a great balance for my cynical edge, and his willingness to loan me his "MacRosenwells" (or "Bio Flip Chips", depending who you ask) for initial experiments was invaluable. Brian's willingness to help out on any matter will always be valued, as will his by-example setting of high standards. I have Lily to thank for meaningful conversations, and much that I know about growing cells in devices.

Salil's selfless willingness to go to all ends to make sure that our microscopy images look the best that they could will always be appreciated, as will his ability to listen to and put up with my panic of the day. I have Nick to thank for the original concept of popping cells out of wells, and I am fortunate to have such a well read co-worker with whom to discuss ideas.

Katya's zest for getting me up to speed on equipment and protocols was much appreciated, as were her direct questions which forced me to get my story straight. Hsu-yi has always been fun to talk with, and her patience in walking me through the finer points of SU-8 spinning at a particularly stressful time was much appreciated. Pat has been a great comrade in the trenches of classes, and his often sobering biological insights will always be valued. Discussions with Mike have been critical in helping me understand phenomena I saw in my research, and we are all fortunate to have someone in our group so eager to dive into our own research problems with the enthusiasm he would have for his own work.

I learned everything I know about optics from Prof. Dennis Freeman and Dr. Stanley Hong. "Denny" has always been willing to give insight and help regardless of the hour, and it is obvious that he gets his greatest satisfaction from helping students think and seeing that they succeed. "Stan" has been the ideal mentor for learning optics; he has been knowledgeable, approachable, and willing to help in the lab at a moment's notice. In the optics arena I owe thanks as well to Prof. Matthew Lang and Dave Appleyard of the Lang lab. Their insight and help in fundamental experiments gave me the confidence to believe my project was feasible.

Mr. Ian Cheeseman has given me the opportunity to develop confidence in high pressure, high stakes situations, which I have found to be useful time and time again at MIT. No task at MIT has quite carried the weight of the team competitions in Bisley or the Queen's finals.

I am most blessed with my family. My parents, Ivan and Leslie, always prioritized providing opportunities for me over any of their own goals, and their unconditional support in all matters has always been the part of my life for which I have been most thankful. My mother's patience and altruism is unmatched, and my father's complete devotion to seeing that I had all I needed to succeed was instrumental to so much of my development. I could not have asked for better grandparents. I have always valued Ray and JoAnn's ability to help put the tasks in front of me in perspective, and I always look forward to seeing them and receiving their wisdom. My Aunt Leigh Ann's ability to turn perceived mountains into molehills at any time of the day made a great deal of this challenging past year all the more manageable. Her take on both the highs and the lows and unwavering commitment to fairness will always be valuable to me.

~To Mom and Dad~

Table of Contents

TABLE OF FIGURES

LIST OF TABLES

Chapter 1 - Introduction

1.1 Genetic Screening and Motivation

A central goal of cell biology is determination of causal paths of cell behavior. Both behavioral and physical cell properties are partially encoded by the DNA within the cell. Analysis of the contents of a cell should theoretically explain and predict cell behavior. Such analysis discerns the connection between cellular genetics and cell function, and is known as genetic screening.

In practice, genetic screening requires a few steps [1]. First, a genetic pathway is perturbed. Perturbation methods include, among others, introduction of genetic material, interfering molecules (i.e. siRNA), or chemical mutagens, with the end goal of either enhancing (gain of function) or silencing (loss of function) expression of a particular known gene or protein. Second, the cellular response must be detected and recognized. Response could take numerous forms, including change with respect to protein expression, cell morphology, cell individual / social behavior and an infinite number of other possible effects. Tools for this detection range from fluorescence detection of protein / molecule levels to visual inspection of cells. Third, cells exhibiting characteristics of interest must be isolated from the remainder of the population for analysis.

The current state of technology imposes a strong tradeoff between the types of cellular responses capable of being analyzed and the ability to isolate cells of interest. Flow assisted cell sorting (FACS) allows enormously high cell throughput [2], but can only base sorting decisions on whole-cell fluorescence intensity and wavelength at a single timepoint. This characteristic precludes sorting based on temporal behavior or fluorescence location.

Microscopy-based inspection of cells allows assessment of morphology, spatio-temporal cell behavior, fluorescence location, and any other image-based cell characteristic, permitting recognition of numerous cellular responses. Laser capture microdissection (LCM) techniques employing proprietary films can permit isolation of viable cells following microscopy-based inspection (Clonis system, Bio-Rad). In this method, cells are grown on the film, and a laser accurately cuts out film sections containing cells of interest. However, the method is not automated, and requires physical handling of film sections which are cut out and contain target cells, limiting the ability to isolate single cells viably. While LCM isolation of single non-viable cells is possible [3], viable cell isolation is preferable because it permits growth of a population of cells of interest for further assays.

Intuitive, user-friendly, efficient, image-based cell sorting is not offered by the current state of technology. The ideal image-based cell sorting architecture would be compatible with a wide range of cell types, allow easy imaging of cells, allow assays of time durations from short (~minutes) to long term (~days-weeks), allow collection of single target cells expressing responses of interest, and scale to large array sizes while keeping operation and overhead of the architecture simple. This thesis assesses current efforts towards this goal, presents a new architecture for user-friendly, viable, image-based cell sorting, and assesses the extent to which the new architecture fulfills these criteria.

1.2 Prior Work

Previous architectures designed explicitly for image-based cell sorting have employed arrays of individually addressable dielectrophoretic (DEP) traps [4, 5] to arrange cells into array structures. After using microscopy to locate cells of interest, target cells can be released into flow for downstream capture. In the current iteration of this architecture, the number of required electrical interconnects scales as the square root of the number of trap sites. Successful proofs of concept exist with this dielectrophoretic architecture, but scaling these arrays to large (i.e. 100x100) array sizes is still challenging. With the square root scaling, 100x100 and 500x500 arrays would require ~200 and ~1000 individual interconnects, wire bonds, and computer- to-chip connections respectively. Support electronics to drive the device become increasingly complex and expensive as well. Figure 1-1 illustrates the evolution of the DEP cytometer.

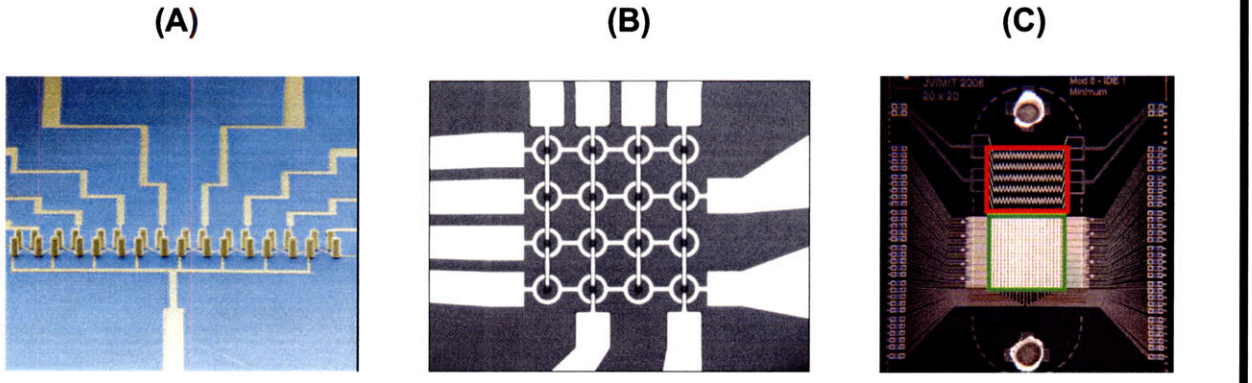

Figure 1-1: Evolution of the DEP cytometer. A) 1x8 array of extruded DEP quadrupole traps [5]. B) 4x4 planar DEP array illustrates interconnection scheme scaling with square root of number of trap sites [4]. C) Taff, Voldman (un-published). 20x20 planar DEP array. Green area is trap site array. Red area indicates additional DEP "vee" structures used to focus cells over trap sites to facilitate loading. Even with efficient square root scaling of interconnects, increasing interconnection complexity is apparent in C).

Other architectures exist which potentially allow image-based sorting of individual cells. A combination of a micropipette and micromanipulator used in conjunction with microwell arrays has been used to isolate single cells exhibiting a target temporal fluorescence behavior [6]. Yamamura *et. al* loaded a cell microwell array such that >80% of array sites contained single cells. Yamamura *et al.* monitored intracellular calcium (Ca^{2+}) levels of single cells before and after cellular stimulation by monitoring activation of Ca^{2+} fluorescent dyes at the single-cell level.

The micropipette / micromanipulator system allowed retrieval of single target cells exhibiting interesting fluorescence temporal behavior for DNA analysis, as shown in Figure 1-2. Such an assay cannot be performed with FACS. One could easily imagine more complex assays being completed with this approach; spatio-temporal fluorescence properties could be monitored as well, allowing full image-based cell sorting. Unfortunately, retrieval of a single cell requires 5-10 minutes, making the method impractical for retrieval of all but the smallest cell populations.

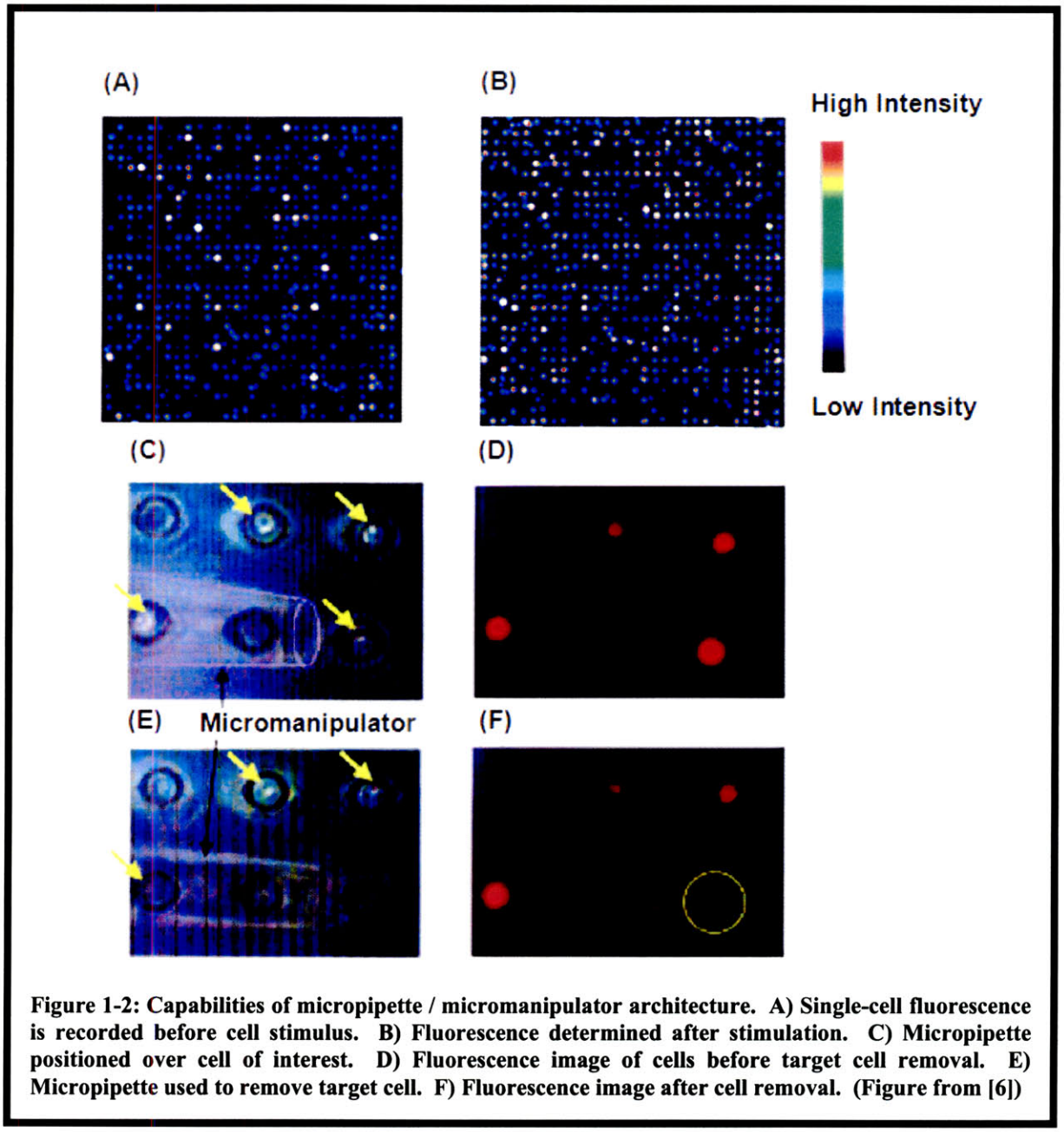

Figure 1-2: Capabilities of micropipette / micromanipulator architecture. A) Single-cell fluorescence is recorded before cell stimulus. B) Fluorescence determined after stimulation. C) Micropipette positioned over cell of interest. D) Fluorescence image of cells before target cell removal. E) Micropipette used to remove target cell. F) Fluorescence image after cell removal. (Figure from [6])

Laser capture microdissection (LCM) is another potential technology potentially offering image-based cell sorting [7]. Revzin *et al.* demonstrated an architecture combining LCM and microwell arrays [3]. First, Revzin *et al.* seeded cells in a poly(ethylene glycol) (PEG) microwell array, washing away cells not settling in wells. Any microscopy technique could be used to locate cells of interest. Next, they fixed the cells, and applied the LCM film over the wells. They then irradiated spots on the film directly over cells of interest with an infrared (IR) laser, fusing the film to target cells. When the film was removed, target cells remained fused to the film and lifted out of the array, allowing for further processing of the cells. Importantly, however, the cells were non-viable. LCM can be used with viable cells, but requires proprietary films, and single-cell selectivity is difficult.

Optoelectronic tweezers (OETs), shown in Figure 1-3, initially appear to offer the solution for image-based cell sorting [8]. OETs use light-mediated DEP to manipulate dielectric particles in suspension. The ITO layers act as transparent electrodes. In an unexcited state, amorphous silicon hydride (a-SiH) acts as an electrical insulator. If light is shined onto a region of a-SiH, the conductivity of the layer rises, allowing spatial patterning of the a-SiH conductivity. In areas where the a-SiH is illuminated, the majority of the AC voltage drops across the fluid; in dark areas, the voltage drops across the a-SiH, giving rise to non-uniform fields, and the potential for DEP.

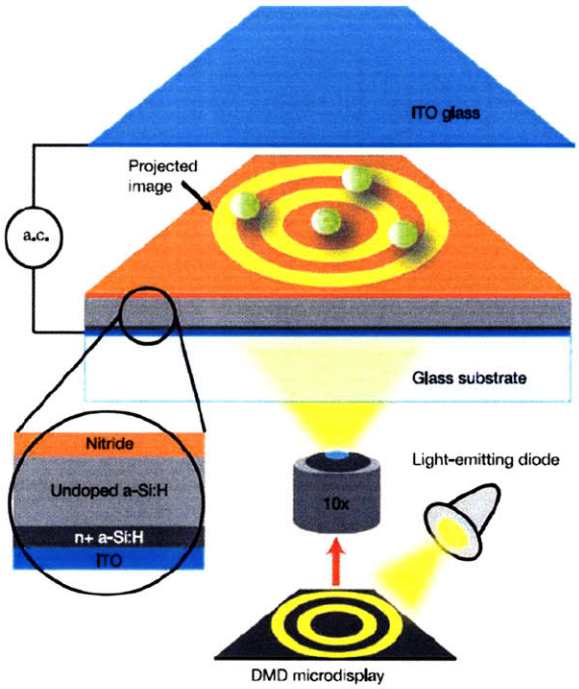

Figure 1-3: Optoelectronic tweezers (OETs). OETs consist of a few simple, unpatterned layers, and allow manipulation of particles and cells in a fluid suspension. Unfortunately, the relatively low photoconductivity of the a-SiH layer prevents operation with high-conductivity media (>~10 mS/m) which is necessary for medium- to long-term cell health. (Figure from [8])

One advantage of OETs is that a digital mirror display (DMD) can be used to project an arbitrary image onto the chip, allowing a reconfigurable electric field distribution within the chamber. Particle and cell sorting with moving "virtual electrodes" has been demonstrated using OETs, as well as simultaneous manipulation of 15,000 particle traps. OETs appear to have all necessary features for intuitive, image-based sorting.

Unfortunately, OET operation is limited to relatively low media conductivities. This limitation exists because the a-SiH layer achieves a maximum photoconductivity of 10 mS/m [9]. In order for modulation of the photoconductivity of the a-SiH layer to significantly affect whether the voltage drops across the fluid or the a-SiH layer, the resistive path through the photoconductive layer must be significantly lower than the path through the fluid when the layer is illuminated. Therefore, a maximum photoconductivity imposes a limitation on the minimum

resistance through the photoconductive layer. This resistive limit restricts the maximum media conductivity with which the device can create non-uniform fields sufficient for DEP.

We modeled the device using FemLab 3.1 (Comsol) to determine the performance of the device in higher (1 S/m) media conductivities, which are more physiologically compatible with mammalian cells than lower media conductivities (1-10 mS/m) reported in preliminary OET experiments [8, 9]. OETs have been reported to be capable of actuating cells in media conductivities as high as 100 mS/m, but no quantitative data were reported. We modeled the fields arising from the illumination of a circular spot on the a-SiH layer. We used a radially-symmetric model as indicated in Figure 1-4 to model the fields in the region around an illuminated spot with a 10V peak-to-peak AC bias applied to the ITO electrodes [8].

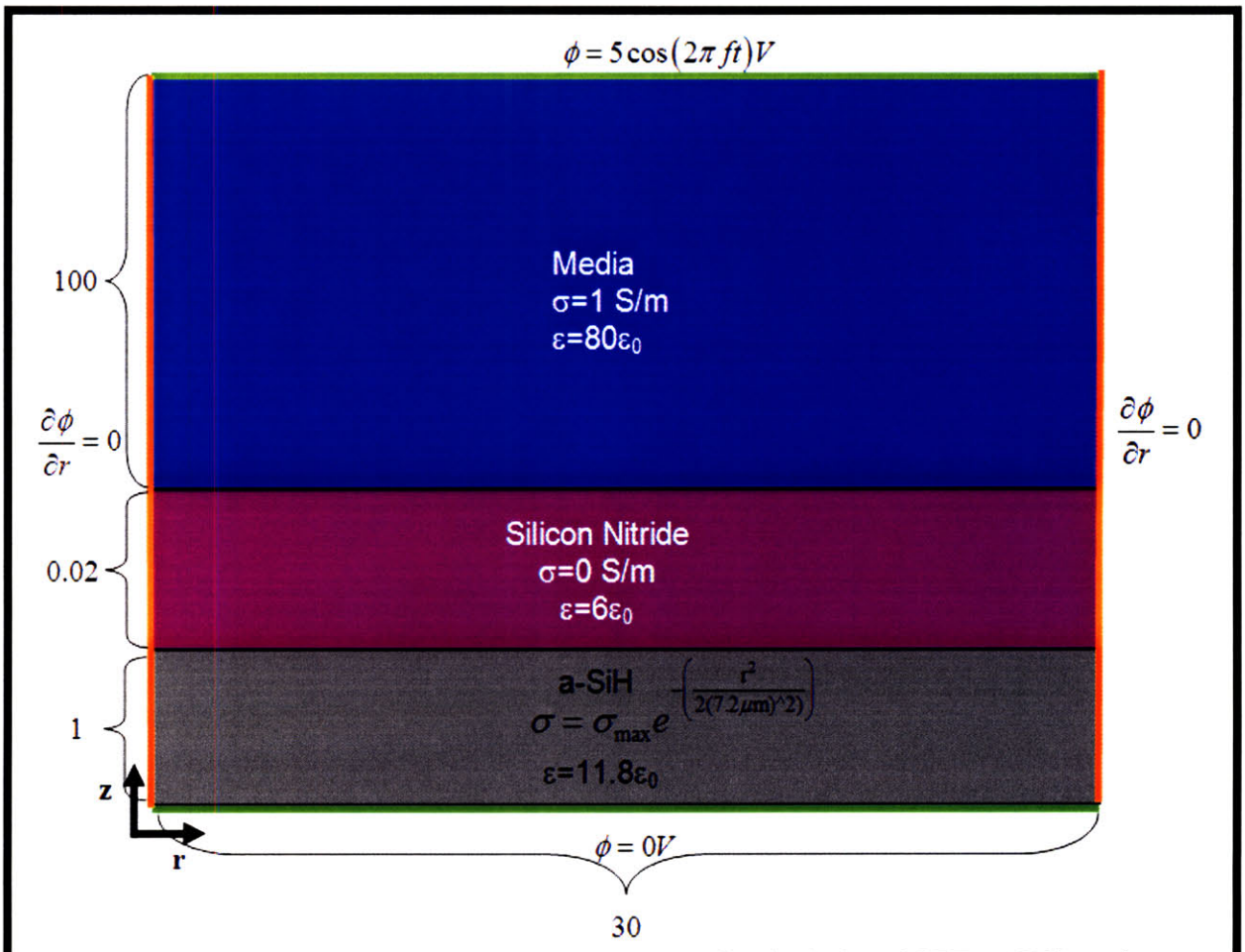

Figure 1-4: Simulation parameters and boundary conditions for simulation of OETs. All dimensions are in microns. ϕ denotes voltage, σ conductivity, ε permittivity, ε_0=8.85e-12 F/m, and f linear frequency in Hz. Zero-flux at r=0 is a symmetry condition; zero-flux at r=30 µm simulates a polar array of activated traps. Spatially varying conductivity profile in a-SiH layer simulates photoconductivity profile due to focusing of a Gaussian beam intensity profile [9].

We observed a strong dependence of resulting potentials / fields on the peak a-SiH photoconductivity, as shown in Figure 1-5. When the peak photoconductivity was allowed to match the media conductivity, nearly all voltage was dropped across the fluid in illuminated areas. Field divergence was greater, and field strength in the fluid was higher than the 10 mS/m case, which represents the modeled performance of the published OETs at 1 S/m media

conductivity [9]. At high media conductivities, the OETs are therefore limited in their ability to maximize field strength and divergence, which together dictate DEP force magnitude.

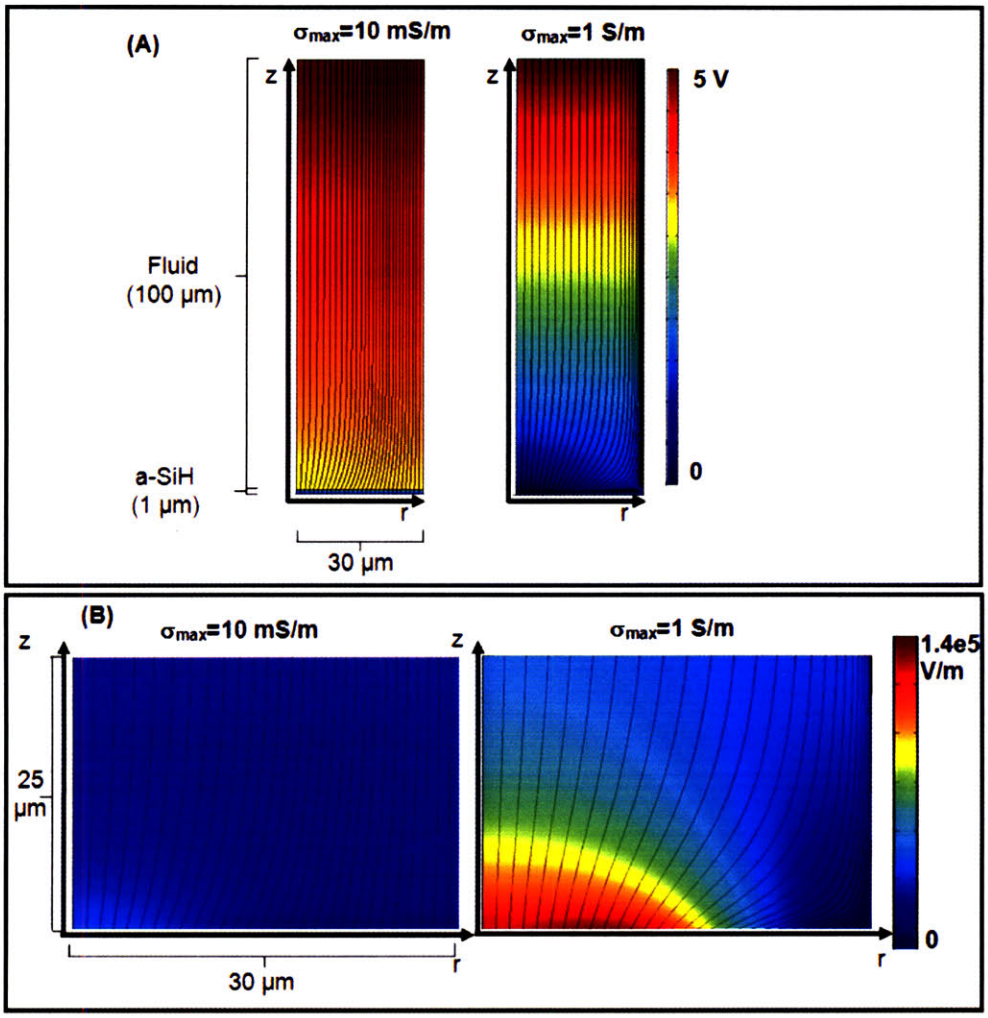

Figure 1-5: Ramifications of peak a-SiH conductivity not matching media conductivity of 1 S/m; streamlines indicate electric field direction. Frequency was 10 MHz. A) In the case of 10 mS/m peak conductivity, a large fraction of the indicated 5V mean-to-peak (MTP) AC voltage is dropped uniformly across the a-SiH layer. In contrast, the case where a-SiH peak conductivity matches the fluid conductivity allows nearly all of the voltage to drop across the fluid in the illuminated region, increasing field strength and divergence. B) Detail of field strength and divergence near the substrate, highlighting the increased field magnitude and divergence for the case where peak a-SiH conductivity could match the fluid conductivity in the illuminated region.

Last, we predicted the magnitude of the DEP force that the OETs could exert on cells of 10 μm radius. We assumed that cells exhibited the following properties: cytoplasmic relative permittivity: 75, cytoplasmic conductivity: 0.75 S/m, membrane capacitance: 1.6 $\mu F/cm^2$, membrane conductance: 22e-3 S/cm^2, membrane thickness: 1 nm, density: 1.071 g/cm^3 [10]. We used StreamForce (http://www.rle.mit.edu/biomicro/publications.htm, Joel Voldman) to calculate the DEP forces acting on cells with these properties given the fields we calculated with FemLab. We plotted the maximum force achievable at various frequencies versus peak a-SiH

conductivity. To determine the largest possible forces with the architecture, we also simulated cases where we replaced the nitride layer with a simulated Debye layer capacitor, with a thickness approximately equal to the Debye length in 1 S/m solution (1 nm) and a relative permittivity of water (80). Figure 1-6 illustrates the results.

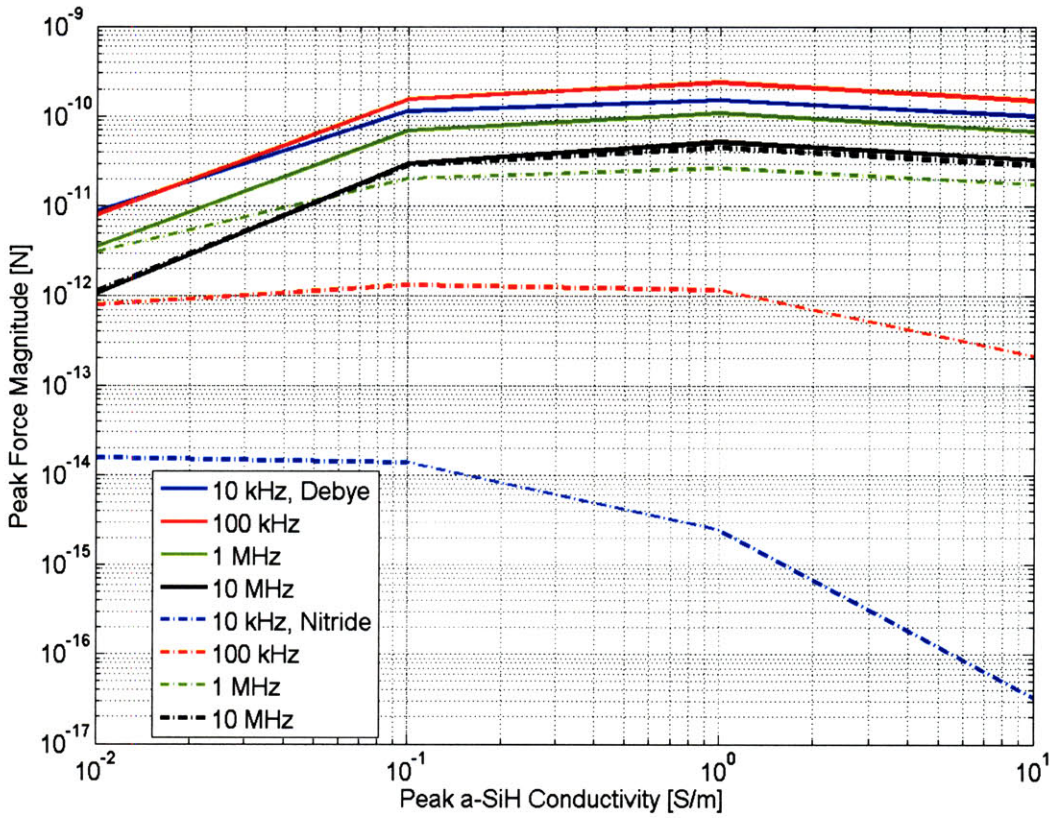

Figure 1-6: Variation of peak DEP force magnitude exerted on a cell with 10-µm-radius with frequency and peak conductivity in the a-SiH layer. All cases at 100 kHz and above benefit from higher peak conductivities in the photoconductive layer than can be achieved using the OETs as reported. We also simulated removing the nitride layer and simply modeling a Debye capacitance in its place to show the maximum possible strength of forces achievable with the architecture.

Except for the 10 kHz case with the nitride layer, peak forces increased in all cases when we raised the peak photoconductivity to levels higher than 10 mS/m. For peak photoconductivities exceeding 1 S/m, peak forces fell, as field divergence began to decrease as the photoconductive layer conductivity began to exceed the fluid conductivity across larger radial distances. The maximum achievable DEP force given the nitride layer and the 10 mS/m peak photoconductivity, (i.e. the OET architecture as published), only slightly exceeded 1 pN.

Such small forces are weak in the context of holding cells robustly against flow. Removal of the nitride layer could enhance forces, but at the possible risk of increasing non-specific adhesion of cells to the device [4]. We predict that OETs, as presented, are impractical as an architecture for image-based cell sorting of live cells in physiological media.

1.3 Optical Tweezers and the Optical Domain

Although OETs do not offer an ideal architecture, the use of light is powerful and enabling. The optical domain offers a few unique advantages. Light can be used to carry information, such as in the context of illumination of a phototransistor gate or photodiode, or, as demonstrated with OETs, for addressing of a cell. Light can also carry energy for transduction into other domains. The thermoelastic effect has been used with black dye-containing poly-(dimethylsiloxane) (PDMS) to create ultrasonic acoustic wave sources [11]. A laser is pulsed onto the black PDMS, where laser energy is absorbed, leading to rapid thermal expansion of the PDMS layer. The expansion launches an acoustic wave into the surrounding medium, representing energy transduction across the optical, thermal, mechanical and acoustic domains.

Optical tweezers represent use of light for addressing and energy transduction [12]. Optical tweezers utilize optical forces to manipulate particles. Optical forces arise from three basic principles: reflection, refraction, and momentum conservation. Optical forces can be divided into two types: scattering forces and gradient forces. Scattering forces arise from the principle of radiation pressure. When radiation strikes a reflective surface, some photons are reflected back, transferring momentum to the reflector. Therefore, a stream of photons striking a reflector exerts a pushing force on the reflector.

Gradient forces can arise when a beam is focused onto a target, as illustrated in Figure 1-7. A ray-optics picture, as shown here, is accurate for cases where the wavelength is much shorter than critical particle dimensions. Momentum conservation dictates that there will be a

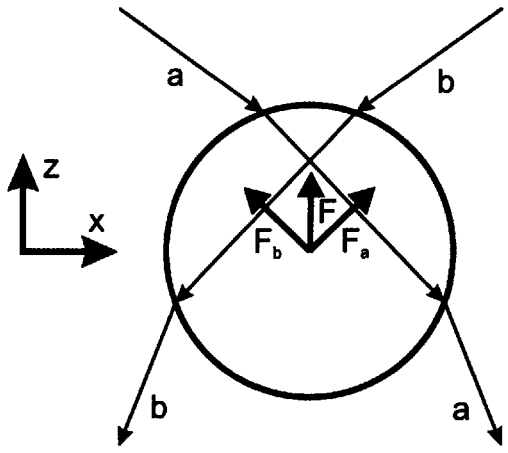

Figure 1-7: Qualitative illustration of optical gradient forces. Photons along rays a and b carry momentum flow proportional to the power of each ray. As refraction changes the ray direction, momentum is transferred to the particle, resulting in forces F_a and F_b, which add to a net force F acting at the particle center. (Figure adapted from [13])

force component perpendicular to each incident ray. In the symmetric case, these forces add to yield a net force as indicated in the figure. Extending to the case of a large number of beams, and recognizing that convergence of rays leads to higher local intensity, the figure illustrates that the gradient force will point up the intensity *gradient* (for particles with a higher refractive index than their surrounding medium), giving rise to the name "gradient force." We will develop optical theory in greater depth in §2.5.

Optical tweezers are a balancing act between the scattering force, which in Figure 1-7 would serve to push the particle in a direction opposite to F, and the gradient force. If the converging rays are focused by a lens, the intuitive result is that gradient forces will seek to move the particle to the focal point of the lens. Scattering forces seek to push the particle out of the focal point. For even weak focusing in the x-y plane, gradient forces are easily observable for particle sizes of up to 10s of microns, making construction of a 2-D optical trap simple. For gradient forces to outweigh scattering forces in z, however, beams of large divergence angles (high-numerical aperture (NA)) must be used. If adequate divergence is used, particles can be stably "tweezed" in three dimensions.

The range of biological optical tweezers applications has been enormous [14]. Initially, addressable optical tweezers arrays appeared to be a possible substitute for DEP electrode arrays for the cytometer. Recent tweezers arrays have used computer-controlled spatial light modulators (SLMs) to construct addressable, dynamic optical trap arrays within the objective field [15]. Vertical cavity surface emitting lasers (VCSELs) have also been used to form addressable optical trap arrays [16].

Unfortunately, the high-NA objective lens required for a stable, three-dimensional trap also implies a small imaging field size ($< \sim 1\text{mm}^2$). Therefore, an optical architecture analogous to the DEP trap array where cells are actively held at all sites could only suffice over a small area of the chip, precluding large arrays. Optical power requirements do not scale well either, as milliwatts of optical power are typically needed to exert piconewtons of lateral holding force; a modest number of 1000 trap sites would requires watts of optical power. Optical tweezers arrays are clearly not an apt replacement for large DEP trap arrays.

Although stable, three-dimensional optical trapping over large areas is not feasible, optical forces can be used to sort cells in alternative ways. Optical force switching of microfluidic channels has been used to sort cells at critical junctions, as illustrated in Figure 1-8 [17]. In the illustration, flow biasing ensures that all cells travel down a single path at the junction. Target cells are deflected by radiation pressure into a separate collection path. A similar approach has also been used in multi-layer PDMS microfluidic devices at vertical channel junctions to switch the cell travel path from one layer to the other [18].

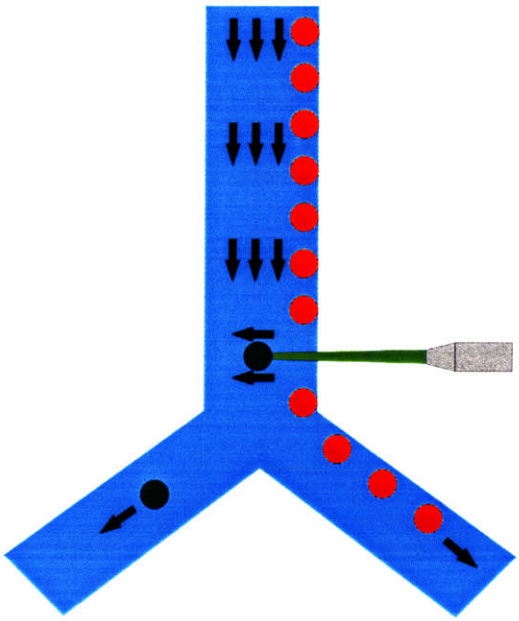

Figure 1-8: Schematic sort using optical force switching at a critical junction in a microfluidic device. (Figure adapted from [17])

Wang *et. al.* published enough information to estimate the applied scattering forces [17]. The exerted optical force can by estimated by recalling the equation for Stokes drag (neglecting wall effects),

$$F = 6\pi\mu r v\,, \tag{1.1}$$

where r is cell radius, v is the cell velocity, and the viscosity, μ, is taken to be that of water, 1cP.

If the required deflection for separation is conservatively assumed to be 10 μm, occurs over the period of 4 ms as reported, and we estimate a cell radius of 8 μm, a lower-bound velocity estimate is 2.5 mm/s, implying 377 pN of Stokes drag. The incident sample power was 13.2 W at 1,070 nm, implying a power / force ratio of 35 mW / pN. The laser was applied at an angle in the experiment; perpendicular application would apply a larger force. Therefore, use of ~100 mW of IR power is sufficient to produce piconewtons of easily addressable pushing force to a cell.

1.4 A Novel Opto-Fluidic Image-Based Cell Sorter

As demonstrated, optical forces alone are insufficient to create a user-friendly, image-based cytometer capable of arraying and sorting large numbers of cells. Strong gradient forces require small imaging field sizes, and scattering forces alone cannot array and hold cells in a grid structure. We propose a new architecture for image-based cell sorting which uses passive microwell structures to array and hold cells, and employs optical forces and microfluidics to remove cells from the array.

Analogously to the DEP trap architecture, we will use cell microwell arrays to create large arrays of single cells and hold them in a grid in the presence of fluid flow. Cell microwell arrays allow cell array construction nearly tantamount to that of the DEP architecture; Rettig *et al.* showed that proper design of well sizes could lead to single-cell loading efficiencies of ~80% [19]. Microwell arrays can be trivially fabricated using a traditional SU-8 and PDMS-molding process.

We will incorporate microwell arrays into the floors of microfluidic flow chambers. We will load arrays by injecting a cell suspension into the chamber, allowing cells to sediment into wells, and flushing cells exterior to wells, as illustrated in Figure 1-9-A&B. At this point, we will have created a near-single-cell array without using any power or interconnects; array loading is completely passive. We will then observe the array using any microscopy technique, noting positions of cells of interest.

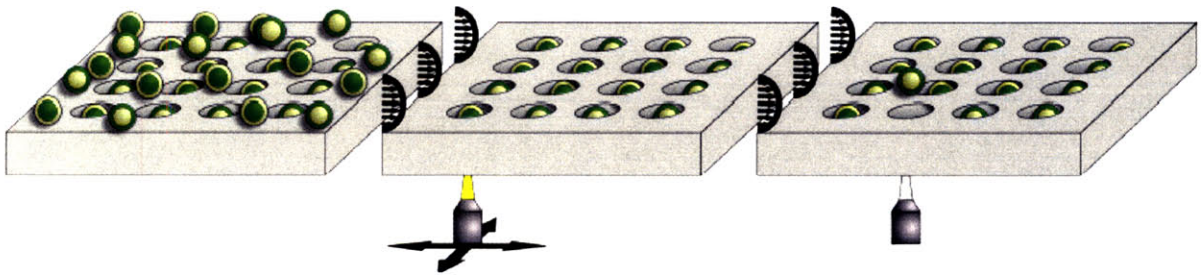

Figure 1-9: Schematic of opto-fluidic architecture operation, depicting a section of the flow chamber floor. A) Cells are injected into the device and allowed to settle into wells. B) Cells not residing in wells are flushed by reinstating flow. Cells are investigated by any microscopy technique, noting locations of cells of interest. C) Target cells are levitated from wells and washed downstream for collection.

A combination of optical forces and microfluidics will enable retrieval of cells of interest. As demonstrated in optical force switching applications [17, 18], the optical scattering force allows for simple cell repositioning, in our case, out of a microwell. We will incorporate a laser into the imaging platform which can be focused onto a target cell. The laser will be of sufficiently low divergence that the scattering forces dominate, allowing us to levitate a target cell out of its well, as shown in Figure 1-9-C. We will then re-instate flow, pushing the target cell downstream for collection. We illustrate a high-level view of the architecture in Figure 1-10.

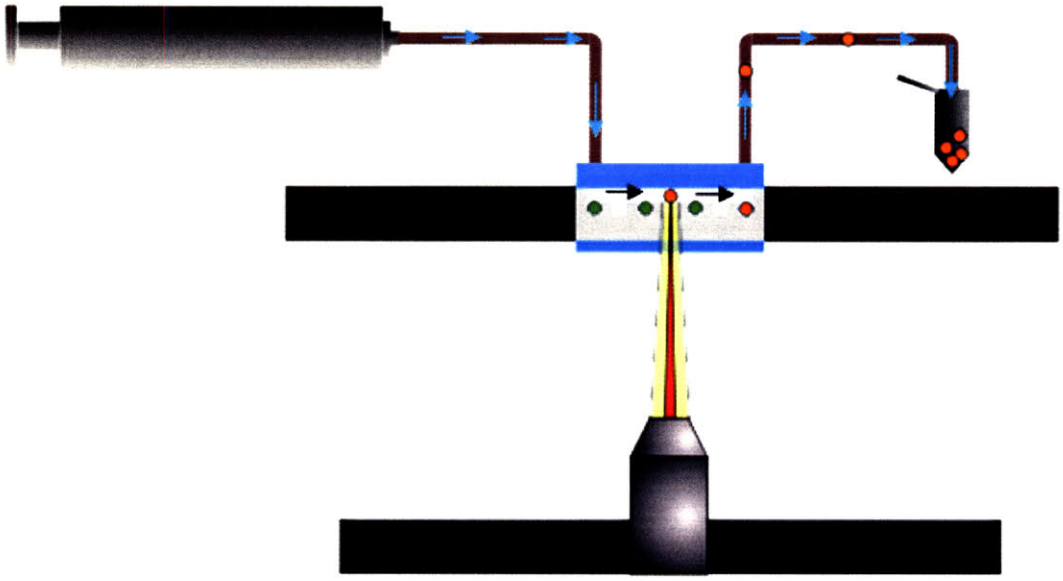

Figure 1-10: High-level view of architecture. Microfluidic device allows simple loading of microwell array via sedimentation and subsequent flushing. A laser (shown in red) is incorporated onto the imaging axis, allowing a cell of interest to be levitated from the well and into the flow field (shown via an arrow) for downstream collection.

The architecture is similar to the platform discussed in §1.2 which combined microwell arrays with micromanipulator / micropipette systems [6]. The drawback to the micromanipulator / micropipette system is that single cells take minutes to reclaim and require the cumbersome overhead of a micromanipulator system. Our architecture will effectively replace the micropipette and micromanipulator system with a laser and microfluidic device for cell capture. The laser and microfluidic device will be compact and easily integrated into traditional fluorescence microscopes and enables cells to be selected and retrieved within seconds instead of minutes.

Combining the arraying of microwell arrays with optical force switching enables simple, efficient arraying of cells into a grid with dynamic addressing and control of array sites. Device fabrication consists of a trivial SU-8 process. The only overhead requirement is that a laser be incorporated on the optical axis for focusing into the specimen plane. Operation of the architecture is fast, user-friendly, and intuitive: removal of a cell simply requires directing the laser at the cell. This thesis will demonstrate the necessary design considerations, implementation, and successful testing of the architecture.

Chapter 2 - Architecture Design and Implementation

2.1 Summary of Design Challenges

Design of the opto-fluidic cell sorting architecture required handling numerous constraints. First, care was taken to determine the optical parameters which would not harm cell health. However, those optical parameters needed to yield forces large enough to manipulate the cells effectively. The optical forces required also hinged on the surface treatment – increased non-specific cell-substrate interactions would require more optical manipulation force. Surface treatments intended to reduce these interactions would need to be viable for the cells. While each of these issues is partially independent, constructing the best possible architecture required considering all of them both independently and simultaneously.

2.2 Cell Health Effects of Optical Methods

Numerous publications have studied cellular response to high optical intensities in optical tweezers contexts [17, 20, 21] . These studies suggest that attention to optical operating parameters allows optical tweezers to be used with cells with virtually no adverse effects. Wavelength, peak optical intensity, exposure time, total energy delivered, and total energy density have been used to quantify cellular agitation [17, 20, 21]. Liang *et al.* recorded these metrics for optical trapping experiments with Chinese hamster ovary (CHO) cells. Liang varied wavelength from 700 nm to 1064 nm, exposure time from 1 min. to 20 min., and power from 88mW to 176 mW, using the total fraction of cells capable of clonal growth after irradiation as a damage metric.

Figure 2-1 illustrates relevant results. Wavelengths of 950 nm and 990 nm appear most favorable for cell health. The 1064 nm wavelength, widely used in many tweezers setups due to low cost, yielded poor clonability. Exposures of up to 3 min. resulted in 100% clonability. Table 2-1 summarizes the quantitative metrics for each case.

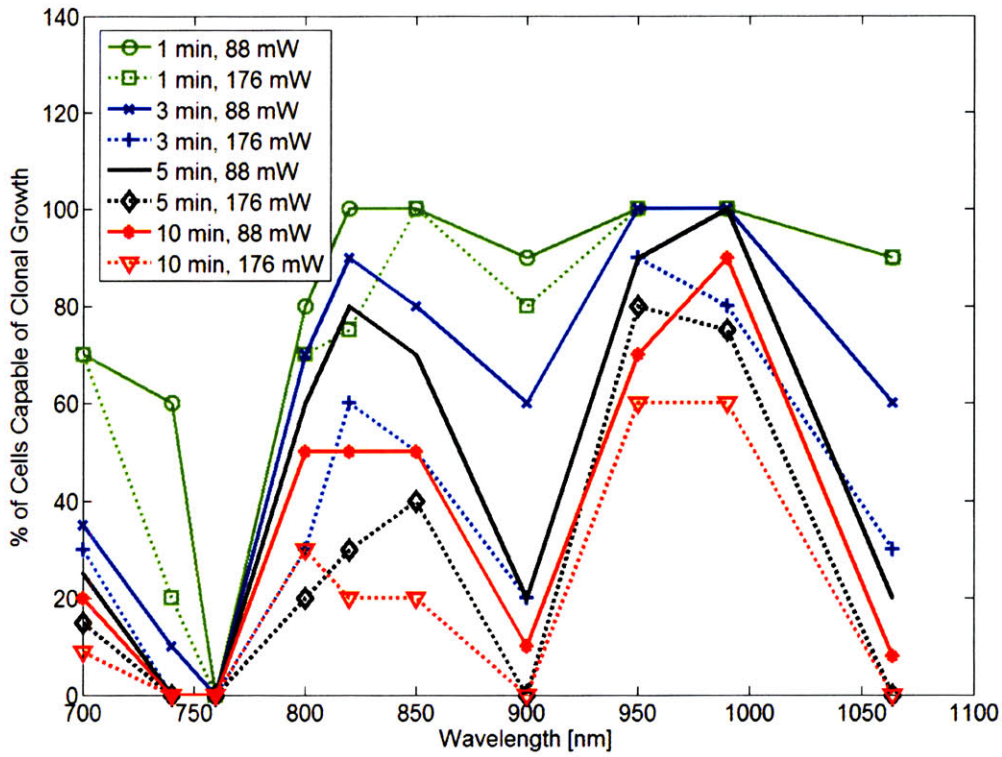

Figure 2-1: Wavelength, time, and power dependence of CHO photosensitivity. Results indicate that no damage occurs at 950 nm and 990 nm for 1 min. exposures at either power level, as well as with other similar parameters. (Figure adapted from [20])

Table 2-1: Cloning efficiency in CHO cells as a function of energy density (power density x time) and wavelength. Areas of 100% efficiency are highlighted in gray. (Table adapted from [20])

mW	88	176	88	88	176	88	176	88	176	176
Min	1	1	3	5	3	10	5	20	10	20
***ED**	18	36	54	90	108	180	180	360	360	720
λ(nm)										
700	70	70	35	25	30	20	15	5	9	0
740	60	20	10	0	0	0	0	0	0	0
760	0	0	0	0	0	0	0	0	0	0
800	80	70	70	60	30	50	20	15	30	0
820	100	75	90	80	60	50	30	20	20	10
850	100	100	80	70	50	50	40	40	20	0
900	90	80	60	20	20	10	0	0	0	0
950	100	100	100	90	90	70	80	60	60	40
990	100	100	100	100	80	90	75	70	60	20
1064	90	90	60	20	30	8	0	0	0	0

Neuman *et. al* measured the wavelength-dependent sensitivity of *E. coli* [21]. Neuman attached the flagella of genetically-modified *E. coli* to glass. The modified *E. coli* flagella exhibited non-specific binding to glass; after binding, the *E. coli* rotated due to rotation of their flagella. Neuman trapped the *E. coli* with 100 mW optical power at various wavelengths, and recorded the time for rotation to drop to 50% of its original rate. Figure 2-2 shows these results plotted over the findings of Liang *et. al* at 88 mW.

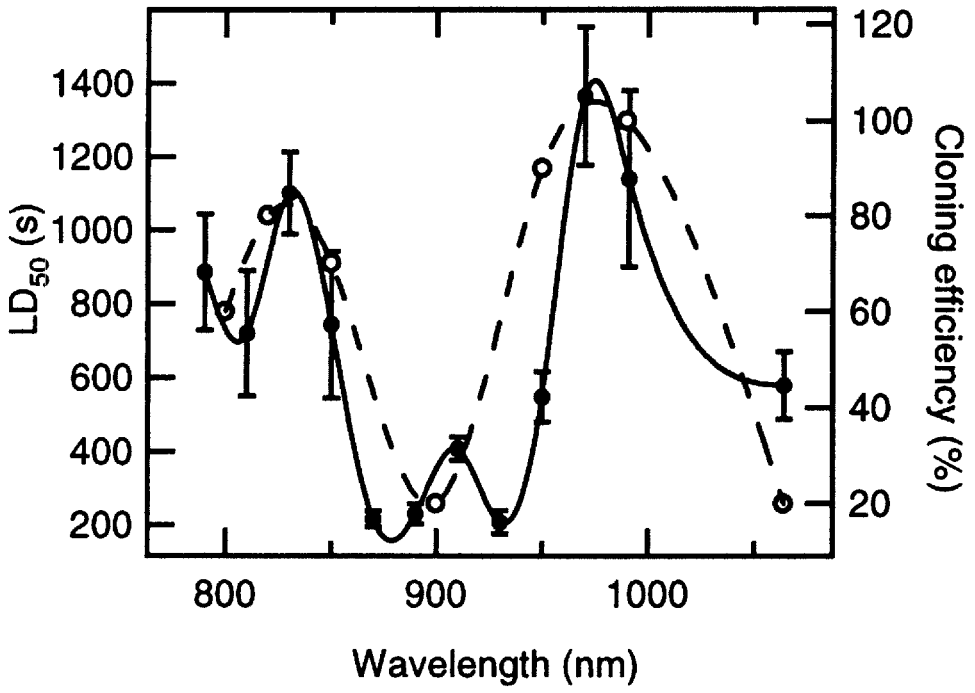

Figure 2-2: Photodamage spectrum for *E. coli* (solid circles / line, LD_{50} dependent variable) and CHO cells (open circles / dashed line, cloning efficiency dependent variable). CHO cells were exposed for 5 min at a power level of 88 mW, while *E. coli* were exposed at 100 mW. LD_{50} indicates the illumination time needed for *E. coli* rotation rate to drop to 50% of its initial rate. (Figure from [21])

The damage spectrum qualitatively matches that of CHO cells. Under anaerobic conditions, damage dropped to control levels, suggesting that oxygen was in the damage pathway, consistent with theory suggesting that singlet oxygen is responsible for cell damage [21]. Another study showed that cell temperature rose by ~1.15 K per 100mW applied to trapped CHO cells, suggesting heating effects would be negligible for brief manipulations [22].

Wang *et al.* published a compilation of concluded damage thresholds from the above two experiments, as well as from two other experiments [17]. Wang *et al.* reported their own experimental parameters, which were shown to be not damaging to cells, but not necessarily at a critical damage threshold level. Table 2-2 summarizes these findings.

To levitate a cell resting on a surface, the levitation force must overcome the net buoyancy-compensated gravitational force on the cell, weak nonspecific surface interactions, and Stokes drag. The net gravitational force acting on a cell in physiological saline is ~ 1pN. With proper surface engineering, non-specific interactions should be minimal. In §1.3, the *conservative* power / scattering force ratio was estimated to be 35 mW / pN, implying a need for

~175 mW of power to exert ~5pN of force. By Stokes drag, such a force would levitate a 16-μm-diameter cell at ~ 25 μm/s. For a 30 μm-deep well, levitation from the well would take ~ 1 s. Table 2-2 illustrates these predicted operating parameters as a comparison to known damage thresholds.

Table 2-2: Compiled table of damage thresholds from different experiments. Experiment with HeLa cells did not show signs of damage; it is listed here as an acceptable operating point rather than as a threshold. Gray-shaded row indicates optical parameters for proposed architecture, as described later. (Adapted from [17])

Cell Type	λ (nm)	Power (W)	Exposure Time (s)	NA	Spot Width (μm)	Power Density (W/cm^2)	Energy Density (J/cm^2)	Energy (J)
Human Sperm	1064	0.3	120	1.3	1.50	6.8E+07	8.1E+09	36
CHO	1064	0.088	60	1.3	1.50	2.0E+07	1.2E+09	5.3
E. coli	1064	0.1	600	1.2	1.62	1.9E+07	1.2E+10	60
NC37 lympho-blast	1064	0.12	30	1.3	1.5	2.7E+07	8.1E+08	3.6
HeLa	1070	13.2	0.004	0.2	4.9	7.0E+07	2.8E+05	0.053
HL-60	980	0.175	1	≤0.1	10.0	2.2 E+05	2.2E+05	0.175

Although the proposed power level exceeds three of the five experiments, the power and energy densities required are orders of magnitude below those found damaging. Power densities are lower because the laser will be focused to match the size of the cell to optimize scattering, unlike tweezers applications where the beam is focused close to the diffraction limit to create large gradient forces. Energy densities are lower for the same reason, and because exposure times are 1-2 orders of magnitude shorter. Total energy is 1-2 orders of magnitude lower than in 4 of the 5 experiments as well.

The 100% clonability of CHO cells under 176 mW illumination demonstrated by Liang suggests that higher powers are harmless if only applied briefly. This result is further supported by Wang *et al.*, who demonstrated cell viability with 13.2 W of applied power. It appears that power and energy density, total energy, and exposure time are the critical factors, and the operating conditions for the architecture fall easily within these reported healthy limits.

2.3 Surface Engineering

Numerous cell types are biologically compatible with fibronectin-adsorbed PDMS surfaces which are mixed with the standard 10:1 base to curing agent ratio [23]. Before attempting surface treatments inside flow chambers, we determined a cleaning and surface treatment protocol for PDMS cell culture. In the case of adherent cells, cells must adhere and grow on the PDMS. Adherent cell lines often trigger apoptosis when they bind inadequately to their surface. In the case of non-adherent cells, the surface should minimize non-specific interactions with the cells. The case of adherent cell lines is especially demanding. The surface must permit cells to attach and grow for timescales longer than at least a day, but cell-surface binding must be reversible for release to occur.

Starting with a clean, uniform surface is critical when engineering a surface. We experimented with different cleaning treatments by preparing 12-well plates with a 2-3 mm layer

of PDMS poured into each well at the recommended 10:1 base : curing agent ratio and cured the PDMS in the wells. We performed each surface treatment in triplicate. Table 2-3 summarizes the test protocol.

We cultured NIH 3T3 fibroblasts in serum-containing media (87%/vol. DMEM (11960-044, Gibco); 10%/vol. BCS, HyClone; 1%/vol. Penicillin-Streptomycin, (15140-122, Gibco); 2%/vol. l-glutamine (25030-081, Gibco)). Incubation conditions were 37.0° C, 7.5% CO_2 atmosphere. We fed cells every other day and passaged at 80% confluence. This 3T3 culture was used for all experiments in this thesis involving 3T3s.

Table 2-3: Method for surface-cleaning protocol comparison

Step	Description	Time/Temp. (C)
1. PDMS Mix	10:1 base : curing agent ratio; 2-3 mm poured/well	NA/RT
2. PDMS Cure	Cured PDMS in wells	2.5 h / 65 C
3. PBS Soak	Added 3 mL PBS to each well to guard against cleaning agent uptake into PDMS	4.25 h / RT
4. Aspirate	Aspirated PBS	
5.Cleaning Agent	3 wells each filled with 2 mL 80% ethanol, 100% isopropyl alcohol, alconox (10 g/L), or left empty	0.5 h / RT
6. Aspirate	Aspirated cleaning agent	
7. UV Sterilize	Placed well plate under UV	1 h / RT
8. Media protein adsorb	Filled all wells with 3 mL 10% BCS DMEM-based media for adsorption to surface	15 h / 37 C
9. Aspirate	Aspirate media	
10. Cell seed	Seeded cells at a density of ~ 100,000 cells/mL; total of 2 mL of 10% BCS DMEM-based media deposited in each well	
11. Incubation	Incubated cells	19 h / 37 C

After incubation, we examined the cells under phase microscopy. Figure 2-3 illustrates cell morphology under each cleaning condition. Cell morphology depended weakly on cleaning method. Cell density was approximately equal as well; Figure 2-3 is unrepresentative of density within each well.

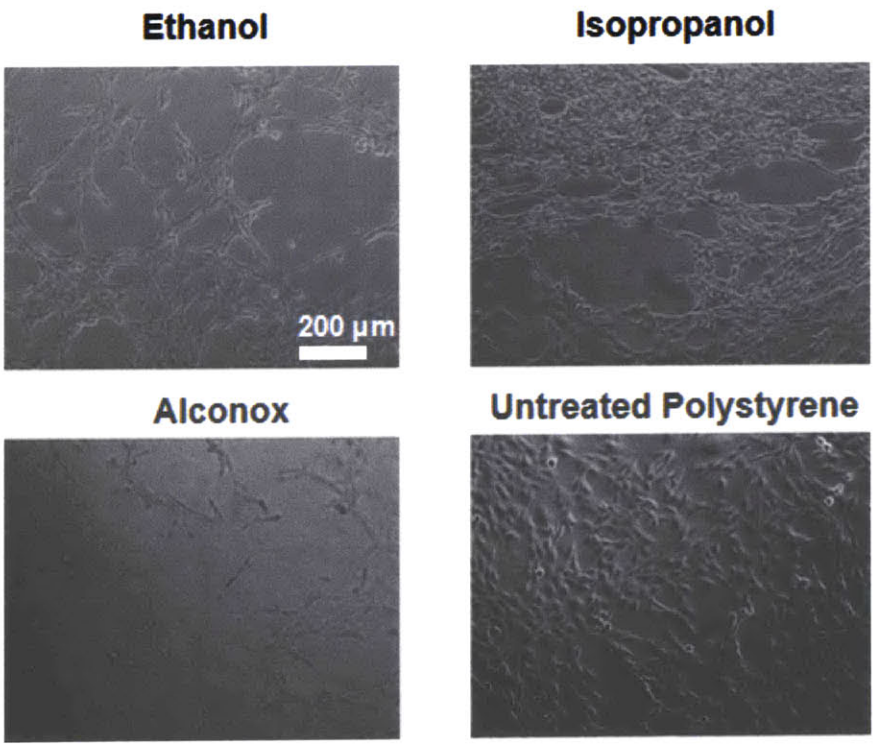

Figure 2-3: Morphology of 3T3 cells growing on PDMS under various cleaning treatments. General morphology is roughly the same in all cases, as is overall density in each dish (global dish density is not accurately represented in each picture).

After concluding that the cleaning method was unimportant, we decided to use ethanol for pre-cleaning. However, we found that a simple PBS rinse of the wells detached many of the cells. Such detachment does not occur on polystyrene, and is indicative of weak surface attachment, and the possibility of inducing undesirable signaling pathways.

We developed a surface treatment protocol for fibronectin adsorption to increase adhesion. We used a published concentration of 5 µg/mL in PBS to form our fibronectin (33010-018, Invitrogen) solution [23]. We sought to determine whether fibronectin made a noticeable increase in the ability to perform a PBS wash without detaching adhered cells. We compared a fibronectin-treated PDMS surface with a media-treated PDMS surface. Using 12-well plates, we performed the protocols summarized in Table 2-4 and Table 2-5 to compare surface treatments and the required times to perform those treatments. We tried each condition in triplicate.

Table 2-4: "Long" protocol for surface perparation

Step	Description – "Long Protocol"	Time/Temp. (C)
1. PDMS Mix	10:1 base : curing agent ratio; 2-3 mm poured/well	NA/RT
2. PDMS Cure	Cured PDMS in wells	2.5 h / 65 C
3. PBS Soak	Added 3 mL PBS to each well to guard against cleaning agent uptake into PDMS	4.5 h / RT
4. Aspirate	Aspirated PBS	
5. Cleaning Agent	3 wells each filled with 2 mL 80% ethanol	0.75 h / RT
6. Aspirate	Aspirated cleaning agent	
7. UV Sterilize	Placed well plate under UV	1 h / RT
8. Media protein adsorb	Filled all wells with 2 mL of either 5 μg/mL fibronectin suspended in PBS or 20% BCS DMEM-based media for adsorption to surface	18 h / 37 C
9. Aspirate	Aspirate media	
10. Cell seed	Seeded cells at a density of ~10,000 cells/mL; 2 mL suspension deposited in each well	
11. Incubation	Incubated cells	variable / 37 C

Table 2-5: "Short" protocol for surface preparation

Step	Description – "Short Protocol"	Time/Temp. (C)
1. PDMS Mix	10:1 base : curing agent ratio; 2-3 mm poured/well	NA/RT
2. PDMS Cure	Cured PDMS in wells	2.5 h / 65 C
3. UV Sterilize	Placed well plate under UV	1 h / RT
4. PBS Rinse	Rinsed wells with PBS	1 min / RT
5. Cleaning Agent Rinse	Rinsed wells with 80% ethanol	1 min / RT
6. Media protein adsorb	Filled all wells with 2 mL of either 5 μg/mL fibronectin suspended in PBS or 20% BCS DMEM-based media for adsorption to surface	1 h / 37 C
7. Aspirate	Aspirate media	
8. Cell seed	Seeded cells at a density of ~10,000 cells/mL; 2 mL suspension deposited in each well	
9. Incubation	Incubated cells	variable / 37 C

We viewed cells 24 hrs. and 48. hrs after seeding. At 24 hrs., we rinsed 3 wells prepared with each treatment (long vs. short and fibronectin vs. media) with PBS to look for signs of weak adhesion. We left other wells alone with the different conditions (again in triplicate) so that we could examine adhesion at 48 hrs. After the PBS wash at 24 hrs., we terminated washed cells; we performed PBS washes at 48 hrs. with untouched cultures. Figure 2-4 illustrates the results.

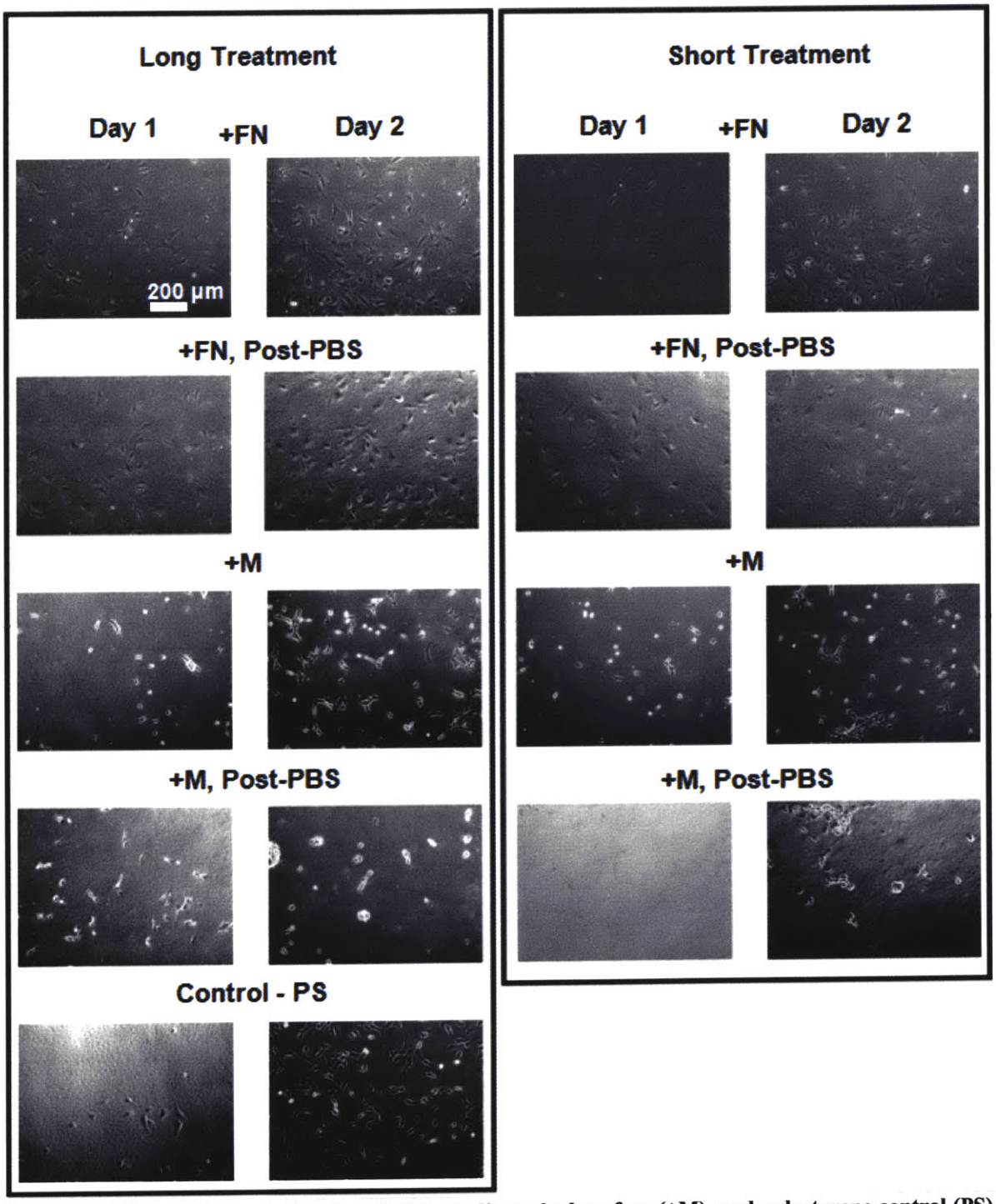

Figure 2-4: Fibronectin-treated surface (+FN), media-soaked surface (+M), and polystyrene control (PS), and comparison between "long" and "short" treatments. Fibronectin coating promotes healthier morphology and greater adhesion after PBS wash.

The results indicated a large morphological difference between cells seeded on fibronectin-coated PDMS and PDMS simply soaked in media. After a PBS wash, cells seeded on the fibronectin surface remained intact with little change in morphology. In contrast, cells seeded on PDMS without fibronectin exhibited detachment similar to that seen after trypsinization.

The results from the short and long treatments were nearly identical. A simple rinse-clean of the PDMS and hour-long fibronectin adsorption yielded morphological data nearly equivalent to the longer process. The surface treatment of Table 2-5 is easily implemented in under 2 hours in a PDMS flow chamber.

Protein adsorption is a complex process; interconnected sub-processes during adsorption include adsorbed protein movement, dissociation, denaturation, (sometimes resulting in irreversible adsorption), and change in conformation, among others [24]. Despite this complexity, studies with engineered self-assembled monolayers (SAMs) have illustrated results useful for engineering protein-adsorbed surfaces [24]. These studies showed that proteins adsorbed more extensively to hydrophobic ($-CH_3$) than hydrophilic (-OH) surfaces.

Large (MW> 200 kD) proteins adsorbed on both surface types, but more extensively on hydrophobic surfaces, suggesting that fibronectin (MW 440kD) would adsorb more to hydrophobic surfaces than hydrophilic surfaces. However, in the context of engineering a surface for cell adhesion, sheer adsorption quantity is not the only critical factor. Protein surface density, conformation, and conformation of polypeptide sequences exposed at the surface are each important parameters for cell recognition [23].

A study by Lee *et al.* investigated cell proliferation of numerous cell types (including 3T3s) on PDMS preparations of varying compositions (i.e. different base / curing agent ratios, as well as PDMS post-processing steps) which had been exposed for fibronectin adsorption prior to cell seeding. Results concerning PDMS surfaces which had been exposed to a plasma treatment prior to adsorption were particularly interesting. Lee showed that fewer 3T3s initially attached to plasma-treated PDMS surfaces than to other surface preparations. Furthermore, the 3T3s proliferated less on the plasma-treated surfaces relative to others. 3T3s also exhibited detachment on plasma-treated PDMS, and on surfaces exhibiting detachment, attached cells had a rounded shape. Lee *at al.* concluded that "low amounts of fibronectin on hydrophilic surfaces may lead to low ligand-mediated cell spreading, absence of maturation, and eventually cell death through a series of signals from the nonenganged adhesion receptors to the mechanism responsible for apoptosis."

Plasma treatment renders a thin layer of the PDMS layer hydrophilic. Lee *et al.* reported advancing water contact angles of $100°\pm4°$ for PDMS composed of the recommended 10:1 base-curing agent mixture ratio, and contact angles of $< 15°$ for plasma-treated PDMS, giving credence to the hypothesis that low amounts of fibronectin adsorbed to the plasma-treated PDMS. The widespread practice of irreversibly bonding PDMS to glass to form a flow chamber requires a plasma bond. Unfortunately, protein adsorption would be hindered after the bond given the findings of Lee.

If hydrophobicity were truly a strong determinant of fibronectin adsorption, reversing the surface to hydrophobic should improve protein adsorption after bonding. After plasma treatment, PDMS cured in the recommended conditions (100 min. @ 85° C) and exposed to air will reverse its surface properties from hydrophobic to hydrophilic within 15 minutes [25]. However, we found that after plasma bonding, the inside of a flow chamber still exhibited hydrophilic properties, even after the bonded device was allowed to remain at room temperature

for 72 hours. We will describe this observation in greater detail in §3.1. In order to accelerate regain of hydrophobicity, we placed bonded chambers in the PDMS curing oven for 12 hours before protein adsorption. As we will show in §3.1, this time course was sufficient to eliminate observable hydrophilic properties of the chamber, presumably enhancing protein adsorption.

Reversibility of the cell-surface binding is critical for the adherent cell surface treatment. After cells had adhered inside wells, we planned to release cells by flowing trypsin over the loaded well array to weaken cell adhesion to the PDMS. We intended to detach cells by gently flowing media over the trypsinized cells until the cells separated completely from the PDMS and began to move in the wells. We expected cells to oscillate and tumble in rather than be ejected from their wells due to the hydrodynamic shielding afforded by the wells.

The described flow problem is difficult to model. When the cell size is on the order of the well size, the cell significantly perturbs flow streamlines. Cells are deformable and move within the well, further complicating flow modeling. We did not attempt to quantitatively model our proposed cell release protocol. This flow problem has become a collaborative effort with the Singapore-MIT Alliance (SMA).

For the non-adherent cell release architecture, we used the same adsorption protocol, but used 7.5 % bovine serum albumin (BSA, stock solution 15260-037, Invitrogen) in place of fibronectin. As we will demonstrate later, use of BSA was both necessary and sufficient to reduce surface interactions enough to allow for easy cell release.

2.4 Preliminary Optical Experiments

2.4.1 Optical Test Layout

We constructed a simple optical system for initial concept testing and parameter optimization (Figure 2-5). L2 was track-mounted to allow fine tuning of beam divergence and the laser focus. We laid out the system such that the CCD (Fire-I 400, Unibrain) image focus matched the focal plane of the laser (Innova 300C, Coherent). We accomplished this by removing L3, F (generic filter glass blocking laser line), and CCD. We placed a sample on the stage and illuminated it using LAMP (generic gooseneck lamp). We reflected the imaging path normally passing to the CCD to a wall in the room ~ 15 feet away. We adjusted the stage until the sample image came into focus on the wall, approximately focusing the image to infinity, which corresponded to the sample being exactly in the focal plane. After replacing lens L3, we positioned the CCD so that the CCD image of the sample was in focus. Since the laser beam would focus at the focal plane of the objective OBJ (10x, 0.25NA, JIS, Edmund Optics), this procedure ensured that the laser focal plane would coincide with the sample image focal plane at the CCD. Therefore, focusing the laser onto a target only required positioning the sample such that CCD image of the target was in focus.

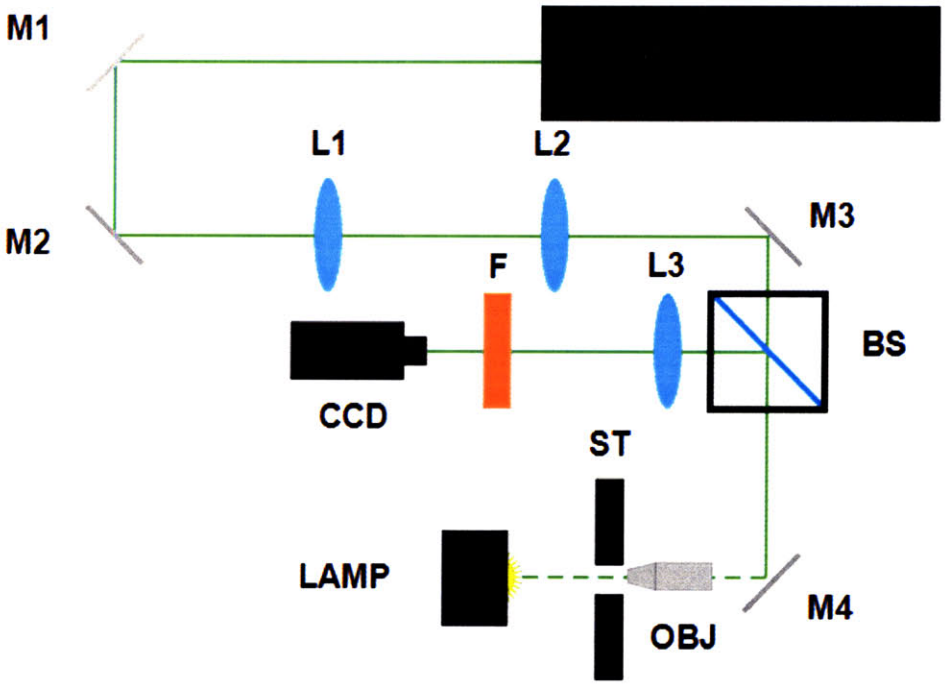

Figure 2-5: Optical layout. Mirrors M1, M2 position beam. Lenses L1 (f=88.3), L2 (f=75.6) fill objective OBJ optimally. Beamsplitter BS (95%/5% transmitted / reflected) passes majority of laser power to OBJ. Mirror M4 directs beam upward (dashed). Stage ST is 3-axis. LAMP illuminates sample. Tube lens L3 focuses beamsplitter reflection for imaging via CCD. Long-pass filter F protects CCD from sample reflections.

In an alternate implementation, we used M4 to direct the beam downwards for different experiments described later. A more efficient way to implement the setup would use a dichroic in place of BS, passing nearly all laser power to the sample and no laser power to the CCD, removing the need for F. Additionally, more light from the sample might reach CCD (BS only had 5% reflectance), lowering the required brightness for LAMP. The laser source was a 514 nm argon ion laser; we used a visible wavelength for ease of alignment.

2.4.2 Bead Experiments

To optimize the functionality of the optical layout, we used 15-μm-diameter polystyrene beads (18328, Polysciences, inc.) as test levitation targets. We suspended the beads in PBS and added a small amount of Triton X-100 (T8787, Sigma) (~0.01% by vol.) to act as a surfactant and decrease non-specific surface interactions. Adam Rosenthal provided SU-8 well array masters from a separate project. We replica molded the masters, forming a thin (~1-2-mm-thick) PDMS sheet of wells. We then plasma-bonded flow chambers, using the well array for the chamber floor as shown in Figure 2-6. We fabricated multiple well-array chambers; well diameters varied from 35- to 40-μm-diameter, well depth was 40 μm, and the PDMS gasket layer defining the chamber was 300-μm-thick, 8.3 mm long, and 4.3 mm wide.

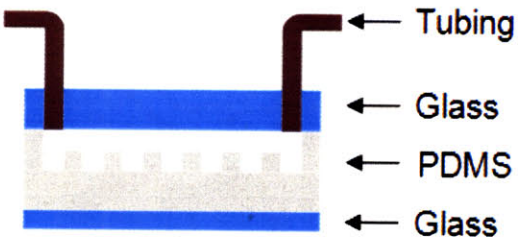

Figure 2-6: Cross-section of well array test chamber.

We injected the bead suspension into the chamber and allowed the beads to settle until all beads rested on the chamber floor or in wells (~2 min.). We first focused the laser onto beads settled in inter-well regions. As expected, application of the laser levitated beads. We then focused the laser on beads residing in wells and validated that we could levitate beads from the wells. An example with ~135 mW of optical power at 514 nm reaching the sample is shown in Figure 2-7.

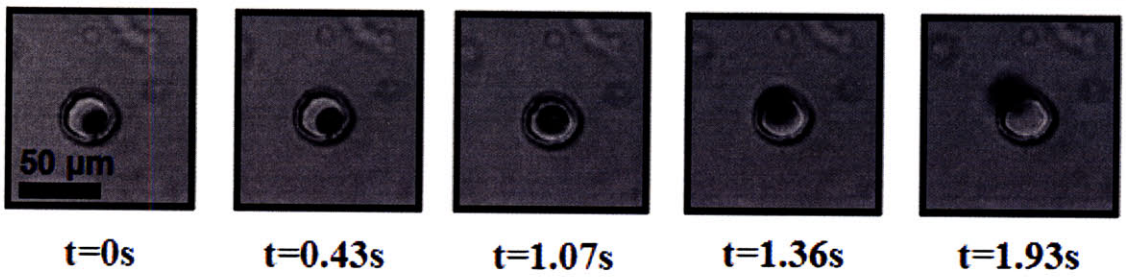

Figure 2-7: Levitation of bead from well with ~ 135 mW of power delivered to the sample.

We estimated the power delivered to the sample by determining the ratio between the output power of OBJ without the device in place and the laser output power. We used a handheld power meter (LaserCheck, Coherent) to measure power at the objective output when operating the laser at a low (< 1 mW) power level. We determined that the objective power / source power ratio was 0.68. The laser control panel allowed direct control of laser output power, implicitly allowing direct control of the power at OBJ. We assumed that the PDMS power absorption was negligible, and that all power from OBJ was delivered to the target.

We tested the sensitivity of the levitation to the position of the laser focal plane. We varied the location of L2, changing the focal plane of the laser, and recorded vertical bead displacement after an application of 2s of laser power at ~70 mW at the sample. We measured vertical displacement by focusing the image of the target bead, noting the z-position of the stage. We then applied laser power for 2 seconds and turned power off. We quickly adjusted the z-focus until the beam came into focus and recorded the new stage location. For these experiments, we used beads residing outside wells.

Using this measurement method, we tested the sensitivity of levitation to the beam focal plane location. We positioned lens L2 such that levitation force was optimized. We then moved L2 in 1 mm increments. We determined experimentally that a 1mm shift in the position of L2

corresponded to a shift in the laser focal plane of approximately 45 μm by examining the profile of the beam back-reflection in the CCD. Figure 2-8 illustrates that levitation was relatively insensitive to the laser focal plane location to within ~ +/- 100 μm.

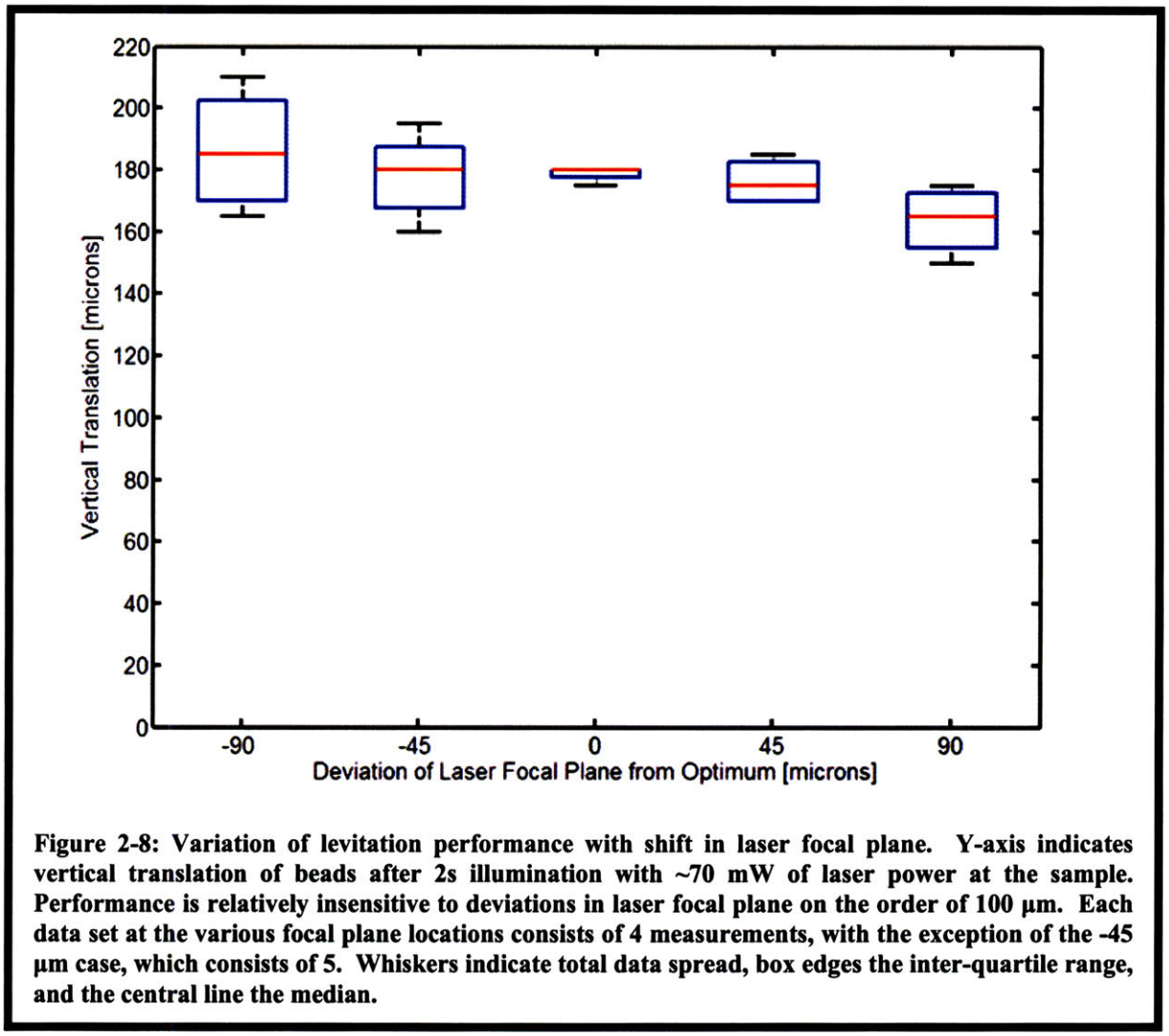

Figure 2-8: Variation of levitation performance with shift in laser focal plane. Y-axis indicates vertical translation of beads after 2s illumination with ~70 mW of laser power at the sample. Performance is relatively insensitive to deviations in laser focal plane on the order of 100 μm. Each data set at the various focal plane locations consists of 4 measurements, with the exception of the -45 μm case, which consists of 5. Whiskers indicate total data spread, box edges the inter-quartile range, and the central line the median.

We determined that the insensitivity shown in Figure 2-8 would suffice for fabrication variations we expected to find with PDMS pouring. We found that performance dropped rapidly for large laser focal plane shifts of ~400 μm or more (smaller shifts could have been equally detrimental; we did not thoroughly investigate this maximum allowable focal plane shift). Finally, the average forces implied by Figure 2-8 by use a Stokes drag calculation uncorrected for the boundary walls were ~15 pN, for a power to force ratio of ~ 5 mW/pN.

2.4.3 Cell Experiments

We next attempted to levitate cells. We injected cells into a test chamber and performed similar experiments to those shown in Figure 2-7. Cells were levitated, though not as quickly as beads at equivalent power levels.

The most noticeable phenomenon was a general "swarming" effect where all cells moved to the beam focus. This behavior was not restricted to cells immediately around the laser focus. Cells millimeters away from the focus were drawn to the focus in an inward radial flow.

The flow was likely thermal, as optical gradient forces would only persist tens of microns from the laser focus. The thermal flow was very large when the top of the chamber was open to air, and dropped considerably when the chamber was closed. Surface tension (and therefore surface tension-gradient-induced flow) is temperature-dependent [26]. We can approximate the extent to which temperature-based surface tension effects can induce flows in the case of a hemispherical droplet resting on a surface.

At any point on the interface between two fluids, a stress balance at the interface states that

$$\tau_{nt}|_2 - \tau_{nt}|_1 + \underline{t} \cdot \nabla_S \gamma = 0, \tag{2.1}$$

where $\tau_{nt|1}$ and $\tau_{nt|2}$ are the shear stresses at the interface in fluids 1 and 2 respectively, $\underline{t}$ is the unit tangential vector of the droplet, ∇_S is the surface gradient operator, and γ is the surface tension [27]. First, we assume that the stress in the air, fluid 2, is negligible. We can approximate the stress in the droplet, fluid 1, as

$$\tau_{nt}|_1 \sim \mu \frac{V}{R}, \tag{2.2}$$

where μ is the viscosity, V is the characteristic velocity at the droplet surface, and R is the droplet radius. We can approximate the gradient in surface tension due to thermal gradients as

$$\nabla_S \gamma \sim \frac{\Delta\gamma(T)}{R}, \tag{2.3}$$

where the change in surface tension is taken from the top of the hemispherical droplet to the point of the solid/liquid/air interface. Equating these two terms, we find that

$$V \sim \frac{\Delta\gamma(T)}{\mu}. \tag{2.4}$$

The surface tension between air and water is 7.197e-02 N/m and 7.118e-02 N/m at temperatures of 25° C and 30° C respectively, and the viscosity of water is approximately 1cP [26]. Linearizing the temperature dependence of surface tension, a small thermal gradient across the drop of 0.1° C would yield a surface tension difference of ~ 1.58e-05 N/m, resulting in a characteristic flow velocity estimate of 16 mm/s. While this modeling is admittedly crude, it illustrates the capacity that small temperature gradients have to induce flow through surface tension effects, even if the resulting velocities were orders of magnitude lower than this estimate.

Closing the chamber eliminated much of the effect, presumably because doing so removed the air-liquid interface and associated surface tension. However, some thermal flows were still apparent after closing the chamber. These flows were slow, on the order of ~ 5 μm/s when the sample was illuminated with ~350 mW of optical power. Flow velocities scaled directly with power. Figure 2-9 illustrates these flows at 350 mW sample power with an enclosed chamber.

(A)

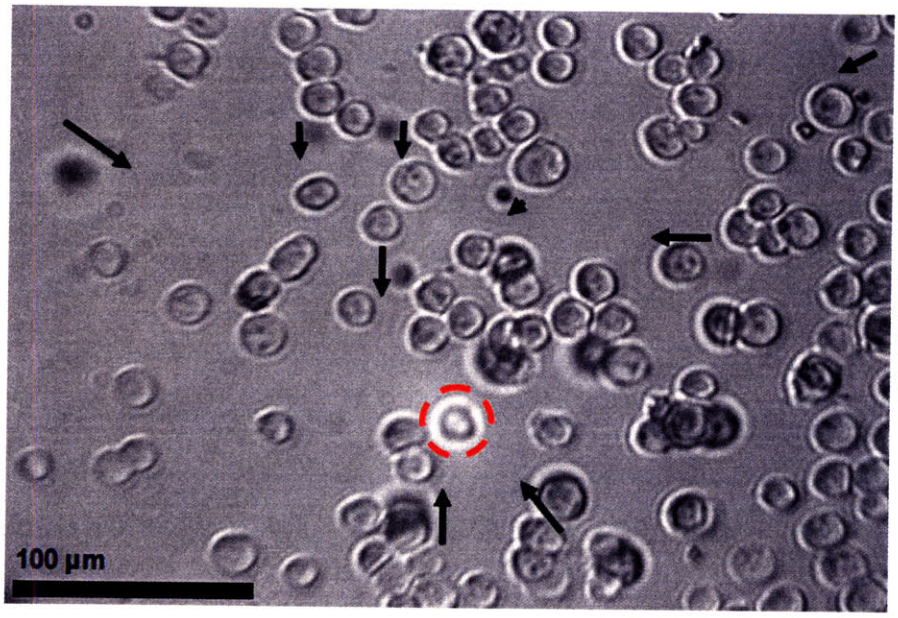

(B)

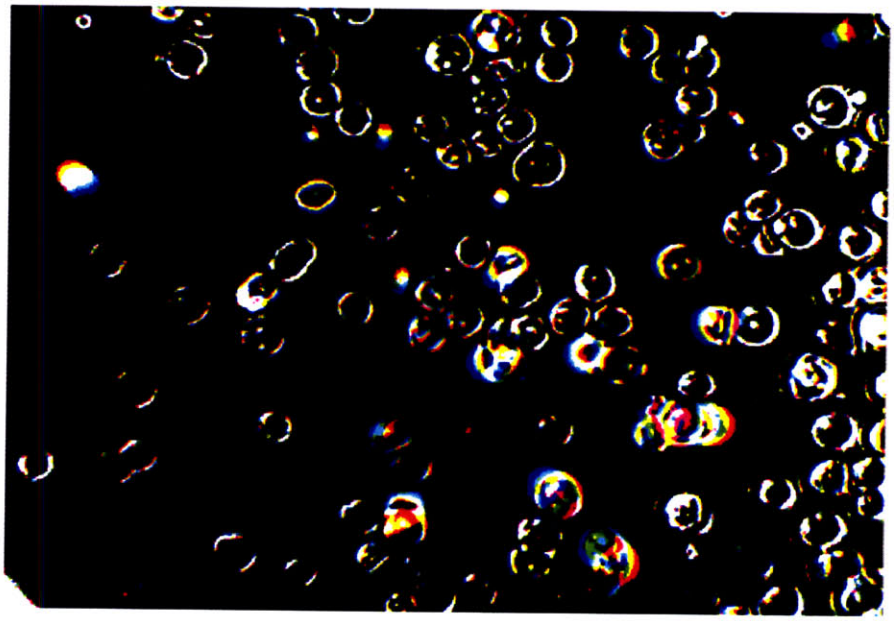

Figure 2-9: Illustration of thermal flows. A) illustrates the directions of cell motion for cells not stuck to the chamber floor when the laser is on. The laser focus is indicated by the dashed circle. B) is a composite image of three frames taken over a time course of ~ 2 seconds. Frame 1 composes the red channel, 2 the green, and 3 the blue, making position shifts apparent. We used this image to create the direction arrows in A).

It is possible that the heating effects could cause the upward levitation force on the particle. As fluid in the laser path heats, the local fluid density decreases. It is likely that the temperature profile due to the heating would not be perfectly axisymmetric. This would cause the heated fluid to rise in some regions, inducing upward flow in the vicinity of the beam.

To ensure that the dominant force levitating the cells was radiation pressure rather than thermal flows, we rebuilt the optical layout with the beam directed downward onto the target rather than upward. We injected cells into the chamber and focused the laser onto cells before they settled. Cells were definitively pushed downward when illuminated by the laser. Downward cell velocities were qualitatively similar to previous upward velocities, suggesting that the thermal levitation effects were significantly smaller than radiation pressure levitation effects. We were then satisfied that we could exert significant radiation pressure-based levitation forces on cells. When cells were trapped in wells, we expected the far-reaching thermal flows to be inconsequential.

For completeness, we validated that levitation occurred with cells while using an infrared (IR) 980 nm laser diode source, which would be less biologically damaging for the cell. The optical setup was similar to our optical testing layout. The setup belonged to the Lang lab, and was only roughly performance-optimized with respect to beam positioning and profile. Nonetheless, we were able to exact levitation forces with power levels comparable to the 514 nm source used above, though required irradiation times were ~ 5-10 times longer. System optimization would likely bring these parameters closer to the results shown above.

2.5 Optical Force Theory

Modeling optical forces exerted on a dielectric particle can be simple, provided that appropriate approximations can be made. We will investigate modeling of optical forces exerted by focused and unfocused beams on dielectric spheres. There are two regimes where simplifications can be made; we will examine behavior first in both of them, and then consider behavior between the regimes.

The first regime considers particles much smaller than the wavelength of the incident light. Gradient forces in this regime reduce to the quasi-static dielectrophoretic force, F_G,

$$\langle F_G \rangle = \left(-\frac{n_m{}^3 r^3}{2} \right) \left(\frac{m^2 - 1}{m^2 + 2} \right) \nabla \langle E^2 \rangle, \tag{2.5}$$

where n_m is the refractive index of the suspending medium, r is the particle radius, <·> denotes time-averaging, and $m=n/n_m$ is the relative refractive index of the particle [12]. If the refractive index of the particle exceeds that of its suspending medium (i.e. as with cells), the gradient force will seek to push the particle to the brightest point (i.e. pDEP). If the converse is true, such as with bubbles in water, the gradient force will push the particle to the point of lowest brightness (i.e. nDEP). The beam also exerts a scattering force, F_S, on the particle in the direction of the Poynting vector, S,

$$\langle F_S \rangle = n_m \frac{\frac{8}{3} \pi (kr)^4 r^2 \left(\frac{m^2 - 1}{m^2 + 2} \right)^2 \langle S \rangle}{c}, \tag{2.6}$$

where k is the wave number, and c is the speed of light [12]. Unfortunately, we cannot use these simple equations, because cell diameters are roughly 10 times that of our proposed wavelength of ~ 1 μm.

The second limiting regime is that where the particle size is much larger than the wavelength. In this regime, the ray-optics regime, the incident light can be decomposed into rays each carrying a power P. Derivation of the force amounts to tracing all reflected and refracted rays, calculating the net momentum change of all photons, thereby inferring the force applied to the sphere. The following derivation follows from Ashkin [13].

Ashkin first traced a ray incident upon circle with angle θ, as illustrated in Figure 2-10.

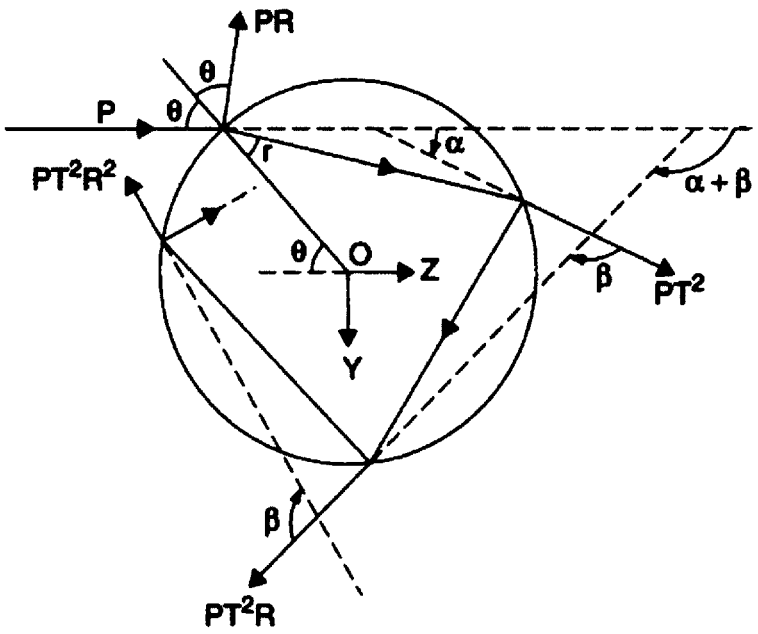

Figure 2-10: Generalized ray trace for optical force derivation. A beam with power *P* strikes the sphere with an angle *θ* relative to the sphere surface normal. A fraction of power is reflected along *PR*, and a fraction is refracted at angle *r*, giving rise to an infinite number of reflected and refracted beams with geometrically decreasing intensity. A momentum balance yields the forces resulting at the center of the sphere in the Y and Z directions, which act perpendicular and parallel to the incident beam direction respectively. (Figure from [13].)

Recognizing that force is change in momentum per second, application of a momentum balance to the incoming photons in the beam of power P indicates that the forces applied to the sphere in the Z and Y directions are

$$F_Z = F_S = \frac{n_1 P}{c}\left[1 - R\cos(\pi + 2\theta) - \sum_{n=0}^{\infty} T^2 R^n \cos(\alpha + n\beta)\right], \tag{2.7}$$

$$F_Y = F_G = \frac{-n_1 P}{c}\left[R\sin(\pi + 2\theta) + \sum_{n=0}^{\infty} T^2 R^n \sin(\alpha + n\beta)\right], \tag{2.8}$$

where n_1 is the refractive index of the suspending medium, R is the Fresnel reflection coefficient, and T is the Fresnel transmission coefficient, making the forces polarization-dependent [13].

Further algebra by Ashkin [13] concluded that these infinite series converge to

$$F_Z = F_S = \frac{n_1 P}{c}\left\{1 + R\cos(2\theta) - \frac{T^2\left[\cos(2\theta - 2r) + R\cos(2\theta)\right]}{1 + R^2 + 2R\cos(2r)}\right\}, \tag{2.9}$$

$$F_Y = F_G = \frac{n_1 P}{c}\left\{R\sin(2\theta) - \frac{T^2\left[\sin(2\theta - 2r) + R\sin(2\theta)\right]}{1 + R^2 + 2R\cos(2r)}\right\}. \tag{2.10}$$

The total force imparted to a sphere is simply the vector sum of forces from all rays incident on the sphere, a problem which can directly utilize the results derived for incidence on a circle. The relationship between the two problems is illustrated in Figure 2-11. The path of each ray passing through the input aperture must simply be traced to an incidence angle with the sphere, allowing the results of the circular derivation to be applied. The forces exerted by all beams passing through the planar input aperture can be summed to yield the net forces in the *X*, *Y*, and *Z* directions, enabling the modeling of the force exerted by an arbitrary beam shape.

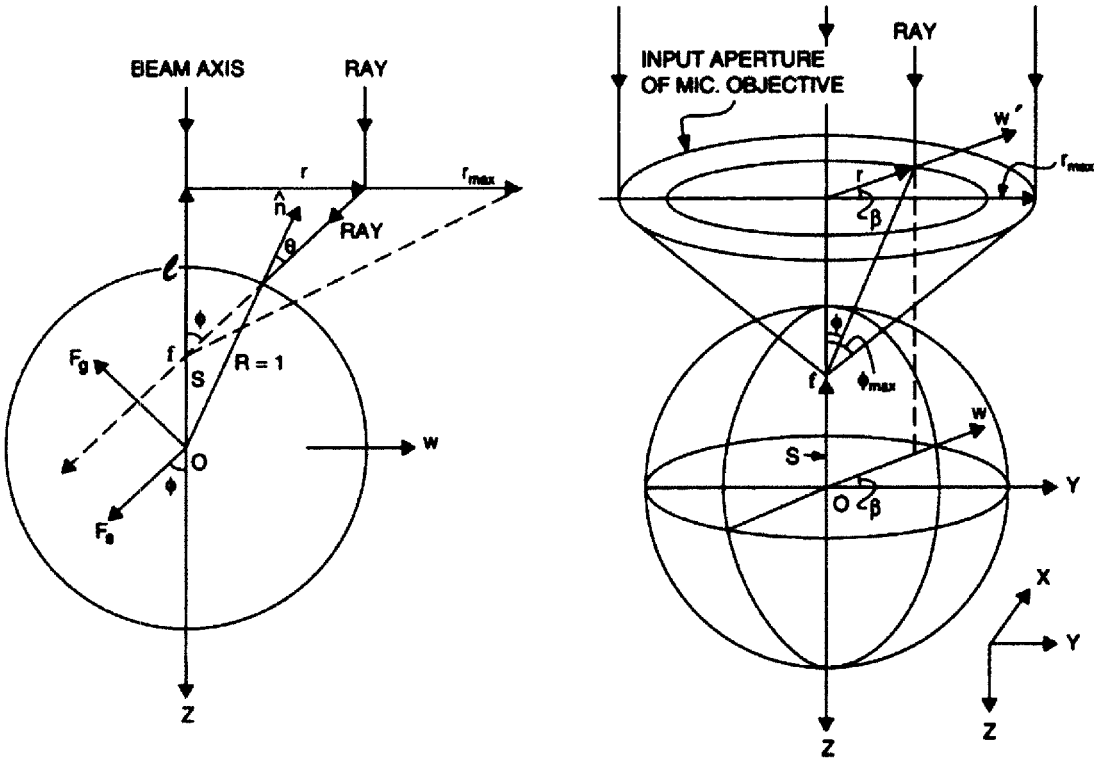

Figure 2-11: Determination of the total force imparted to a sphere. In the circular picture, we see that a ray with incident angle ϕ relative to the beam axis and angle θ relative to the sphere normal imparts a total force in along the beam axis of $F_S \cos(\phi) - F_G \sin(\phi)$. Therefore, summing over all incident beams striking the sphere as implied in the spherical picture yields the total force applied to the sphere. (Figure from [13]).

The ray-optics model applies nicely to the situation often found in optical tweezers and mammalian cells: the cell is much larger than the wavelength, and the beam is sufficiently convergent that diffraction effects are negligible in modeling the beam profile around the target. If the aperture of a lens is uniformly filled by a collimated beam, we recall that the resulting focused spot diameter is

$$d = \frac{1.22\lambda}{NA}, \tag{2.11}$$

where d is the width of the main intensity lobe, NA is the numerical aperture of the uniformly filled lens, and λ is the wavelength of the beam. Therefore, for NA close to 1, and assuming a wavelength of ~1 μm, spot sizes are on the order of 1-2 μm in most optical tweezers applications. If we sought to model forces with cell diameters of 10-20 μm, the effects of diffraction would be negligible if we used high-NA optics.

Unfortunately, from a modeling perspective, diffraction effects are significant for us. We attempt to create a spot size matching that of the cell; a larger spot size would waste power as energy missed the cell, and a smaller spot size would create lower net z-directed forces, due to higher gradient forces opposing the scattering force. In addition, smaller spot sizes create larger local intensities, potentially damaging cells.

In order to illustrate the effects of diffraction at low-NA, we calculated the intensity field for a plane wave focused through a lens with a uniformly illuminated aperture. The resulting intensity profile, $I(r,z)$, with the r-z origin located at the lens focal point, is

$$I(r,z) = \left(\frac{2}{u}\right)^2 \left[U_1^2(u,v) + U_2^2(u,v)\right] I_0, \tag{2.12}$$

where

$$u = \frac{2\pi}{\lambda}\left(\frac{NA^2}{1-NA^2}\right) z, \tag{2.13}$$

$$v = \frac{2\pi}{\lambda}\left(\frac{NA}{\sqrt{1-NA^2}}\right) r, \tag{2.14}$$

NA is the numerical aperture, and U is the Lommel function, defined as

$$U_n(u,v) = \sum_{s=0}^{\infty} (-1)^s \left(\frac{u}{v}\right)^{n+2s} J_{n+2s}(v), \tag{2.15}$$

where $J_n(v)$ is a Bessel function of the first kind [28, 29]. We plotted this intensity profile as we varied NA. Figure 2-12 illustrates the results. We note that in the case of 0.1 NA, the focused spot is ~ 200 μm long in z, while it is ~10 μm wide in r. We further illustrated the case of 0.1 NA by showing more detailed iso-intensity plots, both un-scaled and scaled, in Figure 2-13.

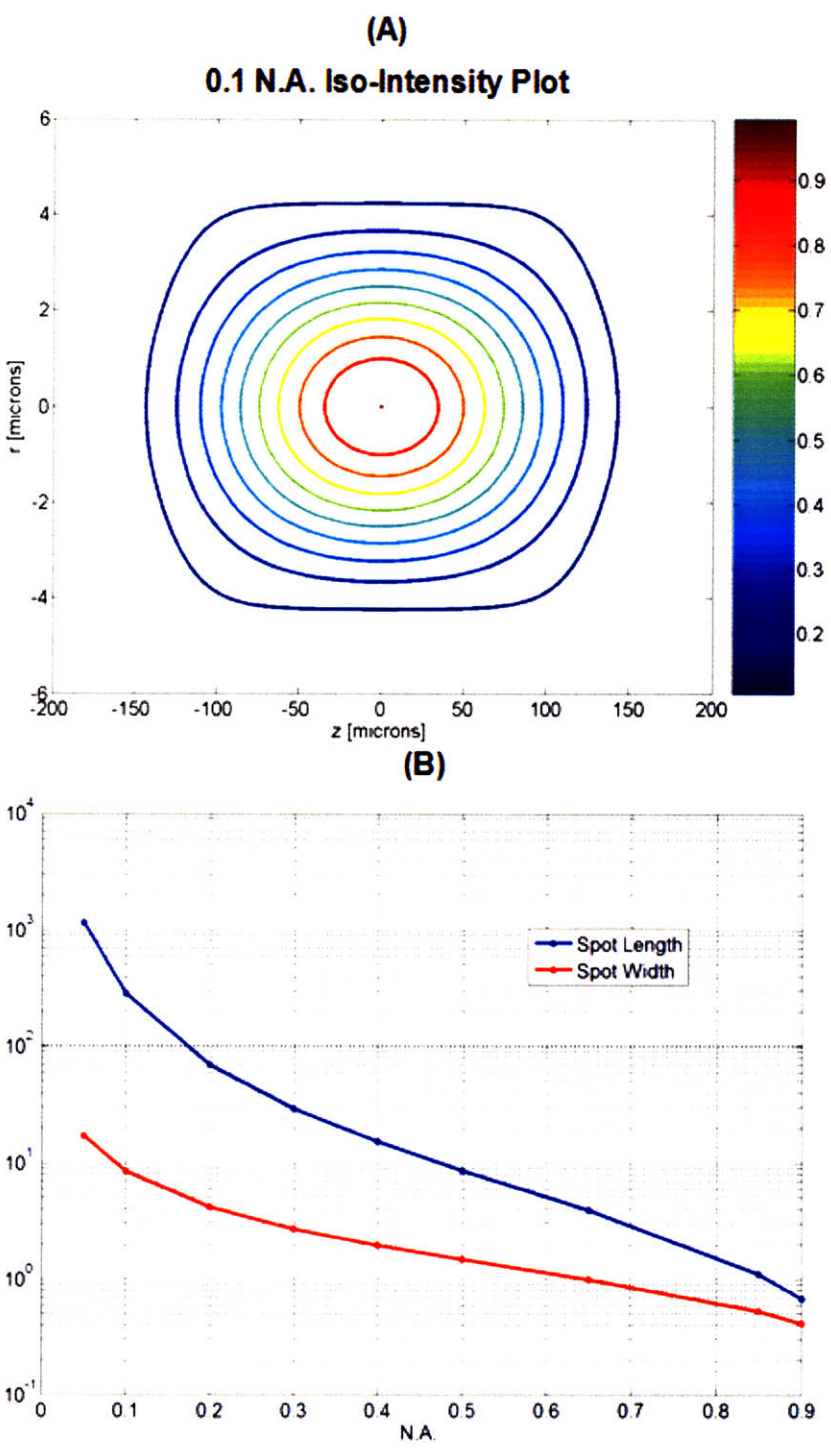

Figure 2-12: Ideal focusing of a 980 nm laser which uniformly fills the back of a lens of a given NA A) Normalized iso-intensity plot for case of 0.1 NA. B) Variation of spot width and length with NA. We define the spot width as the distance through the *z=0* plane across which intensity is greater than 10% of the maximum intensity. Spot length is defined as the distance through the *r=0* plane through which intensity is greater than 10% of the maximum intensity.

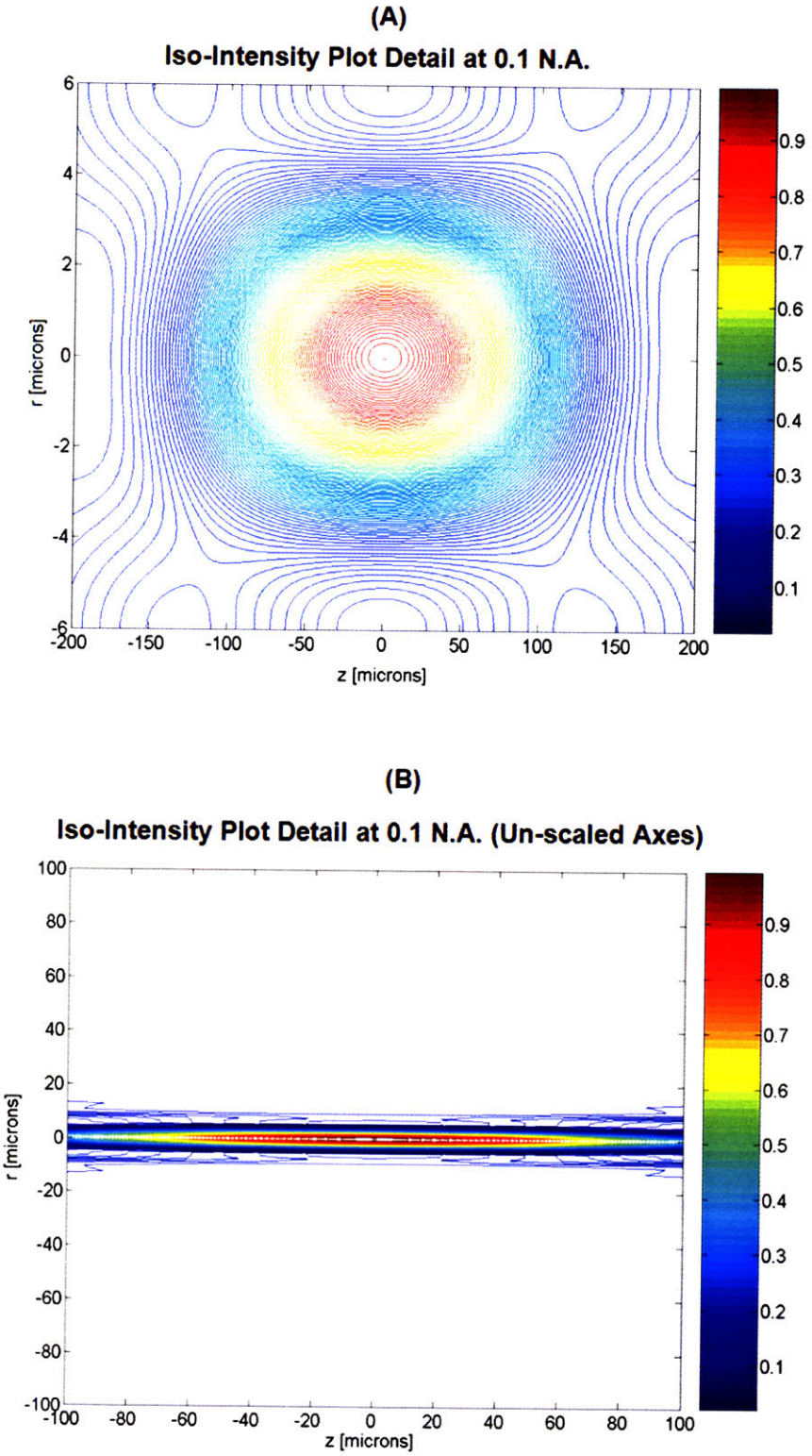

Figure 2-13: Detail of beam intensity for beam focused at 0.1 NA. A) Both axes are scaled. B) Axes have indentical scaling to emphasize beam shape near the focus. Spot width in *z* is roughly 30-times that in *r*.

After examining Figure 2-12 and Figure 2-13, we concluded that simple ray-tracing to derive forces would be inaccurate; diffraction causes the power distribution around the cell to be different from the conical distribution ray-tracing would predict. Initially, the 0.1 NA beam appears to be "quasi-collimated" over the distance relevant to a 20-μm-diameter or smaller cell. However, a somewhat uniform intensity profile over the range of interest does not strictly imply that the beam can be treated as collimated over that region.

The force exerted on the cell could be calculated by computing the electric field distribution in the presence of the cell. The magnitude of the power transfer to the cell would be the integral of the Poynting vector across the surface of the cell, and this power is proportional to the force. Such a solution would require a numerical solution, and does not yield great intuition. The numerical solution is especially difficult because numerical element sizes must be much smaller than the wavelength. Additionally, the particle is much larger than the wavelength, therefore requiring that the total numerical grid be enormous. We attempted to use finite-element methods, but the grid size made such a solution intractable.

We can predict that the force exerted on the cell will lie between the forces predicted by two bounding cases. The lower-bound force would be that where diffraction is neglected, simply using a ray-tracing method to determine the force as described earlier. In this case, beam divergence is overstated, reducing the scattering force, and decreasing the net axial force as the cell moves out of the focus, since gradient forces will attempt to restore the cell into the focus.

The upper-bound case would be the force exerted by a collimated beam; in this case no gradient force can oppose the scattering force in z, as there is no beam divergence. The divergence close to the focus, which diffraction serves to degrade, can never be as low as that of a collimated beam, which has no divergence, i.e. an NA of 0. The actual diffraction-limited beam divergence will lie somewhere between the two cases. Therefore, we calculated the forces for both bounding cases to determine if the cases were reasonably close to one another.

We first simulated the diffraction-free case with various values of NA, a suspending media refractive index of 1.34 to simulate saline, and a particle refractive index of 1.41 [30] to simulate the nucleus comprising the dominant scattering part of the cell (implicitly approximating that the nucleus filled the cell, a decent approximation for unattached cells). We simulated an incident power of 100 mW with circular polarization, and plotted the total axial force versus location of the cell relative to the focus. We expressed the distance from the focus in terms of S, the number of cell radii by which the cell was removed axially from the focus, as illustrated in Figure 2-14.

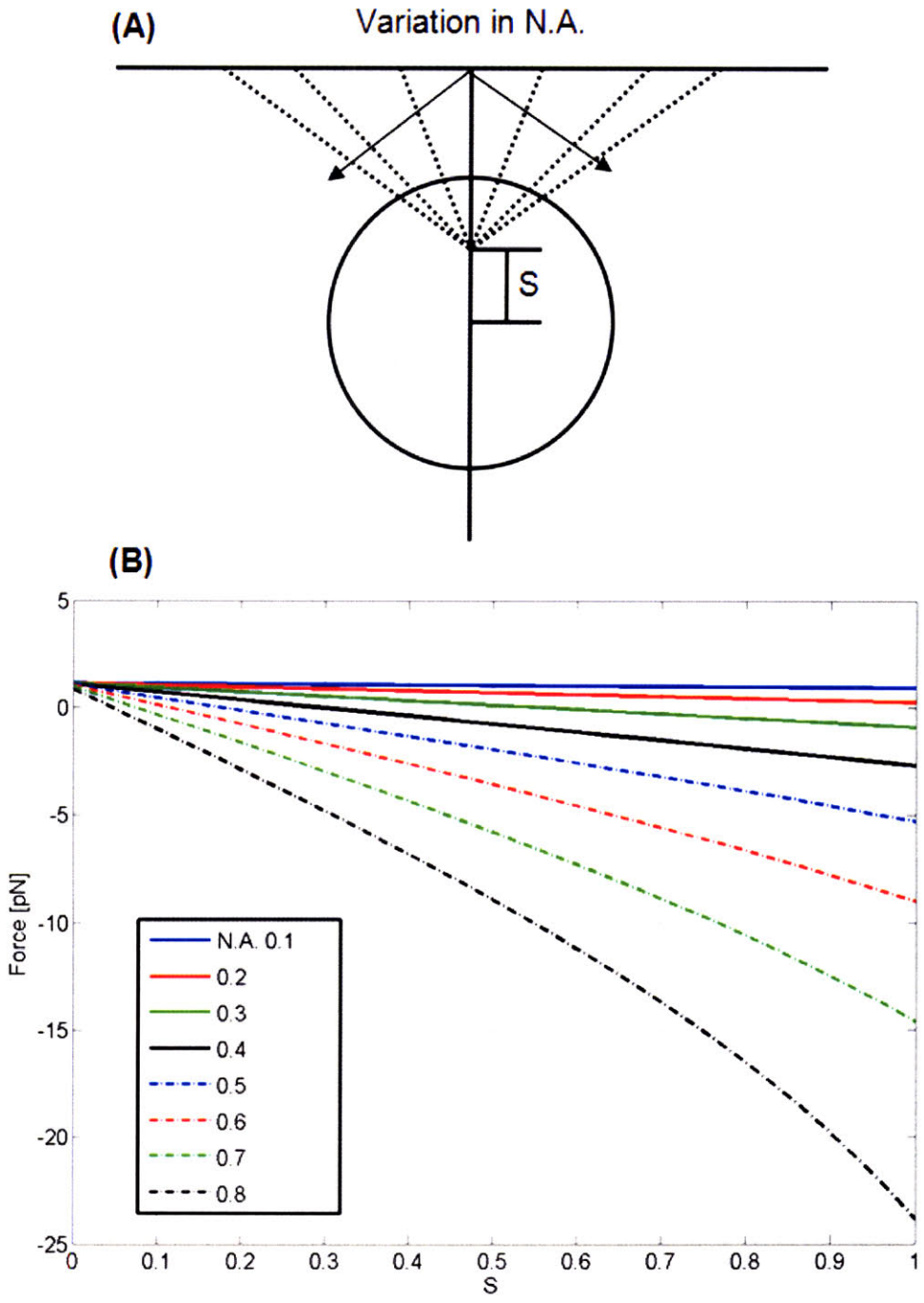

Figure 2-14: Axial position dependence of total axial force exerted on cell. A) Illustration of modeling experiment. We varied the NA of the diffraction-less beam to predict the total axial force versus cell location relative to the focus. *S* expresses axial distance from the focus in terms of cell radii; a value of *S=1* corresponds to the cell membrane being in the focus. B) Force vs. position and NA for a 100 mW, circularly polarized input beam. Force increases in magnitude slightly beyond *S=1*, and then asymptotically approaches 0 N. Simulating *S>1* is difficult; here we plot only *S<1*. Positive forces indicate forces acting in the direction of beam propagation; negative forces imply a stable trap in *z*.

Neglecting diffraction, using an NA of 0.1, we predicted a minimum total axial force of 0.93 pN, which occurred at $S=1$. When modeling a 100 mW circularly-polarized collimated beam, we predicted a force of 9.2 pN. In the diffraction-less case, rays are concentrated to a small range of small incidence angles concentrated at the top of the cell. The Fresnel reflection coefficients are much smaller at shallow angles than at larger angles. In the diffraction-less case, all angles are shallow (< ~6°) with an NA of 0.1. In the collimated case, however, incidence angles approach 90° as the beam strikes the outer edge of the cell. The Fresnel reflection coefficients become large at these steep angles, causing much larger reflectivity near the outside edges of the cell cross-section. The force contribution of each part of the cell relative to the maximum contribution is illustrated in Figure 2-15 for the collimated case.

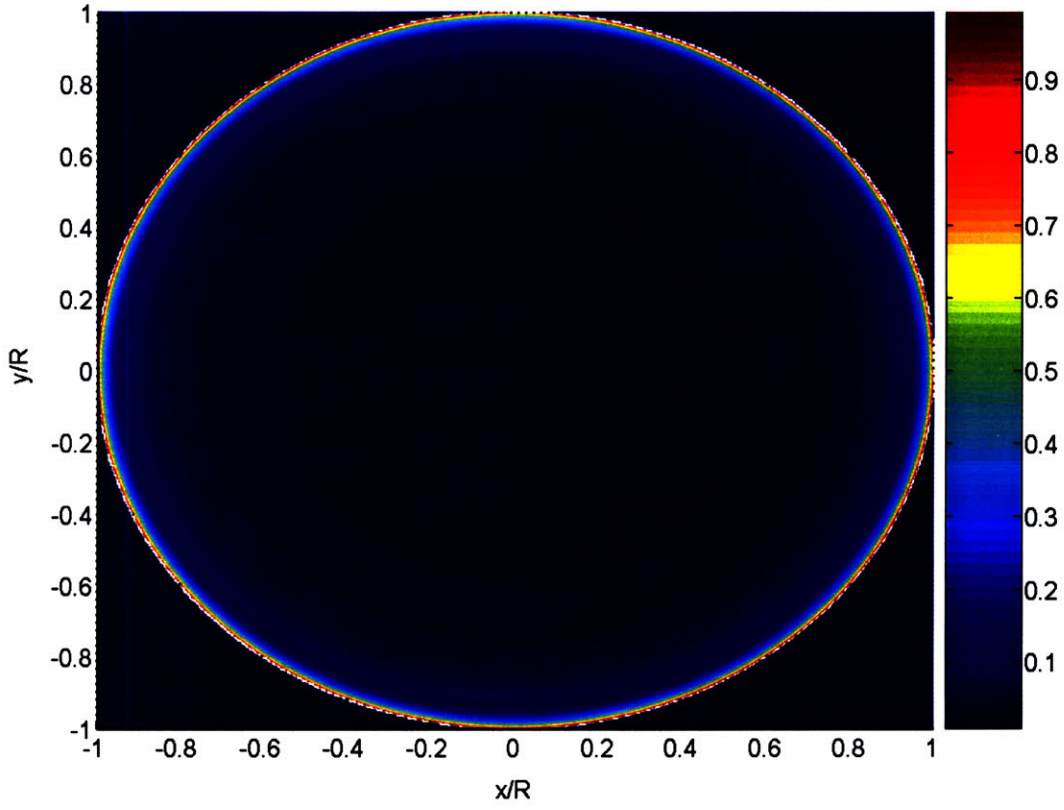

Figure 2-15: Normalized regional scattering force contributions in different regions of the cell . The edges of the cell contribute disproportionately due to the rapid increase in the Fresnel reflection coefficient at the edges, where the incidence angle approaches 90°.

The diffraction-less case concentrates all rays to the central region of the plot in Figure 2-15. We plot the Fresnel reflection coefficients in Figure 2-16. The coefficients are much higher for large incidence angles than for shallow angles. The degree to which reflection at these steep angles actually contributes to the net axial scattering force for a collimated beam, however, is not quite as drastic as the Fresnel coefficients might suggest. The total contribution to the axial scattering force is much more complex, and is impacted by the increasing non-linearity of Snell's law at high incidence angles, and by the weighted contributions of the force terms given in eqs. (2.9) and (2.10).

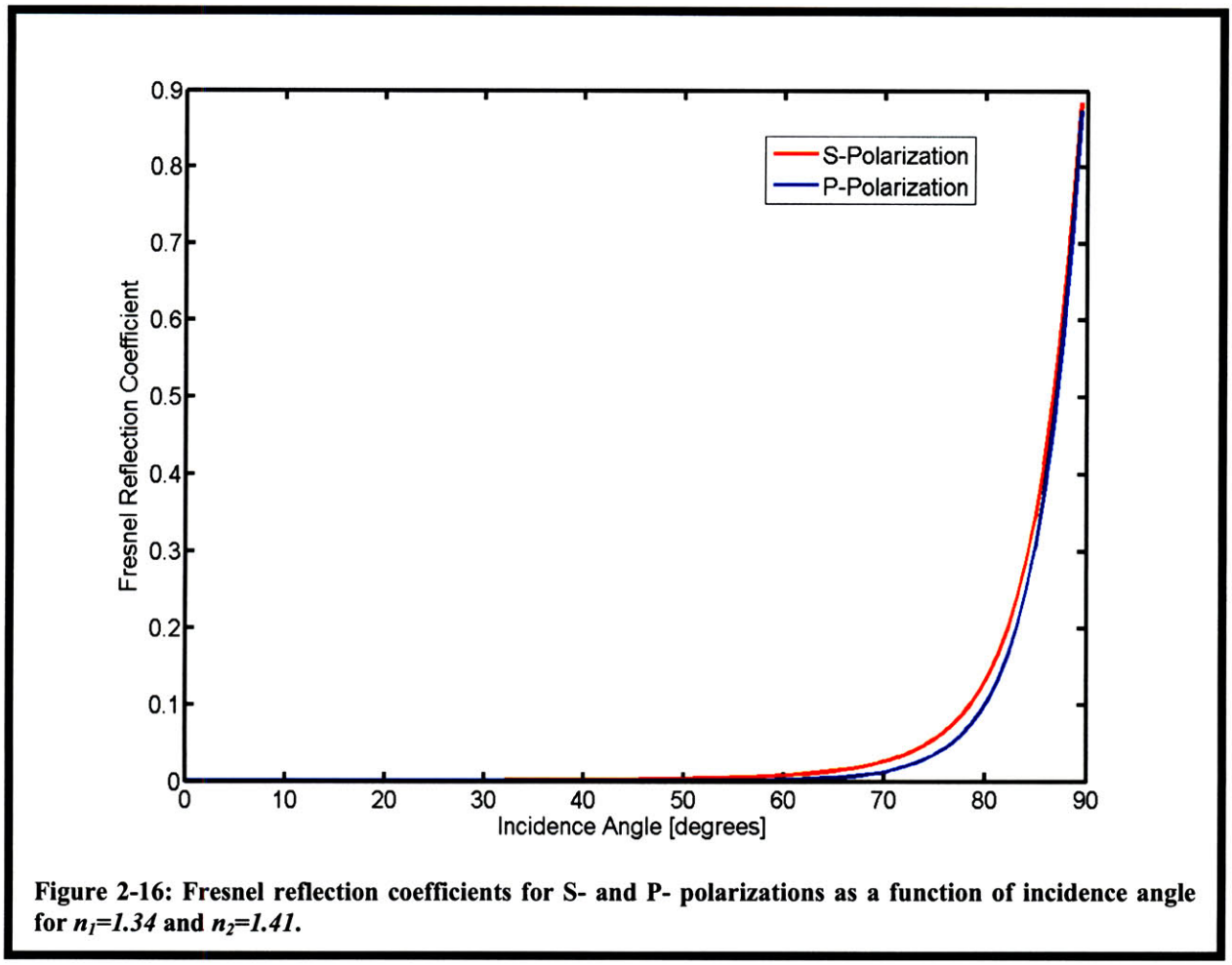

Figure 2-16: Fresnel reflection coefficients for S- and P- polarizations as a function of incidence angle for n_1=1.34 and n_2=1.41.

The correct answer lies somewhere between the two predictions. Therefore, in the case of low-NA, using a simple ray-optics approach to modeling will predict forces roughly within an order of magnitude of the diffraction-limited case. The end result is that modeling predicts that the force should be on the order of a few piconewtons per hundred milliwatts, which is exactly the neighborhood of forces our experiments suggested which we will describe in Chapter 3. Ultimately, we seek to know that we are operating close to optimal levels; it is not critical to exactly predict forces in our application.

2.6 Device Design Considerations and Layout

We used a two-layer SU-8 process, allowing the flow chamber gasket and the chamber floor features to be created after a single PDMS pour and cure. Pouring a separate gasket layer requires a potentially leaky PDMS-PDMS bond to seal the chamber. We anticipated leaks as a potential problem, as we would inject fluids at high pressure to purge air bubbles from the wells.

The first design was a well array, which required patterning posts in the SU-8. At the beginning of the chamber, post diameters were 20 μm. We designed an array with this post dimension 2mm wide and 1mm long. At 1mm down the length of the chamber, we increased the diameter to 25μm and created a 2mm by 1mm array at the larger post size. We continued making similar arrays down the length of the chamber, with diameters of 20, 25, 30, 35 and 40 μm, and then from 40 μm to 170 μm in 10 μm increments. These large variations in array size

made our devices compatible with small, non-adherent cells as well as adherent cells which needed room to spread after attachment. Well depth was be ~ 50μm, which would still allow levitation from small wells but afford reasonable hydrodynamic shielding for larger wells.

The flow chamber was to be 40mm long and 3mm wide. The total area for the posts was 2mm wide and 18mm long, allowing the objective to easily access the wells, regardless the side used for tubing mounts. Variations of the device used inter-well spacing of 10, 20, 40 and 80 μm, allowing determination of the minimum allowable spacing which still formed distinct wells. A section of the mask used to create the well arrays is shown in Figure 2-17.

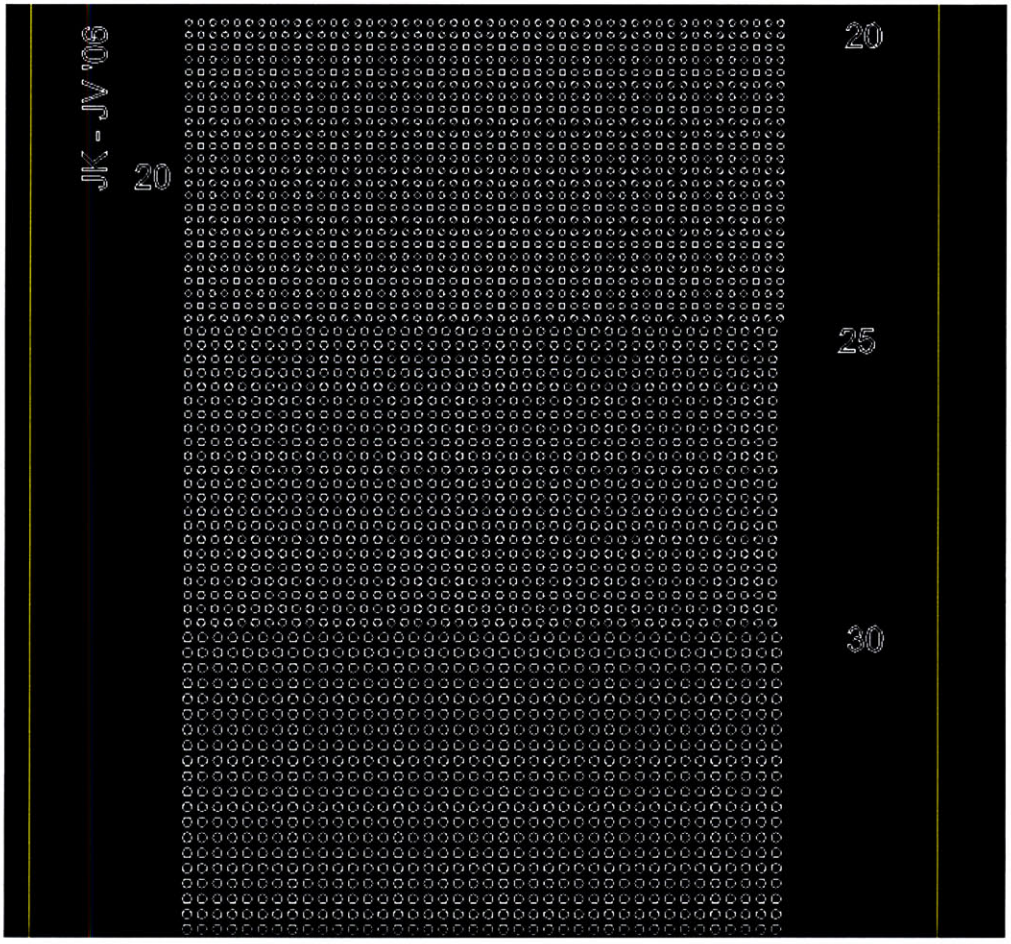

Figure 2-17: Well array layout. We created 1mm x 2mm arrays of wells of size ranging from 20 μm to 170 μm in diameter. We increased diameter monotonically along the length of the device, while well diameter remained constant along the width of the device.

We also made a layout for an alternative design. The design did not utilize a well architecture and was an offshoot of an alternative design by Brian Taff, and is known as the "pachinko" architecture [31]. In this design, cells flow into the chamber and are trapped behind specially designed structures, as illustrated in Figure 2-18.

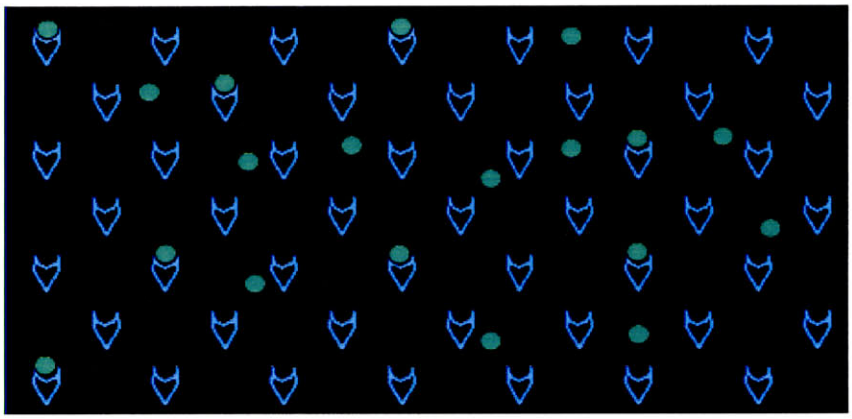

Figure 2-18: Schematic illustration of operation of pachinko architecture. Cells flow past structures; some are trapped. Un-trapped cells are channeled towards other traps. Release is accomplished either by levitation over the structure or by tweezing the cell to the side of the structure. Non-staggered designs might work better for the latter release mechanism, allowing lower probability of re-trapping after release. We incorporated both grid-packed and staggered-packed designs.

Release would be accomplished either by levitating the cell over the top of the structure or tweezing the cell around the structure and into the flow field; low NA optics allow brief tweezing to be applied to cells before they are pushed upwards. Our layout of the pachinko architecture varied the size of pachinko shapes (24 μm wide vs. 80 μm wide) as well as spacing between the shapes (120 μm to 830 μm) and pattern (grid-packed vs. interleaved-packed).

2.7 Device Fabrication and Packaging

The process was a two-level SU-8 process, as illustrated in Figure 2-19. We used 6-inch wafers in the first run. There is no SU-8 6-inch chuck for EV1. The vacuum applied by the 4-inch chuck does not hold the 6-inch wafer firmly to the chuck. Consequentially, any indentations by wafer-handling tools in the edge bead tended to scrape across the mask, grossly moving the wafer as it was inserted into EV1. This issue was somewhat resolvable by ensuring that the wafer was pressed down to maximize vacuum, but the process was finicky. We used 4-inch wafers in subsequent runs, sacrificing a large number of devices.

A larger problem was that after the wafer was inserted for alignment with mask 2, EV1 would bring the mask in contact with the wafer before pulling the mask back for the programmed hold-off separation. However, some points on the SU-8 would stick to the mask, preventing alignment of the second layer to the first layer. Sticking mostly occurred at points where wafer-handling tools had contacted the edge bead.

We circumvented the problem by covering these trouble spots with thin green tape located by the "green" tools in the EV1 photolithography room. While this fixed the sticking problem and allowed alignment, the fix is not ideal because the mask did not come into uniform

separation across the wafer, decreasing resolution and increasing feature size. However, the method was sufficient for our device and was the only way found to permit the process to work.

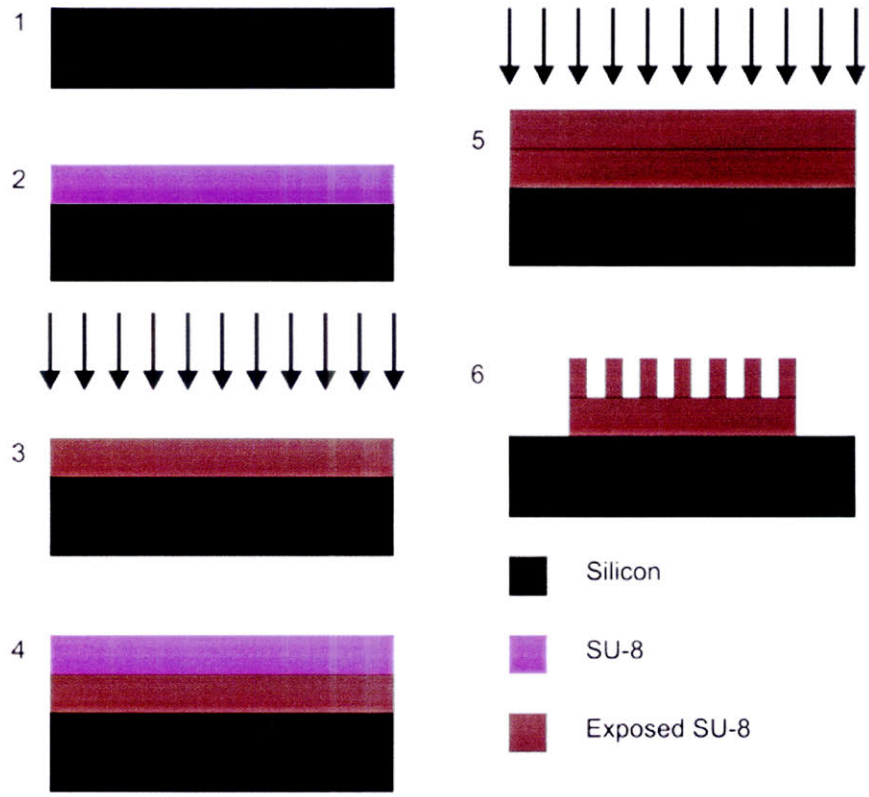

Figure 2-19: Cross sections of process flow. 1) Starting substrate is a test-grade silicon wafer. 2) SU-8 spin-on and pre-bake. 3) Expose mask 1, post-bake. 4) SU-8 spin-on and pre-bake. 5) Expose mask 2, post-bake. 6) Develop.

A single-layer SU-8 process where the gasket layer is fabricated separately would be far simpler. Such a process would allow tighter control of features and easier photolithography with EV1. However, the utility of this method would hinge on the ability to make strong PDMS-PDMS bonds able to withstand high injection pressures, which may or may not be possible.

Another challenge was delamination of the SU-8 from the wafer. Delamination was greatest for the pachinko devices, as the master for these devices consisted of two gasket layers, with the top layer having small "anti-pachinko" holes. In contrast, the well-arrays consisted of a gasket layer with small posts. The pachinko devices consequentially suffered from larger thermal mismatch stresses which caused more pronounced peel-off.

Delamination was pronounced for both pachinko and well array devices after the first fabrication run. Delamination occurred at the edges of the gasket layers. On the second run, we made an effort to transfer the wafer between the dehydration bake and the first spin-coating more quickly. Second, we used a 40 minute prebake on the first layer versus a 15 minute prebake. Third, we took care to develop the SU-8 only as much as was absolutely necessary. The result was that the well-array devices did not delaminate, and that the pachinkos showed less delamination. Pachinko devices still delaminated after a few PDMS pour and cure cycles; in contrast, after the first fabrication run, nearly all pachinko devices were destroyed after a single pour. Table 2-6 summarizes the final successful process.

Table 2-6: Process flow for two-layer SU-8 process

Step	Equipment	Description	Process / Time
1	None	Substrate	Si wafer; test grade
2	Hotplate	Dehydration Bake	200° C / 30 min
3	SU-8 Spinner	SU-8 Spincoat-2050 (~90 μm thickness)	Pour enough SU-8 to halfway cover wafer, allow to flow to edge. Ramp to 500 rpm @ 100 rpm/s, hold 5-10 s; Ramp to 1680 rpm at 300 rpm/s, hold for 30s.
4	Hotplate	Prebake	65° C for 4 min; ramp to 95° C, keep at 95° C for 15 min., ramp down to 65° C. Note: 40 min. @ 95° C seemed to reduce delamination problems.
5	EV1	UV Expose	Mask 1, 30 s., 30 μm separation (SU-8 will likely contact and stick; be prepared)
6	Hotplate	Post-Expose Bake	65° C for 1 min., ramp to 95° C for 10 min., ramp down to 65° C to cool
7	SU-8 Spinner	SU-8 Spincoat-2050 (~45 μm thickness)	Pour enough SU-8 to halfway cover wafer, allow to flow to edge. Ramp to 500 rpm @ 100 rpm/s, hold 5-10 s; Ramp to 3050 rpm at 300 rpm/s, hold for 30s.
8	Hotplate	Prebake	65° C for 4 min; ramp to 95° C, keep at 95° C for 40 min., ramp down to 65° C.
9	EV1	UV Expose	Mask 2, 23 s., 30μm separation (SU-8 will likely contact and stick; be prepared)
10	Hotplate	Post-Expose Bake	65° C for 1 min., ramp to 95° C for 10 min., ramp down to 65° C to cool
11	Solvent - Au	Develop	~7-10 min., visual stop
12	EML Acid Hood	Silanization	Place 3-4 drops of HMDS into cup in vacuum jar. Place wafer(s) against wall of jar. Close jar, turn on vacuum for 5-10 minutes, turn vacuum off, let sit for 1 hour, vent.

Some posts for the well arrays had aspect ratios as high as 2.5; post heights were ~50 μm, and the smallest post diameters were ~20 μm. These posts have withstood more than 20 PDMS pours without incident, demonstrating the adhesion strength between layers of SU-8 (these posts reside on the SU-8 gasket layer). These findings suggest that depositing a thin (~10 μm) unpatterned base layer of SU-8 may reduce or eliminate delamination of all devices.

We used the fabricated SU-8 masters in a traditional replica molding process with PDMS. We mixed PDMS in the standard 10:1 base : curing agent ratio and degassed the PDMS in a dessicator for ~ 1 hour. We then poured 4-5 grams of PDMS on the master, and slowly rotated the wafer until it was covered roughly uniformly by the PDMS. *We then degassed the PDMS while on the wafer for 2 hours.* This second degassing was crucial to remove microbubbles which formed around the small, dense post and anti-pachinko structures. Removal of microbubbles in the PDMS bulk also enhanced imaging quality at high-magnification and improved optical material homogeneity for the focused laser beam. We cured the PDMS at 65° C for 2 hours and carefully removed the PDMS devices.

Since initial experiments used an inverted microscopy system, we interfaced tubing with the top side of the device. We drilled through glass slides and joined the drilled holes to microtubing with epoxy. We allowed the tubing-slide-epoxy structure to cure in the curing oven for ~ 4 hours at 65° C. The general packaging scheme is illustrated in Figure 2-20.

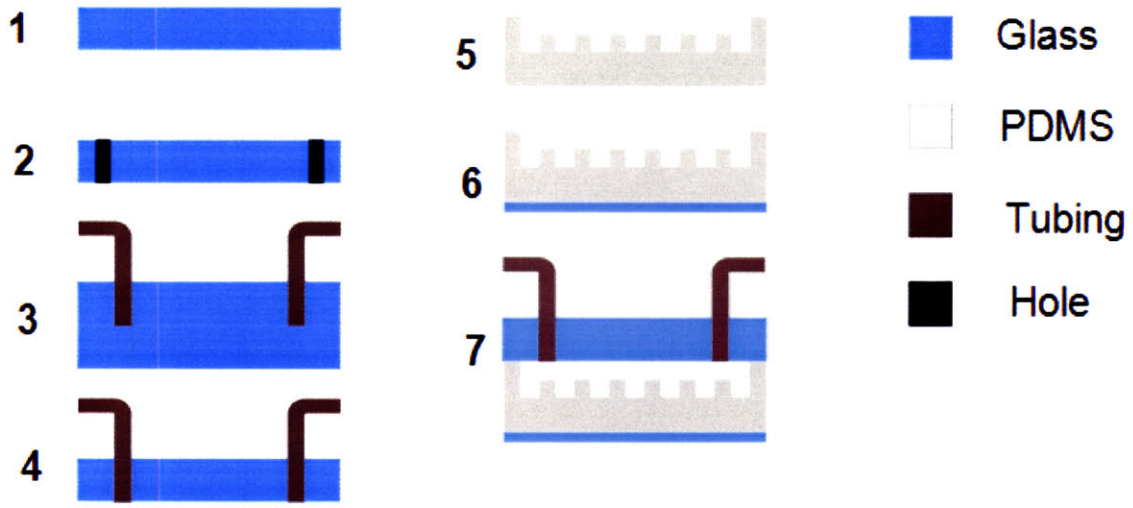

Figure 2-20: Packaging scheme. 1) Glass slide. 2) Diamond drill bit used to drill holes in slide. 3) Helper slide placed under drilled slide; tubing mounted through drilled slide and joined using epoxy. 4) Helper slide removed. 5) PDMS poured, degassed, cured, removed. 6) PDMS bonded to helper coverslip to add mechanical rigidity. 7) Complete bonded structure.

In later experiments, the use of a thin (~1mm thick) PDMS layer demonstrated enhanced optical manipulation performance. However, the thin PDMS layer was mechanically flimsy. Upon bonding to a glass slide, the flow channel would collapse and bond to the slide. Therefore, in order to yield more structural rigidity to the channel, we first plasma-bonded the unpatterned side of the PDMS to a glass coverslip. We then plasma-bonded the coverslip-PDMS structure to the glass slide.

We also measured device features as fabricated. We used images from experiments utilizing the final bonded chamber which included pictures of each well size to determine as-fabricated well diameters. We first mapped pixels to distances using a calibration target of known feature size. Crisp imaging of exact well edges is somewhat difficult, owing to reflection of light within the well. Imaging of well edges is especially difficult in the smaller (< 40-μm-diameter wells). We attempted to reduce the effects of light scattering at the well edges from influencing our measurements by measuring diameters of 4 wells of each diameter at different areas in the image field and averaging the well diameters.

Additionally, we found that wells in fluid-filled devices gave sharper edges for images, which is why we used images from experiments rather than dry, unused devices. We used a 20-μm-inter-well spacing device for the measurements below. Table 2-7 summarizes the differences between as-fabricated dimensions and design dimensions. On average, as-fabricated diameters were 4.3 μm larger than design dimensions, most likely due to the fact that we were forced to use a large hold-off during photolithography. **Whenever we identify wells in experimental images, we refer to the design diameter.**

Table 2-7: Comparison between well design diameters and fabricated diameters. Measurements are for a 20-μm-inter-well spacing device.

Well Design Diameter (μm)	As-Fabricated Diameter (μm)
20	23.1
25	29.6
30	34.6
35	40.2
40	43.9
50	54.4
60	65.5
70	75.1
80	84.9
90	94.0
100	104.4
110	112.6
120	123.3
130	131.9
140	144.7
150	156.7
160	164.4
170	173.8

We estimated chamber and well thickness by measuring the thickness of the fabricated SU-8 gaskets and posts using a 20x-magnification, white light interferometric objective (403910, Nikon). It is unlikely that the measurement technique would allow us to resolve the small difference between PDMS feature depths and SU-8 feature heights, as our microscope (Axioplan 2MOT, Carl Zeiss) was not vibration-isolated, and the objective magnification was only 20x. Measuring feature heights was simpler than measuring depths in packaged devices. We made thickness measurements for our final, best-fabricated wafer, which showed no signs of delamination. We used this wafer for our assays in §3.4. We measured three devices: two close

to opposite edges of the wafer, and one in the center of the wafer, in order to asses variations over the wafer globally as well as locally. We made 3 measurements near 20-μm-, 90-um-, and 170-μm-diameter post regions on both sides of the well array on each device, for a total of 6 measurements per device. Measurements at these points allowed assessment of fabrication variations within a single device. The devices labeled as ("Right Side") were the actual devices used in the assays in §3.4. Figure 2-21 shows the packaged device.

Table 2-8: Variation in SU-8 thickness

Device (Well Spacing [μm])	Gasket Mean Thickness [μm]	Gasket Min. and Max. Thickness (Range) [μm]	Mean Post Height [μm]	Post Min. and Max. Thickness (Range) [μm]
Right Side (20)	91.0	89-93 (4)	46.3	40-51 (11)
Center (10)	85.6	82-90 (8)	44.3	39-49 (10)
Left Side (80)	90.6	84-95 (11)	47.8	45-51 (6)
Total Spread	89.1	82-95 (13)	46.2	39-51 (12)

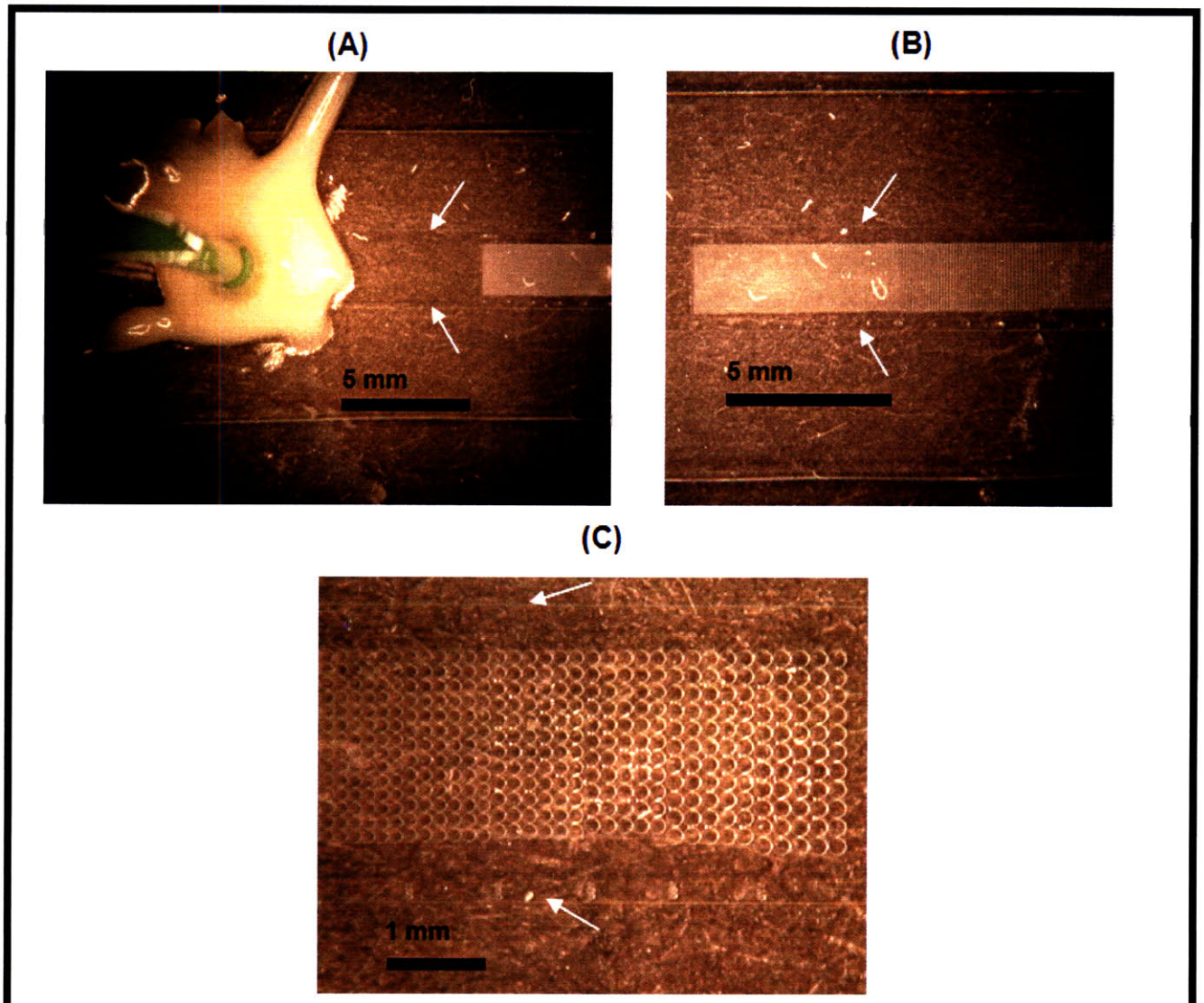

Figure 2-21: Pictures of packaged device. Arrows highlight edges of flow chamber gasket. A) View of device showing inlet tubing, flow chamber, and small-well section of well array field. B) Detail of small-well array section; increase in well diameter is visible from left to right. C) Detail of large-well array section; increase in well diameter is visible from left to right.

Chapter 3 – Results

3.1 Device Preparation Protocol

We interfaced a fluidic network with the packaged device as shown in Figure 3-1. We autoclaved all fluidic network components before operation. We did not autoclave the device to avoid the risk of weakening the epoxy joining the tubing to the drilled glass. We used the configuration illustrated in Figure 3-1 for all experiments.

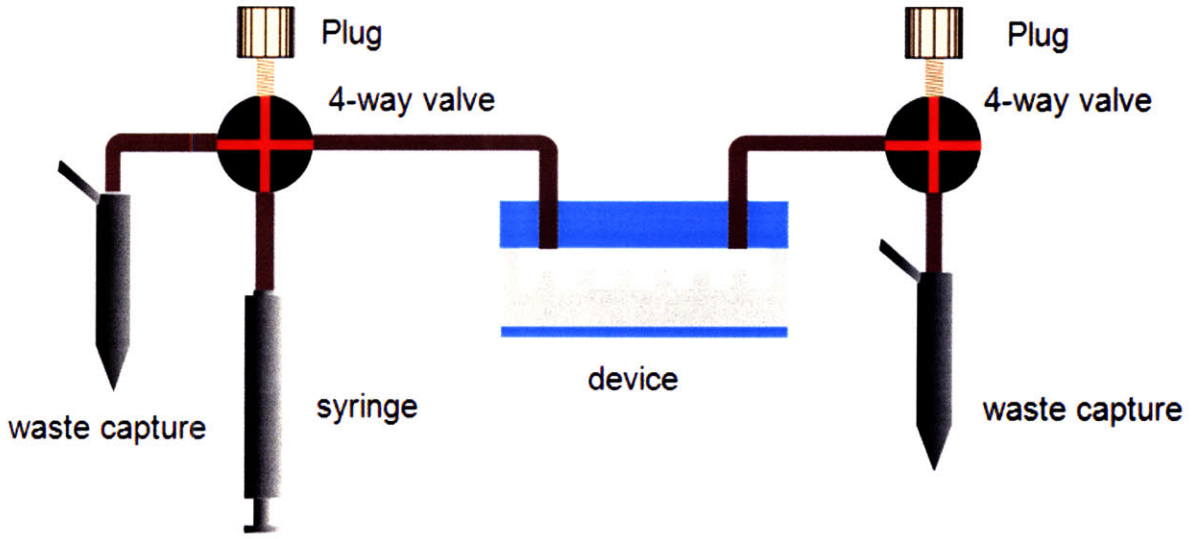

Figure 3-1: Layout of microfluidic network and interface (unions & luers not drawn). We exchanged syringes of various fluids after switching the 4-way valve syringe path to waste capture and subsequently purged the line of any bubbles. Use of two 4-way valves allowed easy stopping of flow after seeding and easy device transport. All fluidic parts except for syringes were from Upchurch Scientific: 4-way valve (V-101D); 1/16'' OD / 0.03'' ID PEEK tubing (1533); 1/16'' OD fittings: ferrule (P-200); PEEK nut (P-235); union (P-702); plug (P-316); syringe luer (P-628). Syringes: 10 ml, glass (Hamilton 81620) or 3 mL, plastic (309603 BD Biosciences).

We prepared the device using a protocol adapted from Table 2-5 and summarized in Table 3-1. The protocol is user-friendly, straightforward, robust, and time-effective. If devices are cured the night before the experiment and fluidic components are autoclaved beforehand, the process takes only 1.5 hours of preparation time before the assay.

The protocol includes a step for well-wetting. The hydrophobic PDMS wells do not automatically wet; pressure must be applied inside the chamber to drive air out of the wells through the gas-permeable PDMS. We accomplished this by stopping the output of the 4-way valve by switching the valve to the plugged state. We then applied pressure to the chamber using a hand-operated syringe connected to the input 4-way valve. We applied constant pressure by hand just strong enough to cause the wells to begin to wet. We allowed all wells across the field

to wet; the process took about 5-10 minutes. If wells ceased to wet at any point, we increased pressure just enough to continue wetting.

Table 3-1: Device preparation protocol subsequent to chamber bonding.

Step	Description	Time/Temp. (C)
1.PDMS hydrophobicity treatment	Reverse PDMS surface to hydrophobic; place entire device in PDMS curing oven. ***critical***	12 hrs./65° C
2. Autoclave Fluidics	Autoclave support fluidics.	See autoclave
3. Assembly	Assemble device & fluidic network in tissue culture (TC) hood	
4. PBS Rinse	Fill syringe w/ PBS; inject through device; pre-absorbs small amount of PBS into PDMS; perform in TC hood.	3 min / RT
5. Ethanol Rinse	Fill syringe w/ 80% ethanol; inject through device; sterilizes flow chamber; perform in TC hood.	1 min / RT
6. PBS Flush	Fill syringe w/ PBS; inject PBS into device and flush all ethanol from chamber and fluidic network; perform in TC hood.	1 min / RT
7. Protein treatment	Fill syringe w/ protein suspension for surface treatment: use 5μg/mL fibronectin (33010-018, Invitrogen) in PBS for adherent cell lines or 7.5% BSA (stock solution 15260-037, Invitrogen) for non-adherent cell lines. Inject protein suspension into chamber; perform in TC hood.	1 min / RT
8. Well wetting	With protein treatment syringe attached and protein suspension in chamber, switch device output path to shut. Move device onto microscope stage and gently apply pressure; output should be stopped – no additional liquid should flow through device. Continue to apply pressure until air is purged from all wells. When all wells are wetted, switch input valve device path to stopped, trapping protein suspension in the chamber.	15 min / RT
9. Protein adsorption	Place entire assembly into device incubator, allowing suspension in chamber to adsorb to chamber surfaces. Alternatively, perfuse protein suspension through device for duration using syringe pump. We used the latter method for fibronectin adsorption at a flow rate of 1 ml/h to ensure fluid protein concentration would not degrade. We did not use perfusion for BSA adsorption.	1 h / 37° C
10. Cell injection	Move assembly into TC hood; switch syringe w/ cell suspension; inject cells into chamber. Move device onto microscope stage and continue injecting cells as desired. Wait 10-15 minutes to allow cells to partially stick inside wells. When ready to purge cells from inter-well regions, move assembly back into TC hood & switch syringe w/ plain media syringe. Move device back onto scope and gently purge cells outside wells. Perform short-term assay or place in incubator for long-term assays, with perfusion or static culture if desired.	

It is *critical* to cure the device in the PDMS oven following plasma bonding to allow the PDMS surface to regain hydrophobicity for protein adsorption for the reasons explained in §2.3. We observed that if the device was placed in the curing oven for 12 hours after bonding, the wells would not wet after we injected PBS into the device, suggesting that the PDMS had reverted to being hydrophobic. We then needed to wet the wells via the above protocol.

In contrast, in the case of one non-adherent cell experiment, we used a device which had been bonded *three days before use*, but not subsequently cured in the oven. Upon injecting our BSA suspension into the device for surface treatment, all wells wetted nearly instantly, suggesting that the PDMS was still hydrophilic, even three days after bonding. When we tried to use the device which had not been placed in the curing oven after bonding, we were unable to optically levitate cells from wells, possibly because BSA had inadequately adsorbed to the wells.

There is no UV sterilization step; the glass and PDMS of the device are impenetrable at the UV wavelengths in the tissue culture hood.

3.2 Adherent Cell Operation

We first investigated adherent cell culture within the microwell arrays. We cultured NIH 3T3 fibroblasts in serum-containing media (87%/vol. DMEM (11960-044, Gibco); 10%/vol. BCS, HyClone; 1%/vol. Penicillin-Streptomycin, (15140-122, Gibco); 2%/vol. l-glutamine (25030-081, Gibco)). Incubation conditions were 37.0° C, 7.5% CO_2 atmosphere. We fed cells every other day and passaged at 80% confluence.

We prepared for adherent cell operation as described in §3.1. We seeded the device with 3T3 fibroblasts and incubated the device for ~16 hours using the same media and incubation conditions as above. We first used wells with inter-well spacing of 20 μm; some of these wells were partially fused due to the non-idealities introduced by the photolithography compromises described in §2.7. Figure 3-2 illustrates the results 16 hours after seeding.

After recording the images in Figure 3-2, we injected 10x trypsin EDTA (15400-054, Invitrogen) into the chamber. Under slow perfusion of trypsin, we observed loosening of cell attachment to the PDMS substrate within 1-2 minutes. Immediately after increasing flow, some cells detached completely and began tumbling in their respective wells.

We observed three fundamental behaviors. In wells smaller than 50 μm in diameter, cells exhibited little if any detachment. In wells with diameters between ~ 50 μm and 80 μm, a significant fraction of cells detached and oscillated back and forth in their wells during flow. Under flow conditions strong enough to induce these oscillations, cells residing in wells greater than 80 μm in diameter were generally ejected from their wells.

We attempted to optically levitate cells after trypsinization by using the setup described in §2.4.1. We optically released a few cells, but success was sporadic and rare. Cells exhibited a wide range of adhesion strengths: across an array of fixed well size, flow conditions adequate to detach cells and induce oscillatory behavior in some wells were sufficient to eject cells from other wells, while cells in some other wells did not detach at all. Partially detached cells would often optically levitate, but small remaining adhesion tethers would hold the cell to the PDMS.

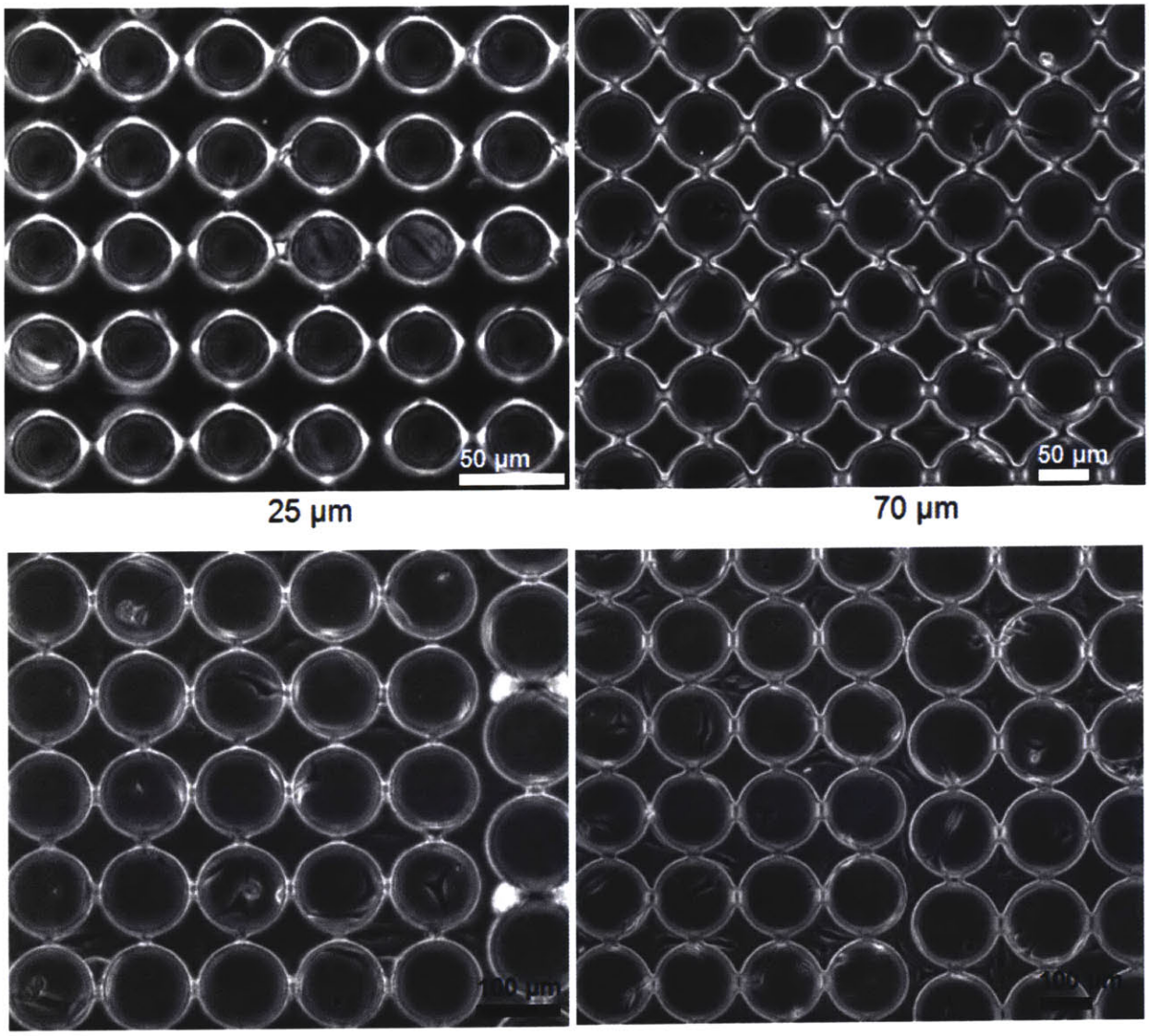

Figure 3-2: Results of culture of 3T3 fibroblasts for 16 hours in fibronectin-coated PDMS wells of indicated diameters. In 25-µm-diameter wells, viable adhered cells tended to spread on well walls. In 70-µm-, 100-µm-, and 110-µm-diameter wells, cells exhibited more spreading in bottoms of wells of increasing size, with some cells still spreading on well walls. The 140-µm- and 150-µm-diamter cases illustrate the preference with which cells will seek the flat, inter-well regions over well floors.

After repeating the experiment using devices with larger inter-well spacing, we observed complications due to cell adhesion between wells and to the entry area of the chamber. Upon trypsinization, these cells released and far outnumbered the small number of cells in the wells, making it difficult to determine whether a detached cell in a well had been cultured in the well or had settled in the well after trypsinization. Figure 3-3 illustrates this finding.

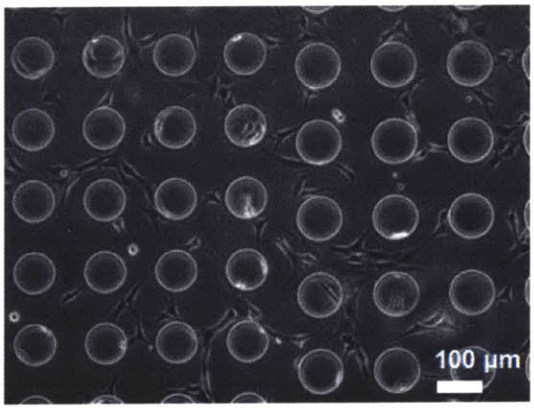

Figure 3-3: Cell adhesion and growth in inter-well regions for devices with larger inter-well spacing. All devices suffer from similar problems in the channel entry areas, regardless of inter-well spacing.

Previously, we had seeded cells and allowed them to settle for ~10-15 minutes before purging cells from inter-well regions. It was difficult to purge cells from inter-well and channel entry regions due to fast binding of cells to the fibronectin-coated surface. We attempted to solve this problem by applying a differential surface treatment to the inter-well regions and entry regions versus the well walls and floors [32]. We aimed to coat the inter-well and entry regions in BSA, blocking these areas from fibronectin adsorption, and decreasing the quick adhesion of cells to these areas. We then aimed to adsorb fibronectin to the well walls and floors.

We followed the device preparation described in Table 3-1 up to the well wetting step. In the wetting step, we opened the output of the device and slowly injected BSA, stopping both ends of the device after BSA had filled the chamber. We then incubated the device for ~ 30 minutes. We switched the syringe with fibronectin solution, stopped the output port, and injected the device with fibronectin at high pressure, wetting the inside of the wells with fibronectin solution. We then incubated the device for ~ 30 minutes before seeding cells. Figure 3-4 illustrates the method.

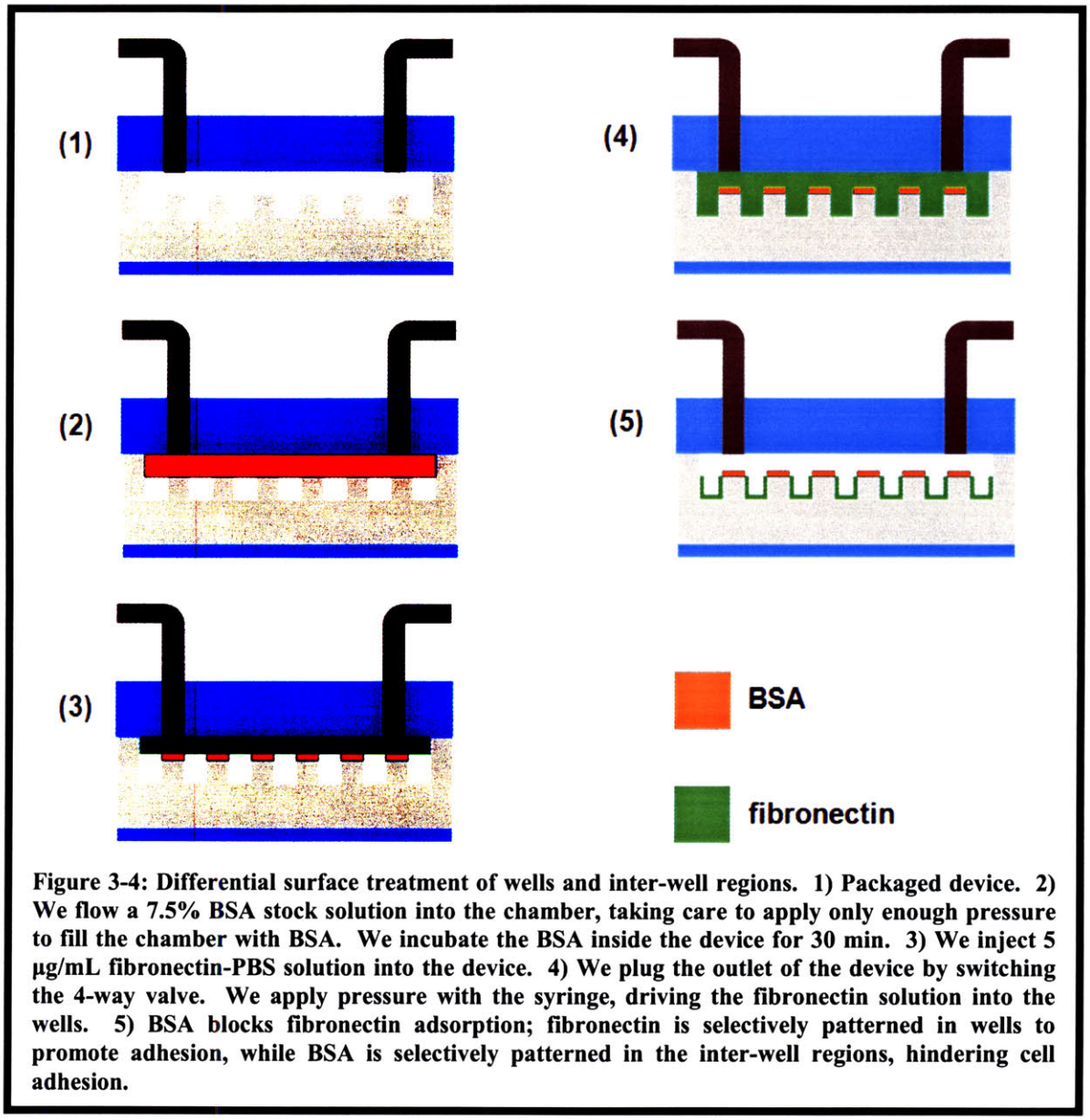

Figure 3-4: Differential surface treatment of wells and inter-well regions. 1) Packaged device. 2) We flow a 7.5% BSA stock solution into the chamber, taking care to apply only enough pressure to fill the chamber with BSA. We incubate the BSA inside the device for 30 min. 3) We inject 5 µg/mL fibronectin-PBS solution into the device. 4) We plug the outlet of the device by switching the 4-way valve. We apply pressure with the syringe, driving the fibronectin solution into the wells. 5) BSA blocks fibronectin adsorption; fibronectin is selectively patterned in wells to promote adhesion, while BSA is selectively patterned in the inter-well regions, hindering cell adhesion.

After seeding, we easily purged cells from the entry areas and inter-well regions before incubation. The next day, few cells resided outside wells, as shown in Figure 3-5, which was taken ~16 hours after seeding. However, cell morphology was markedly different from morphology of cells grown in traditional culture dishes. It is possible that morphology appeared different because the cells exhibited strong preference to remain in the wells, causing them to spread on the sides of the wells and making imaging difficult; Ostuni *et al.* observed similar behavior in analogous experiments [32]. It is important to note that the morphology in a well might not be any less optimal than that observed in a dish; the morphology shown in a well could simply be the natural cell response to spreading on a non-planar surface.

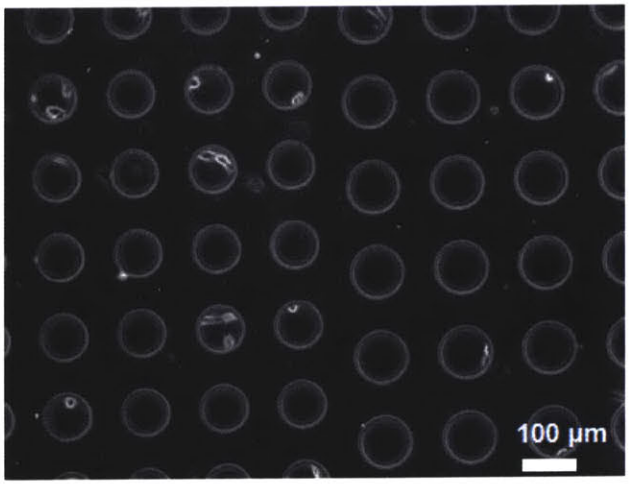

Figure 3-5: Results of differential fibronectin / BSA surface treatment on cell culture. Number of cells residing outside wells is drastically reduced relative to Figure 3-3. However, cell proliferation within wells is not widespread. The method holds promise, but needs refinement.

It is possible, however, that the morphology might also be attributable to media conditions: we incubated cells in a closed, static microfluidic chamber with a swept volume of 15 µL overnight. A creeping perfusion culture might be better for cell health. Nikhil Mittal, a fellow lab member, has successfully cultured HeLa cells in these well arrays which showed healthy morphology and proliferation. He used the well array in a small culture dish, providing a much larger source of nutrients. However, Figure 3-3 showed that cells spreading between wells exhibited morphology similar to that in a traditional culture dish, suggesting that the chamber volume contains enough nutrients for the time course of the experiment.

In our experiments with 3T3 fibroblasts, only cells in very large wells (> 140 µm in diameter) exhibited morphologies highly similar to those in culture dishes. While the morphology observed in a dish might not technically be any more "optimal" than that in a well, cells are much easier to image when spread on a planar surface. This result might suggest that an adherent cell architecture should utilize larger wells, necessitating deeper wells for adequate hydrodynamic shielding.

In a second attempt, we purged cells from inter-well regions in devices treated completely with fibronectin as easily as cells seeded in devices with the differential surface treatment. This result suggests that the differential surface treatment technique was inconsistent and needs refinement. Quantifying protein localization by using fluorescently labeled BSA and

fibronectin would be a good step to ensure that the protocol allowed consistent, patterned adsorption [32].

We also tested the pachinko architecture. We found loading to be finicky and cumbersome, as cells tended to be diverted around the structures. Brian Taff, a fellow lab member, stated that his success with the architecture had required extremely low flow rates and longer load times. We concluded that well loading was simpler, and abandoned the pachinko design in its current form. Patterning a small channel along the center of the shape might permit cells to flow towards the structure by allowing fluid streamlines to pass through the structure. It is unlikely that these structures will afford the hydrodynamic shielding robustness of the well arrays.

We decided that the architecture as fabricated was sub-optimal for adherent cells. Use of larger, deeper wells, or other designs entirely could be a better solution for adherent cells. We shifted effort to evaluating performance with non-adherent cell lines.

3.3 Non-Adherent Cell Operation

We validated functionality with non-adherent cells. We cultured HL-60 cells in serum-containing media (77%/vol. RPMI (21870-076, Gibco); 20%/vol. BCS, HyClone; 1%/vol. Penicillin-Streptomycin, (15140-122, Gibco); 2%/vol. l-glutamine (25030-081, Gibco)). Incubation conditions were 37.0° C, 7.5% CO_2 atmosphere. We refreshed media every third day and passaged at 90% confluence. We prepared a setup for non-adherent cell operation as described in §3.1. We seeded HL-60 cells, allowed them to settle, and purged cells outside wells with fresh culture media. We then closed both ends of the flow chamber and moved the device to the optical setup described in §2.4.1.

We successfully levitated numerous cells from wells and purged them using flow. We operated syringes by hand to purge cells in order to facilitate control and focus attention to the image output and laser control in these initial experiments where attention was critical. As a result, we don not have explicit flow rates used to purge cells. However, purged cells traveled at speeds easily exceeding 200 μm/s while untargeted cells remained in their wells, demonstrating the hydrodynamic shielding the wells afforded.

We started by operating the laser at ~ 100 mW sample power and levitated cells from wells ~ 50 μm in diameter. All wells were ~ 50 μm deep. Cells levitated from wells in ~ 2 seconds. We compared images of cells in our device with a calibration target to estimate the cell radius to be 5.5 μm. Considering the net gravitational force, the implied optical force was about 3.5 pN using a Stokes drag calculation uncorrected for wall effects. The power / force ratio was approximately 28 mW/pN.

We found that cells sluggishly separated from the substrate, but moved faster after leaving the surface. We noticed a slowing in levitation from wells smaller than 30 μm in diameter, though we successfully levitated cells from wells as small as 25 μm in diameter in under 4 seconds. The increased difficulty is partially due to increased Stokes drag as the particle approached well walls. Additionally, cells were levitated along a slightly off-vertical path, dragging cells along well walls.

The beam might have possibly been aligned slightly off-vertical, as aligning the beam to be perfectly perpendicular to the optical table is difficult without incorporating more elaborately adjustable mounts for M4 and OBJ in Figure 2-5. We failed to levitate cells from 20-μm-diameter wells, where off-vertical levitation effects became insurmountable. Careful realignment of the beam might resolve the issue. Figure 3-6 illustrates typical results.

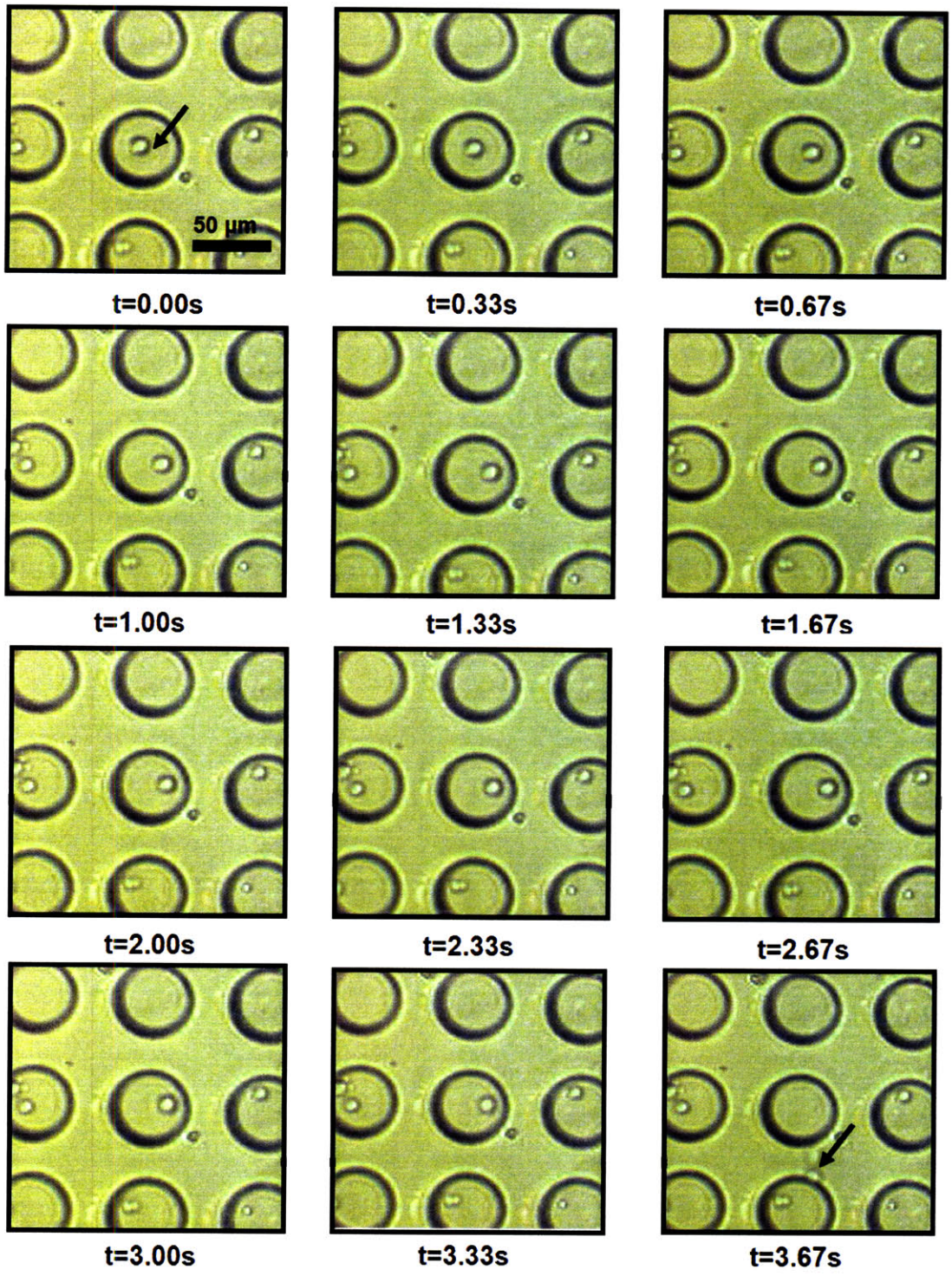

Figure 3-6: Levitation and purging of a target cell (HL-60). After levitation, we gently squeezed / tapped the plunger of the injection syringe by hand, briefly inducing flow, and purging the cell from above the well. The cell moved downstream as shown at *t=3.67s*, and as highlighted by the arrow. Flow direction is from top to bottom in the pictures. Focus characteristic of cell changes little during levitation due to use of low-quality, low-magnification objective and low-quality CCD.

The levitation forces were highly localized. On multiple occasions, we levitated a single cell from a well containing more than one cell, as shown in Figure 3-7. Since passively loaded well arrays typically have sites with multiple cells, this feature is potentially useful. If the laser manipulation system were integrated into the microscope used for inspection, isolation of target cells in multiple occupancy wells would be enabled.

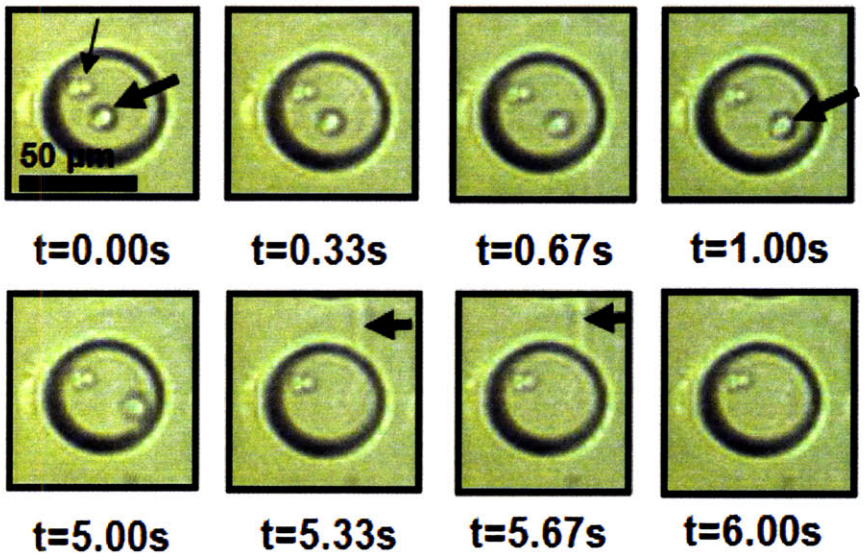

Figure 3-7: Demonstration of localization of applied force. Although two cells (indicated by the two arrows in the *t=0.00s* frame) were residing in a single well, we selectively levitated a single cell from the well (indicated by the larger arrow). During the first second, we levitated the cell. We then purged the cell by gently squeezing / tapping the syringe plunger by hand at *t=5.00s*; the delay between levitation and purging was due to delay in handling the syringe. The cell appears as a blur at *t=5.33s* and *t=5.67s*. In contrast to Figure 3-6, the flow direction is from bottom to top.

3.4 Assays

3.4.1 *Fluorescence Color-Based Cell Sorting*

We next sorted cells based on fluorescence color. We stained approximately equally sized HL-60 cell populations in separate confluent 150 mm dishes using CellTracker Green CMFDA and CellTracker Orange CMRA (Molecular Probes) using standard protocols from datasheets. We performed staining exactly following the protocol outlined in the datasheet, but skipped the optional steps of 3.3, 3.5, and 3.7 in the datasheet. Our staining working solutions contained 5 μM concentrations of dye.

We prepared a setup for non-adherent operation as described in §3.1. We pipetted the contents of the two dishes containing the separate populations into centrifuge tubes and spun down cells using 1000 rpm for 7 min. All steps requiring spin-downs of HL-60s used these

settings. We re-suspended the cells of both centrifuge tubes into a single tube containing culture media to create a 5 mL cell suspension of 1:1 green : orange mixture of the two populations.

We injected the mixture into the device. We allowed the cells to settle and switched the injection syringe from cell suspension to PBS to lower background fluorescence relative to media. We purged cells outside wells with PBS and stopped both ends of the chamber.

Using an inverted fluorescence microscope (Axiovert, Carl Zeiss) outfitted with a camera (Spot RT Color, Diagnostic Instruments), we recorded fluorescence images of the cell array using a FITC filter cube (41001, Chroma) for green-labeled cells and a Cy3 filter cube (61000v2, Chroma) for orange-labeled cells. We noted locations of a few wells containing single green-labeled cells. We used a well at the lateral edge of the array at the transition between the 20-μm-diameter and 25-μm-diameter wells as a reference well, and noted well locations relative to the reference well. After calibrating pixel sizes, we measured the as-fabricated well sizes used for the experiment as 31.0 μm in diameter. The same size of well was also used for the sort illustrated in §3.4.2.

After moving the device to the optical setup described in §2.4.1, we located the noted well locations by counting from the known reference well. We then used the laser to levitate the target cells from the wells and purged the cells from the device. We then transferred the device back to the fluorescence microscope and recorded images of the array after sorting. Figure 3-8 illustrates the results.

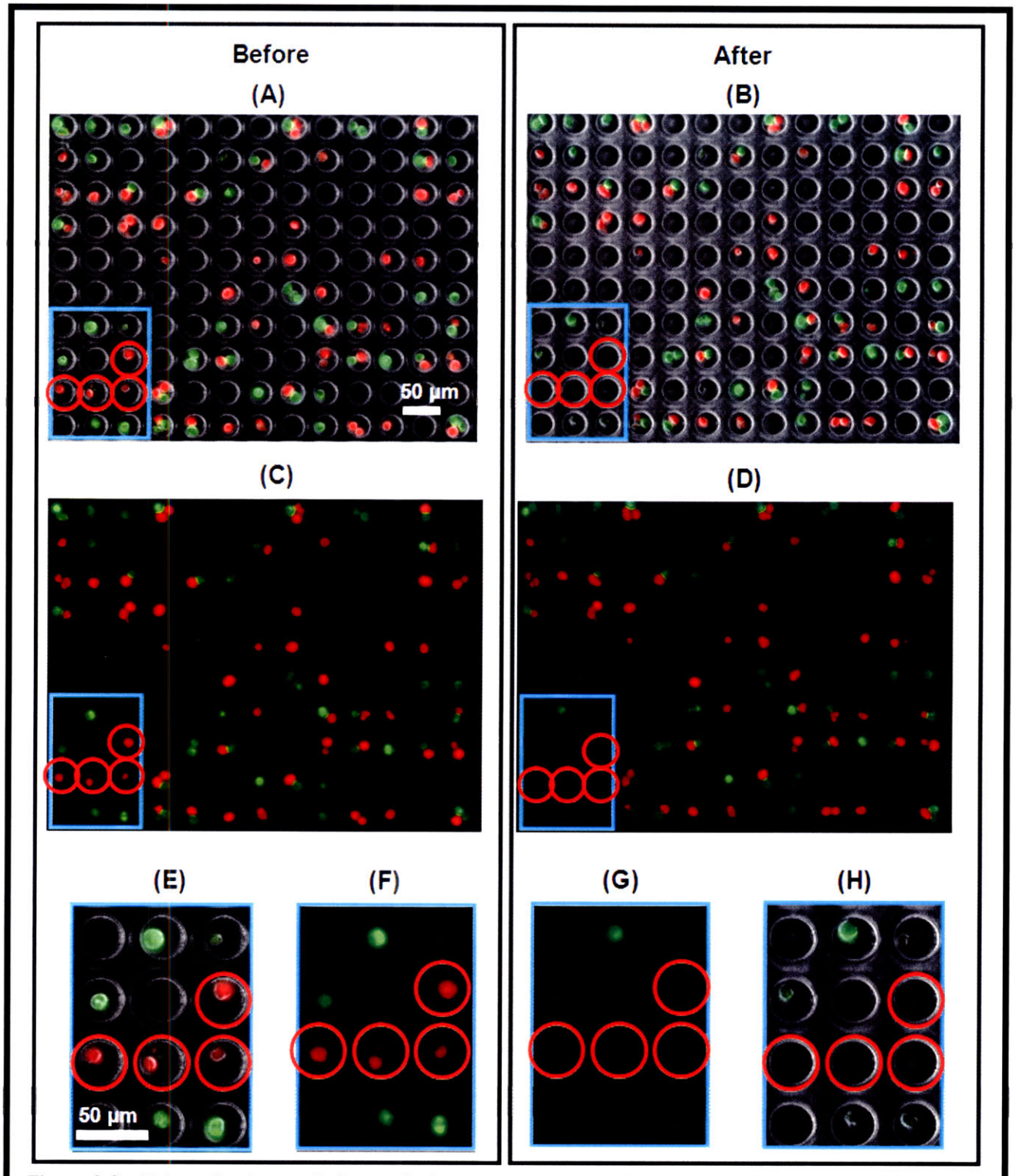

Figure 3-8: False-color images before and after green- vs. orange-labeled cell sorting; all images A-D are single, unstitched 20x–magnification images; E-H illustrate detail from the boxed portion of the array. A,B,E,H) Combined phase & fluorescence images; C,D,F,G) Combined fluorescence images. Note in (A-D) that unsorted sites contain same cells before and after sorting; method is robust to accidental removal of untargeted cells. Some photobleaching of cells close to target cells occurred due to accidental laser misalignment during assay. Target cell locations are circled.

We used a sample illumination power of ≤ 150 mW. The orange-green sort required a few illumination attempts remove the first cell due to slight laser misalignment. This misalignment is responsible for partial photobleaching of neighboring cells as shown in G) and H) in Figure 3-8. Careful initial alignment avoids the problem. We illuminated each target cell for 4-5 seconds before being purged to ensure complete levitation from the well. Shorter times may have been sufficient, but we were conservative in this trial.

All untargeted cells shown in A-D) remained in their wells after sorting, highlighting the robustness of the method. Array loading efficiency was far lower than is possible. Proper sizing of wells has been shown to allow single-cell loading efficiencies of 80% [19]. Wells were ~ 50-μm-deep and considerably larger than the cells, which is clearly not an optimal size. Wells should be redesigned to be marginally larger than the cells they capture; this change is trivial.

3.4.2 Fluorescence Localization-Based Cell Sorting

We demonstrated true image-based sorting by performing a sort based on fluorescence localization, a sort unavailable with FACS. We stained a population of HL-60 cells with Hoechst, (33258, Molecular Probes) a nuclear stain. We added Hoechst directly to the cell culture media to achieve a final dye concentration of 5 μg/mL. After adding dye, we incubated the cells in the dye-containing-media for 15 min. at 37° C. We then washed the cells in PBS to remove the Hoechst and re-suspended half the cells in a dish containing culture media, and the other half in a dish containing PBS.

Next, we additionally stained cells in the PBS-containing dish with Concanavalin A (ConA, Alexa Fluor 488 conjugate, C11252, Invitrogen), which preferentially stained proteins in the cell membrane. We added ConA to achieve a concentration of 50 μg/mL and incubated the ConA-containing dish for 20 min. at 37° C. We washed the ConA-stained cells with PBS twice. We then spun down the contents of the Hoechst-only-stained dish as well as the Hoechst+ConA-stained dish and re-suspended the contents of both dishes in a tube containing 5 mL PBS, creating a mixture of Hoechst-only- and Hoechst+ConA-stained cells.

There were significantly more double-stained cells in the mixture because many double-stained cells stuck to their culture dish while being removed for one of the spin-down procedures. This loss of cells was unintentional, and fewer than expected cells were utilized from the dish. The loss was not problematic, however, as we could now demonstrate selection of "rare" cells. We prepared a device for non-adherent cell operation as described in §3.1. We loaded the cell mixture into the device using a protocol identical to that in §3.4.1.

We aimed to remove cells exhibiting membrane-localized fluorescence. We used an inverted fluorescence microscope to locate cells of interest and moved the device to the optical setup to remove the target cells. We then moved the device back to the fluorescence microscope to record images following sorting. Figure 3-9 and Figure 3-10 illustrate the results.

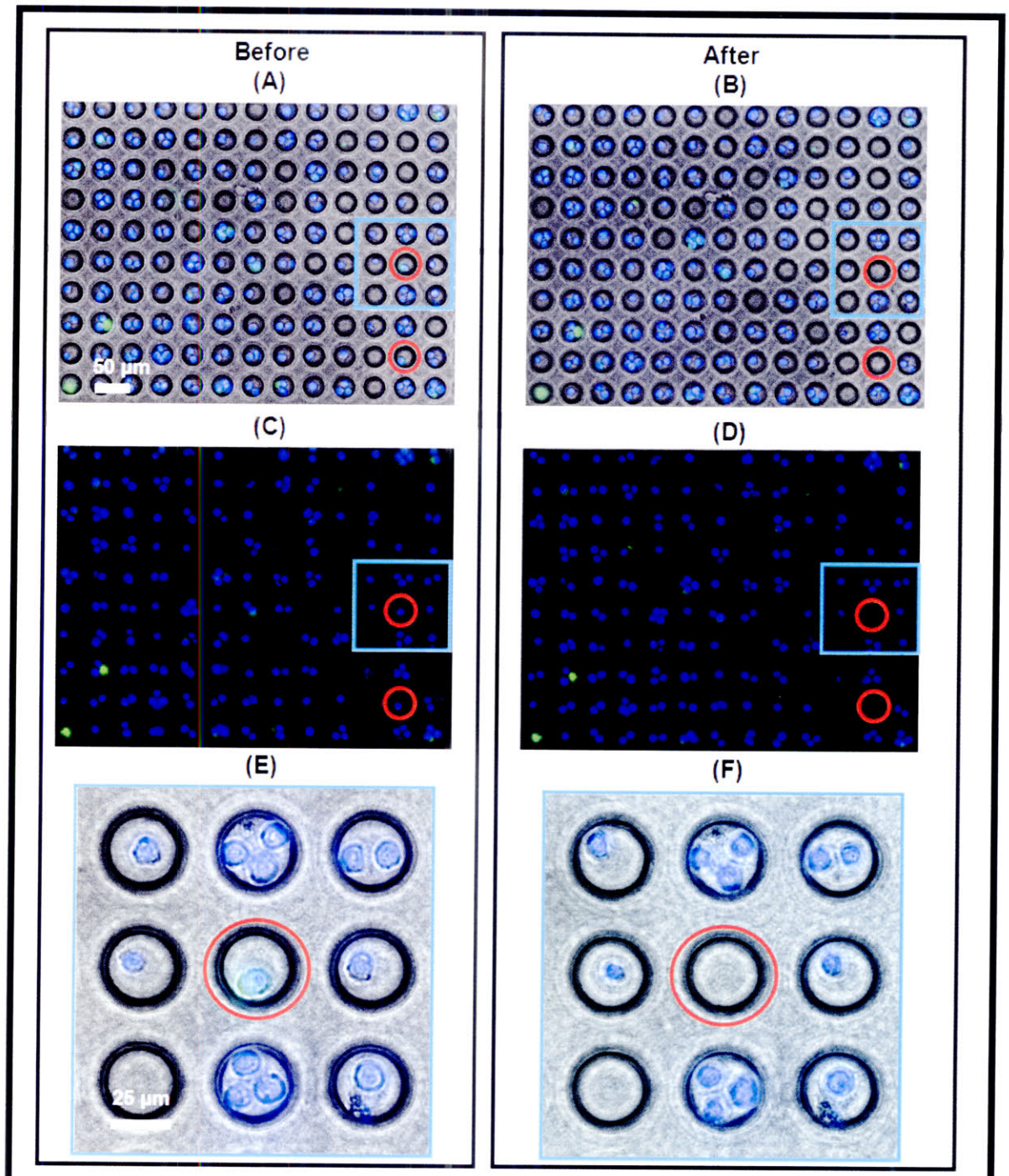

Figure 3-9: False-color images of the array before and after image-based cell sorting. A-D) are single, unstitched 20x-maginifcation images; E-F) are 63x-magnification images of boxed regions. A,B,E,F) are combined phase & fluorescence images; C,D) are combined fluorescence images. We successfully removed cells in circled locations with membrane-localized stains.

Again, the results illustrate that we could robustly remove only specifically targeted cells. Figure 3-10 highlights the extent to which the new architecture enables inspection of qualitative image features before sorting. We used different colors of stain purely for illustrative purposes.

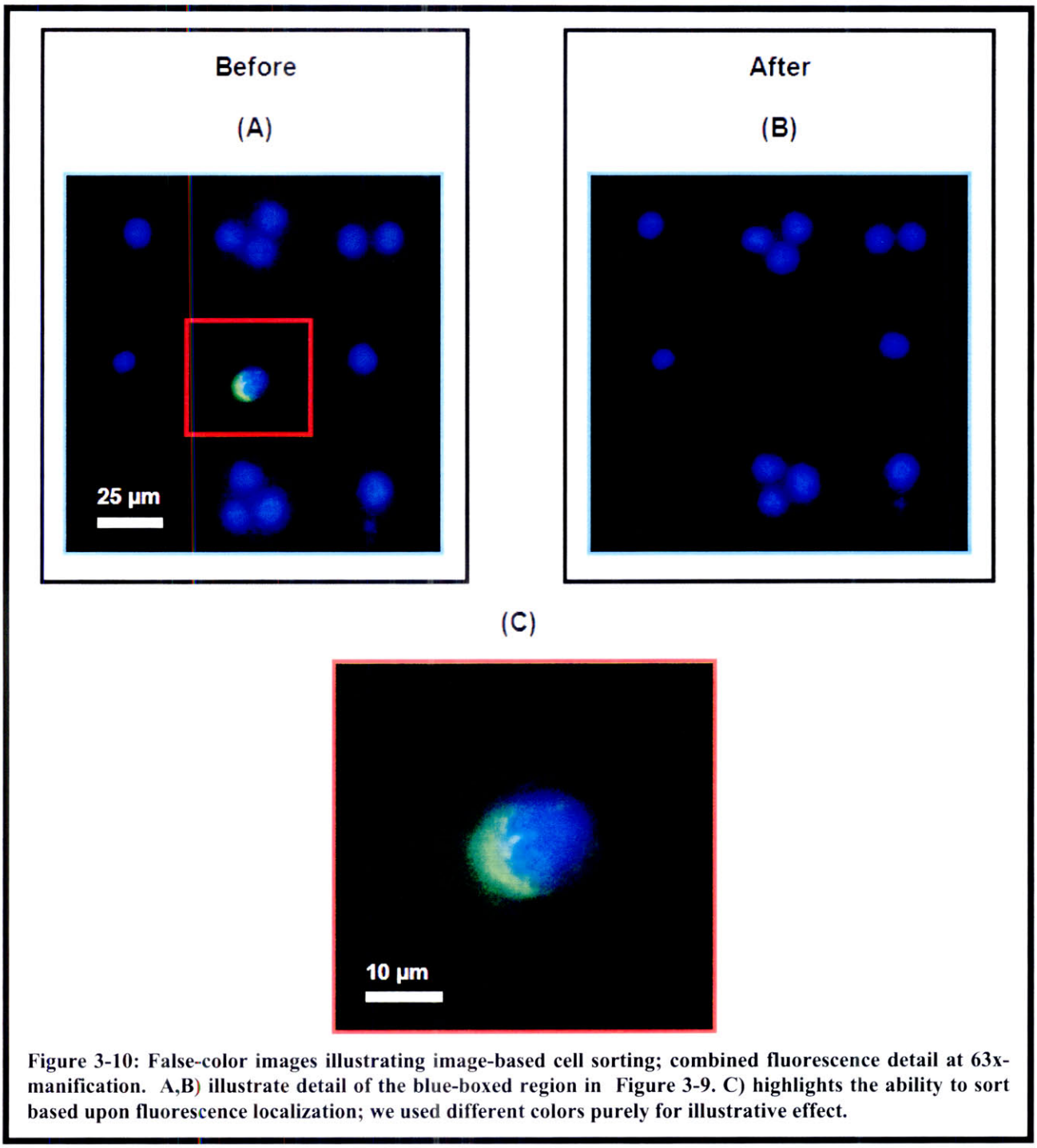

Figure 3-10: False-color images illustrating image-based cell sorting; combined fluorescence detail at 63x-manification. A,B) illustrate detail of the blue-boxed region in Figure 3-9. C) highlights the ability to sort based upon fluorescence localization; we used different colors purely for illustrative effect.

Chapter 4 – Future Directions

4.1 Scaling, Automation, and Interface Concerns

As fabricated, the architecture was incompatible with adherent cells. However, results indicated that the scheme performed well with non-adherent cells. We considered the feasibility of using the architecture to undertake assays with large numbers of cells.

A major advantage of the architecture is its scalability. A 22,000-site array of 20-μm-diameter wells with 20 μm inter-well spacing could fit in the same 2-mm x 18-mm well region used in the test devices. A 5-mm x 32-mm well region would support 100,000 sites, and a million-site array would simply require a 40-mm x 40-mm well region. The former could be implemented using a scaled version of the current architecture. The latter would require some redesign of the flow chamber, but would likely not be difficult to realize. Scaling to such large array sizes would likely take weeks or months rather than years.

Array inspection time is likely to limit array sizes rather than the difficulty of constructing large arrays. For all but the smallest and simplest image-based assays, human inspection of each site is impractical. Incorporation of the architecture into an automated imaging platform capable of image feature recognition would enable a new class of assays.

In one example, the automated system might inspect each site and compile a list of cell images and locations exhibiting desired image features. The user could examine the list, return to the locations, inspect the cells, and manually use the optical levitation force to retrieve the cells of interest. This approach would restrict operation to retrieval of a small number of cells.

Another example is full automation. In this case, array inspection would be computer-controlled, as would be cell retrieval. It would be reasonable to expect that a cell could be automatically retrieved in ~ 10 seconds. Retrieval of 100 cells would take ~ 20 minutes, and retrieval of 1,000 cells would take ~ 3 hours. The latter case would require environmental control of the chamber. The number of levitation beams could be scaled as well; use of five independently positioned levitation beams would reduce the time to remove 1,000 cells to about half an hour.

A future challenge will be capture of small numbers of released cells. Simply collecting fluid output would yield cell concentrations far too small to be practical. We may need to incubate released target cells in separate microfluidic chambers to increase target cell concentrations. Furthermore, capturing target cells exclusively is not trivial; clumps of untargeted cells can accumulate in valves, tubing, and within the flow chamber, such as around the inlets and outlets.

As a result, world-to-chip interfacing will likely need improvement. A possible approach would be to fabricate separate ports for cell-injection, purge-media injection, waste, and target cell capture. This approach would allow the media used to purge target cells to avoid passing through pathways used to inject cells, which would contain significant numbers of unwanted cells. The target cell capture port would remain closed and the waste port open until target cell release, keeping the capture port clear of unwanted cells. This idea is illustrated Figure 4-1.

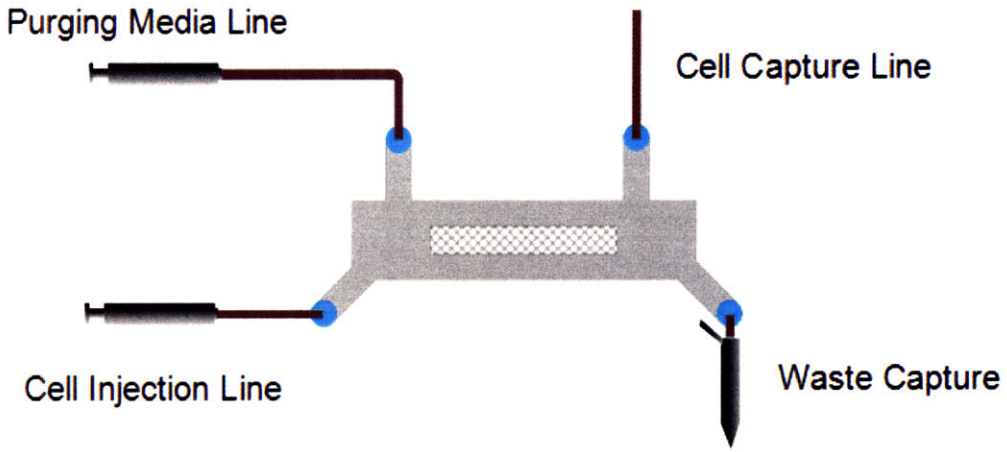

Figure 4-1: Potential change to fluidic interface to improve sample purity by using separate injection and purge paths. The waste capture line is left open and the cell capture line is kept shut until target cell release, at which time the waste capture line is closed and cell capture line is opened, avoiding collection of residual cells already in the waste path.

With improved world-to-chip interfacing, the current architecture will be amenable to scaling, automation, and imminent use in assays. We will likely implement automated cell image interrogation with un-automated cell release within months. Full automation could prove significantly more difficult; its ease of implementation will likely hinge on the ability of the computer vision system to receive reliable information regarding positions of the levitated cells.

4.2 Incorporation Into a Fluorescence Microscope

We present a plan for integration into an automated fluorescence microscope. We aim to incorporate the system into our upright fluorescence microscope (Axioplan 2MOT, Carl Zeiss). We will use a 290 mW, 980nm laser diode (Avanex, 3CN00283AL) to help prevent cell damage.

The challenge of the optical setup is fitting the system between the stage and the microscope base. If we used a layout passing the beam through a beam size adjuster before passing it through a focusing lens, as in Figure 2-5, we would require a beam collimator and expander next to the scope, consuming table space. We decided to pick a combination of collimating lens and focusing lens to yield the target spot size, reducing the entire system to a size that could be fit into the space under the stage, as illustrated in Figure 4-2.

We plan to mount the lenses in cage-mount X-Y translation holders which can be held with traditional post holders. The post holders will interface with a 90° bracket. The bracket will mount onto a stack of translation stages which will create a 3-axis stage. The 3-axis stage will rest on a tip/tilt stage, allowing complete freedom to align the beam to the optical axis of the microscope.

We will mount the tip/tilt stage on a breadboard. We will mount the breadboard on three kinematic ball bearing mounts which will interface with three complementary ball bearing holders. The holders will be permanently fixed to the table using an epoxy removable via razor

blade. The kinematic mounting allows the entire system to be removed when not in use while maintaining alignment to the optical axis when re-mounted in the future.

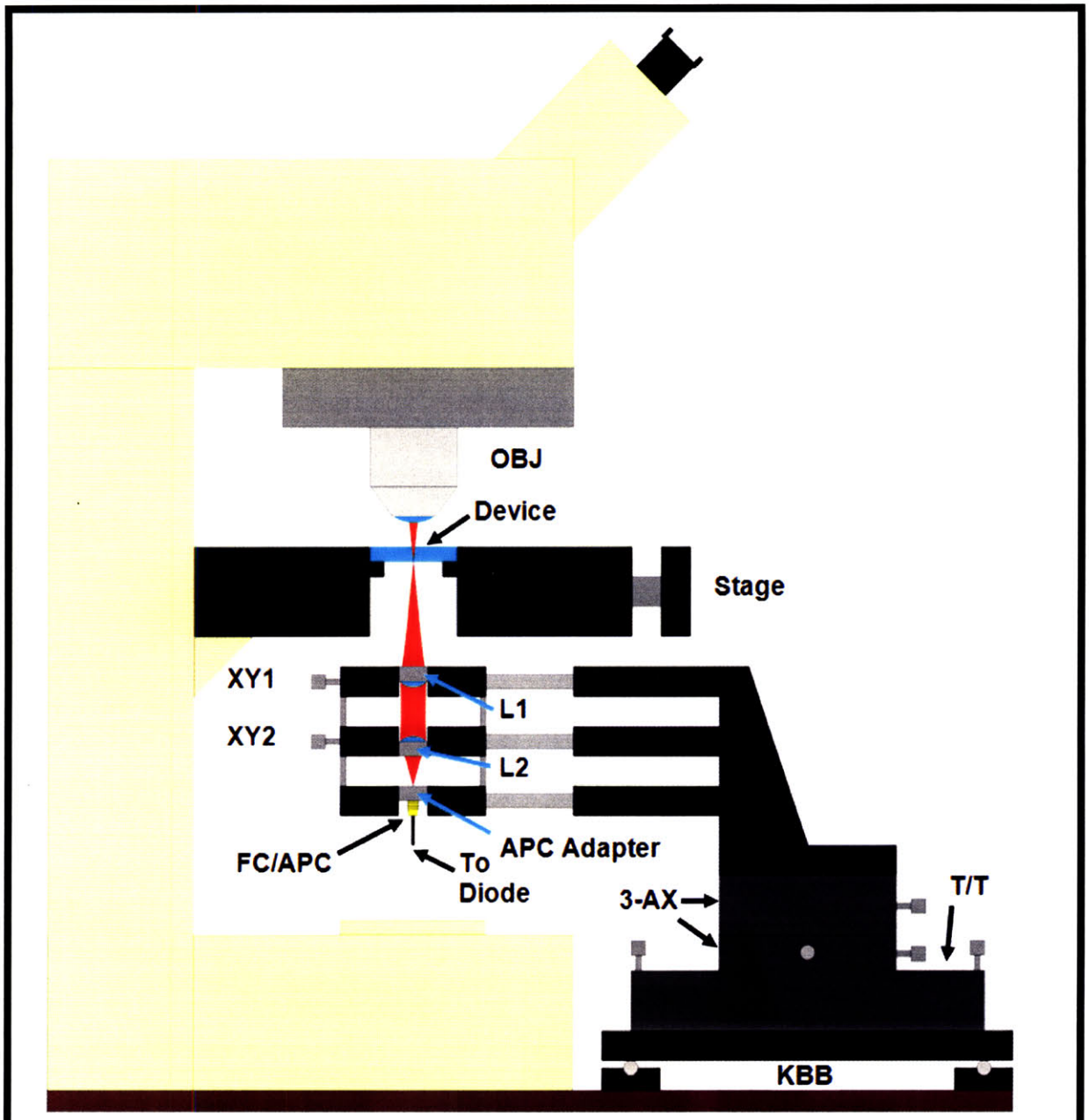

Figure 4-2: Schematic of system incorporation. Two aspheric lenses are used to collimate (L2) and focus (L1) the beam. The lenses are mounted in X-Y translation holders (XY1 & XY2). The FC/APC connectorized fiber is mounted to an adapter which compensates for the 8° cleavage angle of the APC fiber. The assembly is mounted to a 90° bracket which interfaces with a 3-axis stage (3-AX) & tip-tilt stage (T/T). The stage is mounted to a breadboard interfacing with the table through kinematic mounts (KBB) to allow for easy removal of the system. The kinematic mounts allow the system to be repositioned identically, reducing re-alignment time each time the system is used. Beam is infrared; red is used for illustrative purposes only.

Space is a strong constraint for the focusing assembly; the focal lengths of L1 and L2 must be minimized. Our design utilizes aspheric lenses to minimize aberrations under conditions with short focal lengths. Implementing the system with 1-inch spherical lenses would introduce significant spherical aberrations, degrading levitation performance. Use of small-diameter aspheric lenses minimizes spherical aberrations. We will experiment with lens pairs to select pairs yielding desired spot sizes for various applications. We should be able to leave lens L2 untouched after selection and positioning, and vary L1 to achieve the desired spot size, removing the need to re-align the optics every time the spot size needs variation.

Incorporation into the microscope requires protection for both the user and the microscope. Although the beam will be mostly enclosed either in fiber or in the microscope, the beam must pass though the device and through unenclosed space before being recaptured by the objective (OBJ). Because the device could shift and tilt due to snagging of fluidic tubing, the beam could be reflected into the eyes of the operator or others in the room. Therefore, the operator should always wear adequate laser safety eyewear. Furthermore, we enclosed the entire microscopy setup with a laser curtain.

Numerous measures must be taken to further protect the microscope and user. After the beam has struck the target, it is no longer useful and is solely hazardous. Any particles or dried liquids (i.e. cell culture media) on the objective lens could absorb heat under intense illumination, damaging the lens. Therefore, we have dedicated a 20x objective (Achroplan, 440040-0000-000, Carl Zeiss) for use during optical excitation which has ~ 80% transmission at 980nm. After the beam passes through the objective, we aim to stop the beam in a number of positions in the microscope as detailed in Figure 4-3.

One level of protection is afforded by a specially designed filter cube. During IR excitation, the filter cube designed for laser protection will be used. Both the laser and the filter cube position will be controlled by the computer, so removal of the filter cube from its proper position is the only reason that the filter cube would not be in place during optical excitation. Both the excitation and transmission paths contain 2-mm-thick KG5 filter glass (Schott), which nominally has optical density (OD) 3.8 at 980 nm. A 50%/50% beamsplitter is used in the filter cube. Therefore, for a maximum excitation of 300 mW, 24 μW of power would pass through the 2-mm-thick filter cube filters assuming no dichroic properties of the beamsplitter.

Lens coatings, the CCD camera, and the user's eyes could be damaged by the laser. Protocol will dictate that the user must always wear laser safety eyewear. The eyepieces should never be used; the microscope will be used only in a video microscopy mode. The eyepieces should be switched to blackout mode when the system is used.

The CCD is at highest danger of damage. In the case of maximum power with 100% transmission at 980 nm through the beamsplitter, 48 μW of collimated power would pass into the CCD imaging path. In the worst case of focusing the beam to a diffraction-limited spot size of 1.2-μm-diameter with an NA of 1 (eq. (2.11)), the intensity would be 4.2 kW/cm^2, which is roughly four times the damage threshold for most conventional, low-power optical coatings (discussion with ThorLabs). The actual damage threshold of the CCD is unpublished, but is likely much lower than 4.2 kW/cm^2. As a comparison, the maximum allowable intensity for a typical ambient-air-cooled silicon-based handheld power sensor is 0.5 W/cm^2 (LaserCheck, Coherent). Even an optimistic estimate of intensity using an NA of 0.1 would yield an estimate of intensity of 42 W/cm^2 at the CCD.

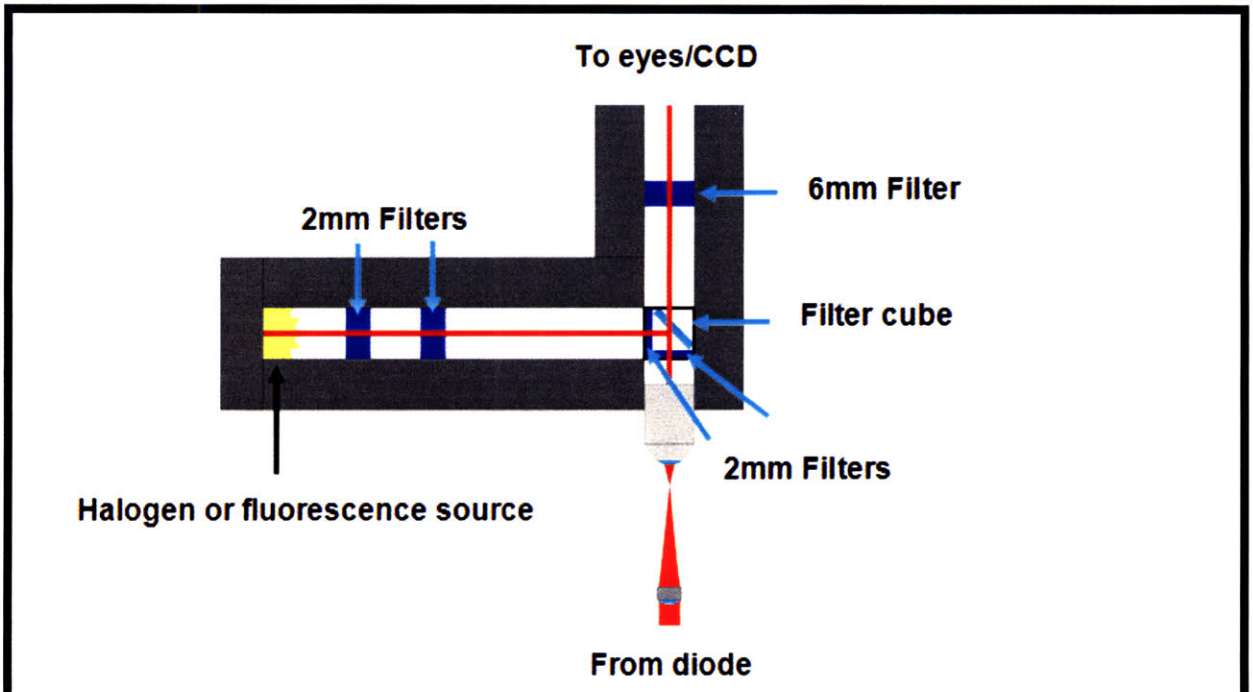

Figure 4-3: Schematic of beam-blocking measures when the laser is used. One protection layer is given by a filter cube which is selected when the laser is on. The filter cube protects both the imaging path and illumination path with 2-mm-thick filter glass both in both the excitation and illumination positions. A second protection layer is from the path-specific filters. Two separate sliders each holding 2-mm-thick filter glass protect the sources, while a 6-mm-thick (two 3mm filters) filter mounted in an analyzer slider protects the imaging path.

Unfortunately, because the filter cube can only hold a 2-mm-thick filter, sole use of a filter cube to remove the harmful beam is insufficient. Therefore, we propose using a mandatory second level of protection for the CCD. We will use a 6-mm-thick stack of KG5 filter glass in the analyzer slider position. The OD of 6 mm of glass will be 11.4, three times that of a singe 2-mm-thick filter, for a total OD of 15.2 for the total path to the CCD, yielding an intensity at the CCD of 1.7e-08 W/cm^2, well below any possible damage threshold. If, by mistake, the filter cube is removed, 1.1e-04 W/cm^2 will reach the CCD, which is still three orders of magnitude lower than the damage threshold for the power detector.

We will protect the fluorescence and halogen sources with a similar scheme. We will place two 2-mm-thick filters in sliders along the illumination path. In the absence of the filter cube, the diffraction-limited worst case intensity focused to a light source with a conservative NA of 1 would be 0.7 W/cm^2. It is impossible to know exactly what the damage threshold of the fluorescent source and halogen source is. However, with the filter cube in place, the intensity drops to 1.1e-04 W/cm^2, well below any reasonable damage threshold.

The other damage pathway is lens coating damage. The beam will not be focused onto any optical surfaces, but the beam will be collimated as it passes through the optical components of the microscope, and could possibly have a beam waist size small enough to cause locally intense illumination. We considered the worst case of the smallest possible beam waist.

The smallest aspheric collimating lens we would likely use would have an clear aperture of ~ 3 mm, yielding a 3-mm-diameter beam waist. The longest conceivable focal length of the

aspheric focusing lens would be ~ 20 mm, and the focal length of the Zeiss Achroplan is ~ 2 mm, creating a 1:10 beam collapsing system. Therefore, the beam would have a waist size of ~ 300 μm after entering the microscope. Without attenuation, the intensity of a 300 mW beam of this waist size would be 425 W/cm^2. After passing through the filter cube, the intensity would drop to 6.8e-02 W/cm^2, well below typical coating damage thresholds. Further filters would drop these powers to negligible levels.

The important point of this analysis is that *all measures must be implemented to guarantee that operation of the system is safe to the* ***user, others in the room, the microscope, and the CCD***. We have outlined the relevant powers and intensities at various points of the system under various operating configurations in Table 4-1 to illustrate the consequences of negligence in operating the system. If the user is mindful of the positions of filters, wears safety goggles, and uses the enclosure curtain, the system will be more than adequately safe to the user, co-workers, and microscope.

Table 4-1: Intensities and powers at various locations in system under various operating configuration states. (*Assumes diffraction limited spot size with NA of 1) (assumes shining of beam directly into eye; goggles assumed to have an OD of 8+ at 980nm) (*** assumes a worst-case beam waist of 300-μm-diameter)**

System State	Intensity at CCD* (W/cm^2)	Power to Eyes** (W)	Intensity at Light Source* (W/cm^2)	Intensity at Optical Coatings*** (W/cm^2)	Risks
All filters in, goggles on	1.7e-08	3.0e-09	1.1e-04	1.7e-09 (light path) 2.8e-13 (CCD path)	Safe
All filters in, goggles off	1.7e-08	3.0e-1	1.1e-04	1.7e-09 (light path) 2.7e-13 (CCD path)	Blindness
Cube out, all auxiliary filters in, goggles on	1.1e-04	3.0e-09	7.0e-01	1.1e-05 (light path) 1.7e-09 (CCD path)	Destruction of selected filter, light source damage?
Cube in, all auxiliary filters out, goggles on	4.2e+03	3.0e-09	4.2e+03	6.8e-02	Destruction of CCD, light source
Cube out, all auxiliary filter out, goggles off	2.7e+07	3.0e-1	2.7e+07	4.3e+02	All the above, loss of job

Chapter 5 – Conclusion

5.1 Goal Fulfillment

In §1.1, we outlined characteristics of the ideal image-based cell sorting architecture. Here we examine those criteria, and the extent to which the implemented architecture meets them.

"The ideal image-based cell sorting architecture would be compatible with a wide range of cell types..."

This aim was not fulfilled in the sense that adherent cell lines could be seeded, grown, observed, released, and sorted. While we did not attempt to use non-adherent operation mode with adherent cell lines for short-term experiments, such an application might be possible, provided that BSA prevented adhesion to the extent that it did with HL-60s.

As mentioned before, without BSA addition, HL-60s adhered to the PDMS, suggesting that it was use of BSA, not the use of HL-60s, which enabled the functionality of the non-adherent device mode. Therefore, it is likely that adherent cell lines as well as other non-adherent cell lines could be sorted in experiments where cell adhesion and spreading was not critical. Nonetheless, HL-60s and other non-adherent cell lines by themselves present broad platforms for useful assays.

Finally, use of more powerful lasers with the non-adherent cell lines might enable the architecture to function with adhered cells. If remaining surface adhesion forces are on the order of a few 100s of piconewtons after trypsinization, a brief 10W pulse of IR power may be sufficient to overcome this threshold, then allowing smaller powers to levitate cells. Such a use of power would be similar to that of Wang *et al* [17]. However, such sources are considerably more expensive than IR laser diodes, costing upwards of $15,000, and are much more hazardous.

"The ideal image-based cell sorting architecture would... ... allow easy imaging of cells..."

Imaging was simple with the device; imaging within microwells did not present unique complications. The device exhibited no significant background fluorescence. The use of the chamber allows for easy changing of the buffer, allowing PBS to be used during fluorescence imaging, minimizing background fluorescence.

Imaging and feature localization in non-adherent cells is more difficult than with adherent cells which have attached and spread, so arguably imaging is not as easy as it could be if adhered, spread cells were supported. On the other hand, the architecture enables easier imaging than is possible in traditional culture dishes with non-adherent cells. The small volumes of the wells significantly attenuate any random motions of the cells, making stationary imaging of the cells far easier than in much larger-volume culture dishes. Such motions will be further attenuated when we use a microscope on an air-floated table.

"The ideal image-based cell sorting architecture would... ...allow assays of time durations from short (~minutes) to long term (~days-weeks)..."

We successfully demonstrated a short term assay. It is likely that the architecture would support longer term assays as well. The fluidic interface allows the chamber volume to be refreshed either under continuous perfusion or in a discrete, periodic fashion. Such refreshing would feed cells as well as remove any undesirable buildup of cell secretions within the microwells. If facilitated paracrine signaling were deemed important, fabrication of partially fused wells is simple, allowing easier cell-cell signaling. The architecture presents numerous avenues for enhancing capabilities for long-term experiments.

"The ideal image-based cell sorting architecture would... ...allow collection of single target cells expressing responses of interest..."

We have successfully demonstrated on-chip single-cell isolation. This ability includes cases of wells containing more than a single cell. Our demonstration is a successful first step towards single-cell off-chip separation. Demonstration of off-chip isolation of target cells is non-trivial, and we have not attempted to demonstrate the world-to-chip interfacing. As explained in §4.1, the fluidic interface will need to be redesigned to allow facilitated capture of high-purity samples. The described alteration or a similar methodology will likely allow for off-chip isolation. We have demonstrated a clean, robust first step towards this end goal.

"The ideal image-based cell sorting architecture would... ...scale to large array sizes while keeping operation and overhead of the architecture simple."

We have demonstrated that the architecture completely meets this goal. The fabrication process and packaging scheme are trivial by the standards of most microdevices. Design and fabrication of a thousand-site-array, a million-site array, and a custom array layout are equally trivial. Operational overhead, both physical and financial, is constant for all array sizes, simply requiring a laser source and automated microscope.

Potentially most important is the intuitive, simple operation of the architecture; the user must simply point the beam at the desired target to retrieve it. Loading the device is equally simple; no special techniques outside of simple injection of cells are required. The total simplicity of the device makes it extremely robust – after developing and following working protocols, we never experienced a *single failure* due to device or architecture overhead complications in all non-adherent-mode experiments presented in this thesis. As a result of simple scaling, trivial fabrication and packaging, ease of use, and easy of incorporation into widespread microscopy systems, the method could be appealing to a wide range of audiences in the research community, both inside and outside the biological arena.

5.2 Contributions and Future Directions

We have presented a highly scalable architecture enabling simple, intuitive, image-based sorting of non-adherent cells. We have experimented with adherent cell lines and obtained results useful for design of future adherent cell architectures. Additionally, we have provided an example plan for incorporation of the system into a typical upright fluorescence microscope.

After incorporation into an automated fluorescence microscope, the platform will enable a new class of image-based genetic screens. Based on the results of the discussed cell health research, we should be able to use our system to isolate viable mutant cells and grow them into

larger populations, enabling simplified creation of mutant cell lines. The system stands to make a significant contribution to genetic screening.

The system is simple, intuitive, and robust enough to be appealing to researchers outside our lab. It is unlikely that a researcher completely unfamiliar with optics, microfluidics, and microfabrication could implement the entire system from scratch in a brief time. However, the optical system components could be packaged such that installation on a microscope required installation of a few small retro-fittings. Assuming that a pre-fabricated SU-8 master were provided, learning to create and package devices is trivial, enabling use of the platform by any researcher willing to make a brief (<2 week) learning commitment.

Equally as important as the cell sorting assays enabled by the architecture are its other potential applications. The work in this thesis has dealt exclusively with removal of targets of interest for capture. One obvious extension of this work would be extension to applications involving non biological particles benefiting from image-based sorting. It is possible that other particles may be more amenable to manipulation by the scattering force, as their refractive indices may have larger contrast with the suspending medium than cells, allowing larger forces to be exerted on them.

Work by Adam Rosenthal, a fellow lab member, has centered around loading single cells into microwell arrays and subsequently flipping the microwell array onto a substrate, patterning single cells for culture. This technique has been named the "Bio Flip Chip." If well array chambers were reversibly bonded, such as with an adhesive gasket layer, the chamber could be opened, and desired cells could be patterned onto a culture substrate, allowing the techniques to be combined.

The optical architecture could add capabilities to the Bio Flip Chip. Combining the two technologies could enable patterning of multiple cell types, as illustrated in Figure 5-1. We would first seed the cell type comprising the majority of the desired pattern. We could then remove the first cell type from all wells where other cell types were desired. We would then flow in another cell type, subsequently removing the second cell type from undesired locations. This method could be repeated for an arbitrary number of cell types. After loading the wells in the desired arrangement, we would use the device as a Bio Flip Chip, patterning the cells for culture.

Time would be the limiting factor in such a method. However, the technology scales well for some relevant experiments. In the example shown in Figure 5-1 A-D, if 60 sets of three-cell patterns were desired, we would need to levitate 60 cells from wells for flushing. Assuming that that the system were automated and that purging a cell took 10 seconds, this operation would take only about 10 minutes. In the example in Figure 5-1 E-J, 60 sets of three-cell patterns would require 180 cell removals, requiring 30 minutes. It is possible, however, that the applied power could be increased, since levitated cells need not be viable, potentially reducing the purging time.

Finally, the well array could be constructed from a digestible polymer. Cells could be seeded in the array using a reversibly-bonded chamber, and undesired cells could be removed, enabling construction of ultra-pure tissue scaffolds (idea from Prof. Matthew Lang). Alternatively, a method similar to that of Figure 5-1 combined with used of a digestible polymer could enable construction of tissue scaffolds with controllable starting cell arrangements of multiple cell types.

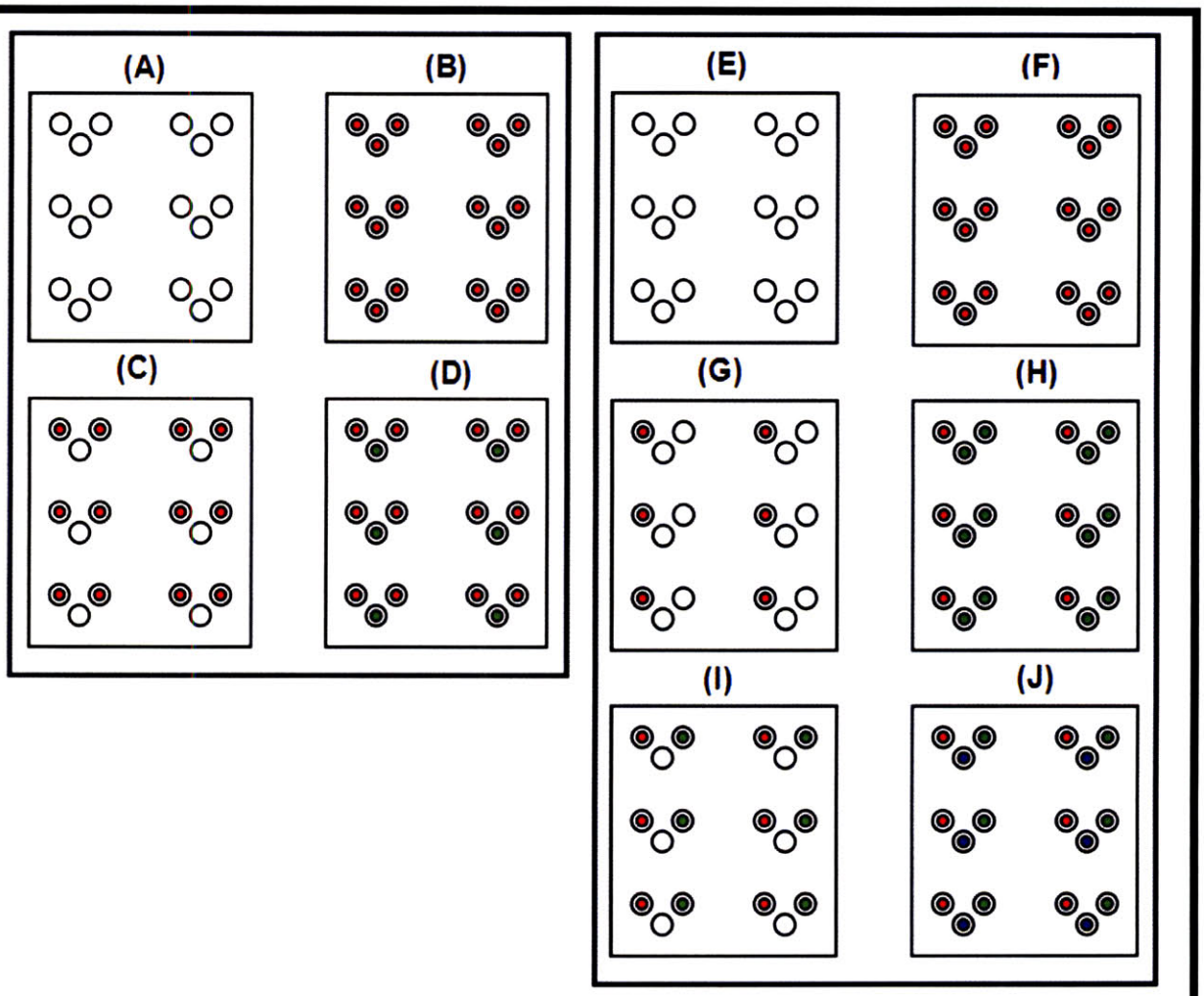

Figure 5-1: Schematic of patterning multiple cell types with the architecture. A) Empty device. B) Cell type I is seeded. C) Cell type I is removed from undesired locations. D) Cell type II is seeded; chamber is opened and cells are patterned onto a culture substrate (not pictured). E) Empty device. F) Cell type I is seeded. G) Cell type I is removed from undesired locations. H) Cell type II is seeded. I) Cell type II is removed from undesired locations. J) Cell type III is seeded; chamber is opened and cells are patterned onto a culture substrate (not pictured).

Appendix: MatLab Implementation of Optical Force Model

```
clear; %Clear workspace variables
CollimatedMode=1;%Set to 0 if using focused beam; 1 if using collimated beam

if (CollimatedMode==0)
    f=9.9499;%Set dimensionless focal length corresponding to
             %N.A. of 0.1 assuming a clear aperture radius of 1
else
    f=1e10;  %Approximate focal length of infinity for collimated case
end

n1=1.34;%Refractive index of media
n2=1.41;%Refractive index of nucleus
c=3e8;%Speed of light [m/s]

GridSpaces=500;%Grid spacing for simulation; # of grid points along each row
TotalPower=0.100;%Total power of simulated beam [W]

[X,Y]=meshgrid(linspace(-1,1,GridSpaces),linspace(-1,1,GridSpaces));
%Create simulated square aperture to trace rays through; simulation
%utilizes only a circular portion to simulate a circular lens aperture.
Radius=sqrt(X.^2+Y.^2);%Radial locations corresponding to each point on the
%rectangular aperture.
NumBeams=prod(size(Radius));%Total number of beams to be traced
EdgeLength=sqrt(NumBeams);%Number of beams per edge of square aperture
P=TotalPower/NumBeams;%Power per beam [W/beam]

FszAll=[];%Vector which will hold total z-directed scattering forces for
%each value of S, the fraction of a cell radius by which the cell is
%axially out of the focal point.
FgzAll=[];%Analogous to FszAll, but contains Z-directed gradient forces.
FtotalAll=[];%Total axial force for each value of S.

R=1;%Define dimensionless cell radius as 1.
Smax=1;%Set maximum axial displacement of cell in terms of R.
nmax=10;%Divisions of S to go through; a value of 10 would correspond to
%simulating at S=[0 0.1 0.2.... 0.9 1]

for n=0:nmax%Loop over all values of S to simulate
    S=Smax*n/nmax;
    phi=atan(Radius/f);%Matrix of values of phi for each point in the square
                       %aperture
    if (CollimatedMode==1)
        theta=asin(Radius/R);%For collimated case, simple geometry shows that
                             %theta reduces to this limiting case
    else
```

```
        theta=asin(S/R*sin(phi));%Focused case, this follows from [13]
    end

    thetatrans=asin((n1/n2*sin(theta))); %Snell's law to solve for
                                         %transmitted angle.
    Rs=((n1*cos(theta)-
n2*cos(thetatrans))./(n1*cos(theta)+n2*cos(thetatrans))).^2;
    %Fresnel reflection coefficients (s-polarized)
    %from each point in the square aperture
    Rp=((n1*cos(thetatrans)-
n2*cos(theta))./(n1*cos(thetatrans)+n2*cos(theta))).^2;
    %Fresnel reflection coefficients (p-polarized)
    %from each point in the square aperture
    Ts=1-Rs;
    %Fresnel transmission coefficients (s-polarized)
    %from each point in the square aperture
    Tp=1-Rp;
    %Fresnel transmission coefficients (p-polarized)
    %from each point in the square aperture

    Fss=(1+Rs.*cos(2*theta)-Ts.^2.*(cos(2*theta-
2*thetatrans)+Rs.*cos(2*theta))./(1+Rs.^2+2*Rs.*cos(2*thetatrans)));
    Fgs=((Rs.*sin(2*theta)-Ts.^2.*(sin(2*theta-
2*thetatrans)+Rs.*sin(2*theta))./(1+Rs.^2+2*Rs.*cos(2*thetatrans))));
    %S-polarized scattering (Fss) and gradient (Fgs) values of Q [13] for
    %each point in the square aperture.
    Fsp=(1+Rp.*cos(2*theta)-Tp.^2.*(cos(2*theta-
2*thetatrans)+Rp.*cos(2*theta))./(1+Rp.^2+2*Rp.*cos(2*thetatrans)));
    Fgp=((Rp.*sin(2*theta)-Tp.^2.*(sin(2*theta-
2*thetatrans)+Rp.*sin(2*theta))./(1+Rp.^2+2*Rp.*cos(2*thetatrans))));
    %P-polarized scattering (Fsp) and gradient (Fgp) values of Q for each
    %point in the square aperture.

    FsTotal=(Fss+Fsp)/2; %Total value of Q due to scattering forces
                         %for circular polarization
    FgTotal=(Fgs+Fgp)/2; %Total value of Q due to gradient forces
                         %for circular polarization

    FsTotal(find(Radius>1))=0; %Simulate circular aperture by only
                               %including values where the aperture radius
                               % is less than 1.
    FgTotal(find(Radius>1))=0;

    Fsz=n1*TotalPower/c*4/pi*sum(sum(FsTotal.*cos(phi)))/NumBeams;
    Fgz=n1*TotalPower/c*4/pi*sum(sum(FgTotal.*sin(phi)))/NumBeams;
    %Compute the total scattering and gradient forces resulting
    %from focusing from the circular aperture.  Note the correction
    %of 4/pi, which accounts for power lost by cutting out a fraction
    %of power from the square aperture

    Ztotal=(Fsz+Fgz);%Total axial force
    FszAll=[FszAll Fsz];
    FgzAll=[FgzAll Fgz];
    FtotalAll=[FtotalAll Ztotal];%Update vectors so that behavior vs. S
                                 %can be observed.
end
```

References

1. Grimm, S., *The art and design of genetic screens: Mammalian culture cells.* Nature Reviews Genetics, 2004. 5(3): p. 179-189.
2. Ashcroft, R.G. and P.A. Lopez, *Commercial high speed machines open new opportunities in high throughput flow cytometry (HTFC).* J Immunol Methods, 2000. 243(1-2): p. 13-24.
3. Revzin, A., et al., *Development of a microfabricated cytometry platform for characterization and sorting of individual leukocytes.* Lab on a Chip, 2005. 5(1): p. 30-37.
4. Taff, B.M. and J. Voldman, *A scalable addressable positive-dielectrophoretic cell-sorting array.* Analytical Chemistry, 2005. 77(24): p. 7976-7983.
5. Voldman, J., et al., *A microfabrication-based dynamic array cytometer.* Anal Chem, 2002. 74(16): p. 3984-90.
6. Yamamura, S., et al., *Single-cell microarray for analyzing cellular response.* Analytical Chemistry, 2005. 77(24): p. 8050-8056.
7. EmmertBuck, M.R., et al., *Laser capture microdissection.* Science, 1996. 274(5289): p. 998-1001.
8. Chiou, P.Y., A.T. Ohta, and M.C. Wu, *Massively parallel manipulation of single cells and microparticles using optical images.* Nature, 2005. 436(7049): p. 370-372.
9. Pei Yu, C., et al. *Cell addressing and trapping using novel optoelectronic tweezers.* 2004.
10. Huang, Y., et al., *Introducing dielectrophoresis as a new force field for field-flow fractionation.* Biophysical Journal, 1997. 73(2): p. 1118-1129.
11. Buma, T., M. Spisar, and M. O'Donnell, *High-frequency ultrasound array element using thermoelastic expansion in an elastomeric film.* Applied Physics Letters, 2001. 79(4): p. 548-550.
12. Ashkin, A., et al., *Observation of a Single-Beam Gradient Force Optical Trap for Dielectric Particles.* Optics Letters, 1986. 11(5): p. 288-290.
13. Ashkin, A., *Forces of a Single-Beam Gradient Laser Trap on a Dielectric Sphere in the Ray Optics Regime.* Biophysical Journal, 1992. 61(2): p. 569-582.
14. Lang, M.J. and S.M. Block, *Resource letter: LBOT-1: Laser-based optical tweezers.* American Journal of Physics, 2003. 71(3): p. 201-215.
15. Grier, D.G., *A revolution in optical manipulation.* Nature, 2003. 424(6950): p. 810-816.
16. Birkbeck, A.L., et al., *VCSEL Arrays as micromanipulators in chip-based biosystems.* Biomedical Microdevices, 2003. 5(1): p. 47-54.
17. Wang, M.M., et al., *Microfluidic sorting of mammalian cells by optical force switching.* Nature Biotechnology, 2005. 23(1): p. 83-87.
18. Ozkan, M., et al., *Optical manipulation of objects and biological cells in microfluidic devices.* Biomedical Microdevices, 2003. 5(1): p. 61-67.
19. Rettig, J.R. and A. Folch, *Large-scale single-cell trapping and imaging using microwell arrays.* Analytical Chemistry, 2005. 77(17): p. 5628-5634.

20. Liang, H., et al., *Wavelength dependence of cell cloning efficiency after optical trapping.* Biophys J, 1996. 70(3): p. 1529-33.
21. Neuman, K.C., et al., *Characterization of photodamage to escherichia coli in optical traps.* Biophys J, 1999. 77(5): p. 2856-63.
22. Liu, Y., et al., *Evidence for localized cell heating induced by infrared optical tweezers.* Biophys J, 1995. 68(5): p. 2137-44.
23. Lee, J.N., et al., *Compatibility of mammalian cells on surfaces of poly(dimethylsiloxane).* Langmuir, 2004. 20(26): p. 11684-11691.
24. Mrksich, M. and G.M. Whitesides, *Using self-assembled monolayers to understand the interactions of man-made surfaces with proteins and cells.* Annual Review of Biophysics and Biomolecular Structure, 1996. 25: p. 55-78.
25. Eddington, D.T., J.P. Puccinelli, and D.J. Beebe, *Thermal aging and reduced hydrophobic recovery of polydimethylsiloxane.* Sensors and Actuators B-Chemical, 2006. 114(1): p. 170-172.
26. Weast, R.C., *CRC handbook of chemistry and physics.* 1st Student ed. 1988, Boca Raton, FL: CRC Press. 1 v. (various pagings).
27. Deen, W.M., *Analysis of transport phenomena.* 1998, New York: Oxford University Press. xix, 597 p.
28. Born, M. and E. Wolf, *Principles of optics : electromagnetic theory of propagation, interference and diffraction of light.* 7th expanded ed. 1999, Cambridge ; New York: Cambridge University Press. xxxiii, 952 p.
29. Dana, K.J., *Three Dimensional Reconstruction of the Tectorial Membrane: An Image Processing Method using Nomarski Differential Interference Contrast Microscopy.* MIT S.M. Thesis, 1992.
30. Drezek, R., A. Dunn, and R. Richards-Kortum, *Light scattering from cells: finite-difference time-domain simulations and goniometric measurements.* Applied Optics, 1999. 38(16): p. 3651-3661.
31. DiCarlo, D., et al., *Large Scale Single Cell Analysis Using High Density Hydrodynamic Trapping Arrays.* Proceedings of the MicroTAS 2005 Conference, 2005. 1: p. 379-381.
32. Ostuni, E., et al., *Selective deposition of proteins and cells in arrays of microwells.* Langmuir, 2001. 17(9): p. 2828-2834.